THE PASSIVE SCALAR CONCENTRATION AND VELOCITY FIELDS OF ISOLATED TURBULENT PUFFS

By

Elham Ghaem-Maghami

A Dissertation

Submitted to the Faculty

of the

WORCESTER POLYTECHNIC INSTITUTE

in partial fulfillment of the requirements for the

Degree of Doctor of Philosophy

In

Mechanical Engineering

By

_____

June 2006

APPROVED:

_____

Dr. Hamid Johari, Advisor

_____

Dr. John J. Blandino, Committee Member

_____

Dr. Jeffrey S. Goldmeer, Committee Member

_____

Dr. Grétar Tryggvason, Committee Member

_____

Dr. Mark W. Richman, Graduate Committee Representative

To My Parents

Abstract

Passive scalar concentration and velocity fields of isolated turbulent puffs were examined experimentally using the planar laser Mie scattering and PIV techniques, respectively. Work in WPI laboratories on reacting, fully-modulated jets has indicated significantly reduced flame lengths for compact puffs in comparison with steady and pulsed jets. Of particular interest is the entrainment and mixing of isolated turbulent puffs away from the nozzle. The present experiments were carried out in order to enhance fundamental understanding of the velocity fields associated with isolated, turbulent puffs. Puffs were generated by injecting air through a 5 mm diameter nozzle into a flow chamber with a weak co-flow. The injection time was varied by the use of a fast-response solenoid valve from 20 ms to 161 ms. Puffs with a Reynolds number of 5,000 were examined in the range of 25 – 75 diameters downstream of the nozzle. The results indicate that as the injection volume increases, puffs evolve from a spherical geometry to one with a tail. The distribution of a passive scalar within the examined turbulent puffs is unlike that in turbulent vortex rings. The half-width of radial concentration profile through the puff center decreases as the injection volume increases. On the other hand, the puff length in the axial direction increases with the injection volume. The results from phase-locked PIV measurements indicate that the largest axial mean velocities and the radial velocity fluctuation are within the central portion of the puff and the largest axial velocity fluctuation are typically present above the puff center. The turbulent shear stress profiles within puffs are antisymmetric about the centerline and the maximum magnitude for the smallest injection volume is 2.5 times the steady jet value. The vorticity fields calculated from phase-locked velocity field data indicate the presence of vorticity throughout the puff volume. The ratio of puff volume flow rate to steady jet at the puff center location was largest for the smallest injection volume. The majority of entrainment into the puff occurs below the puff center while the puff cap pushes out into surrounding fluid. In general, the puff characteristics did not reveal an internal structure analogous to that in the turbulent vortex ring.

Acknowledgment

Dr. Hamid Johari has been the motivation behind this research. He had spent a great deal of his time and effort in helping and guiding me through the research for the past five years. He is also my inspiration towards a successful career. I would also like to thank Dr. John J. Blandino, Dr. Jeffrey S. Goldmeer, Dr. Mark W. Richman, and Dr. Grétar Tryggvason for serving on my graduate committee. I would also like to greatly acknowledge the financial support of the National Aeronautics and Space Administration, Microgravity Research Division, under Cooperative Agreement NNC04GA61G as well as advice and support from Mr. Dennis P. Stocker and Dr. Uday Hegde.

I would like to thank Dr. Srinivasan Dattarajan, Dr. Kenneth Desabrais, Dr. Adriana Hera, and Dr. James Hermanson for their assistance and support. I also acknowledge the help that has always been given to me with a smile by Tracy Coetzee, Barbara Edilberti, Barbara Furman, Pamela St. Louis, Siamak Najafi, and Randolph Robinson the kindest and nicest people of the Mechanical Engineering Department. I would like to thank my families and friends Abhijeet, Ediyta, Hamid, Ian, Irene, Jayant, Larry, Pradeep, Ramin, Ritchie, Sagar, Scott, Siju, Sunita, Susan, Vasin who always supported me, directly or indirectly while I was working on this dissertation. I would like to thank Jim Johnston who never denied a helping hand.

I would like to thank my parents and my brothers for a lifetime love, support and continuous confidence in me. It is because of them that I am enjoying this stage of my life. Last and definitely not the least I am really grateful to my husband, Vinod Tilak, who has been my inspiration and strength over all these years and for being so supportive and encouraging, and being there for me when I needed.

Table of Contents

List of Figures

List of Tables

Nomenclature

English Symbols

a	Gaussian constants
B_u	decay constant
k_u	Gaussian constants
C	concentration within the flow field
C^*	absorbing species concentration
C_e	entrainment constant
C_z	best fit empirical parameter of time
c	puff numerical factors
d	nozzle diameter
f	pulsing frequency
H	stroke length, $4\ \forall_o/\pi d^2$
I	puff initial momentum
I_b	background intensity
I_L	beam intensity before propagating
I_{Laser}	laser beam intensity
I_{mflow}	measured seeded flow intensity
I_{mL}	beam intensity after propagating
I_{mS}	measured fog intensity
TKE	turbulent kinetic energy
L	flame length
$L_{0.1}$	puff full length
$L_{0.5}$	puff half-length
M	honeycomb mesh diameter
$\dot{m}$	mass flux
$\dot{m}_e$	entrained mass flux
$\dot{m}_i$	initial mass flux
n	puff size constant number

P	cube root of stroke ratio, $(H/d)^{1/3}$
P_1	axial pressure
P_{Back}	back pressure
Q	volume flow rate
Re_{jet}	jet exit Reynolds number
r	radial coordinate
$r_{1/2}$	half-radius
SF	flow-multiplying factor
t	time
t_o	virtual origin in time
T	time variable
U	axial velocity
U_c	centerline velocity
U_{cof}	co-flow velocity
U_o	injected velocity
u'_{rms}	rms value of axial velocity fluctuation
$\forall$	Puff volume
$\vec{V}$	velocity vectors
$<u'v'>$	turbulent shear stress
$\forall_o$	injected volume flow
V	radial velocity
v'_{rms}	rms value of radial velocity fluctuation
w'_{rms}	rms value of azimuthal velocity fluctuation
z	axial coordinate
z_c	puff center location
z_o	virtual origin
$(z/d)_c$	normalized puff center location

Greek Symbols

α	pulse injection duty cycle

α_e	entrainment coefficient
δ	puff width
$\delta_{0.1}$	puff full-width
$\delta_{0.5}$	puff half-width
η	similarity constant
κ	non dimensional universal constant
ρ_a	density of surrounding fluid
ρ_i	density of jet flow
σ	characteristic radius
τ	pulse cycle injection time
τ_o	pulse cycle off time
τ_t	total pulse cycle time
υ	viscosity coefficient
υ_t	turbulent viscosity coefficient
ξ	similarity constant
ψ	stoichiometric air/fuel ratio

1. Introduction

1.1 Background

An important area of study in the field of fluid mechanics is the behavior of turbulent jets. Turbulent jets are important because they exhibit more efficient mixing qualities than do laminar or transitional jets. The increase in efficiency is due to the increased surface area that the jet turbulence creates with the surrounding fluid. Turbulent flow structures, entrainment and mixing rate are parameters of great interest among researches. Industrial applications of this knowledge range from chemical processes that involve turbulent mixing, to combustion, where information on entrainment rates of ambient air into the flame can be utilized. Recently interest in partially pulsed or periodically perturbed reacting and non-reacting jets has been growing due to the potential efficiency gains and pollution control characteristics. A clear understanding of the turbulent flow jet characteristics would help create new technologies for pollution control and minimization of the impact of emissions on the environment.

1.1.1 Steady and Pulsed Non-Reacting Jets

Extensive investigations have been carried out on the steady jet, which is characterized by lateral spreading and a decrease in the jet velocity. The presence of large scale structures has been experimentally observed in many steady turbulent jets (Ricou & Spalding, 1961; Crow & Champagne, 1971; Dimotakis *et al.*, 1983). Two aspects of the large scale organizations are entrainment and mixing characteristics. Entrainment and mixing of ambient fluid with the jet fluid occurs due to vortices. These vortices surround the ambient fluid and draw it into the jet (Chen & Rodi, 1980; Turner, 1986). As vortices pair and mix inside the jet, the ambient fluid is further mixed with the jet fluid.

The near field region is defined as the region within 15 to 20 orifice diameters of the jet origin. It has been established that the internal interaction of the jet fluid persists throughout the near field region. A number of studies have revealed that in the near field, the jet is dominated primarily by large scale ring-like vortex structures. These vortices form as a result of the roll-up of the axisymmetric shear layer surrounding the jet core (Hill, 1972).

Entrainment and mixing in the far field region, which is defined to be greater than 25 orifice diameters of the jet origin, had been generally viewed as unorganized structure involving mainly small scale motions (Chen & Rodi, 1980). Dahm & Dimotakis (1987) showed experimentally that the far field behavior of turbulent jets does involve large-scale structures and related entrainment mechanisms. More recent works provide enough evidence to support the existence of large scale structures in the jet far field (Tso *et al.*, 1981; Dimotakis *et al.*, 1983; Dahm & Dimotakis 1987). These structures span the jet width and have fairly uniform concentrations. Simple physical models based on the large scale structures have successfully explained several features of the jet diffusion flames such as the blowout process (Broadwell *et al.*, 1984; Dahm & Dibble, 1988).

The concentration field of a conserved passive scalar was measured in aqueous jets (Dahm & Dimotakis, 1987; Dahm & Dimotakis, 1990) and in gaseous jets (Dowling *et al.*, 1989). In the jet far field, the mean centerline velocity and the concentration of a conserved scalar decay inversely with the downstream distance in a self-similar manner and the jet spreads linearly. The mean radial profiles are approximately Gaussian curves (Tennekes & Lumley, 1972). Classical turbulent models for free shear flows predict the

mean behavior of the self–similar jet fairly well. These models are based on the concept of stochastic transport by small eddies.

Unsteady turbulent jets are different than their steady counterparts. A large number of research works are found in the literature on disturbing the jet in an effort to alter the jet entrainment and mixing. Studies have shown that the jet entrainment can be increased in the near field through controlling the vortical structures by adding a small periodic disturbance (Crow & Champagne, 1971, Liepmann & Gharib, 1992). Direct forcing of isothermal jets with specific acoustic input have been shown by many researchers to result in increased spreading rates and enhanced mixing over unforced jets (Crow & Champagne, 1971). These studies show that noticeable changes in non-reacting jet growth and entrainment can be found even at relatively low pulsation frequencies of the order of 10 Hz (Lovett & Turns, 1990). The effects of acoustic forcing have been seen as far out as seventy nozzle diameters downstream, with an increase in local entrainment of as much as a factor of three (Vermeulen & Ramesh, 1986). Sarohia & Bernal (1981) pulsed an air jet harmonically at an amplitude of about 10% while keeping the time averaged mass flow rate constant. It was observed that velocity profile spreading and volume flow rate of the jet were increased in the near field. The velocity field of the fully pulsed air jets (the mass flow rate was zero between pulses) has been investigated by Platzer *et al.* (1978) and Bremhorst & Hollis (1990). For the fully pulsed jets, the entrainment can be as much as twice that of the steady or partially pulsed jets. This effect was seen as far as 50 nozzle diameters. It was believed that the entrainment enhancement was coupled with an increased Reynolds stress values. Fully modulated jets appear to have significantly increased entrainment even in the far field (Bremhorst & Hollis, 1990).

In fully pulsed jets when the injection times are short and a relatively long time exists between the subsequent pulses, the jet consists of a sequence of distinct, non-interacting turbulent puffs. In case of reacting flow, these puffs react and burn rapidly, in comparison with steady jets (Johari & Motevalli, 1993; Hermanson *et al.*, 2000).

A puff refers to a distinct mass of turbulent fluid moving unsteadily through its surrounding with which it mixes readily (Richards, 1965; Oshima *et al.*, 1977). The puff structure may be considered similar to a turbulent vortex ring with the vorticity spread throughout the puff volume (Glezer & Coles, 1990). Puffs with low and high injection volume are shown schematically in Fig. 1.1. A compact puff with no tail signifying the low injection volume is shown in Fig. 1.1a, and an elongated puff with a tail is shown in Fig. 1.1b. One method of generating puffs is to impulsively inject the source fluid through a nozzle. This technique creates a vortex ring if the stroke ratio, H/d, is small, say of order one. As the stroke ratio increases, the injected fluid rolls up into a compact puff. In the limit of very large stroke ratios, a starting jet is created. Past work has shown that the volume of a compact isolated puff increases with the axial distance to the third power, i.e. z^3, because the puff width increases linearly in the far field, $\delta \sim z$. Volumetric arguments have been used to show that the bulk entrainment and mixing rates scale with the cube root of the injected volume (Johari & Motevalli, 1993). In fact, the scaling laws for the spreading and celerity (velocity of puff center) of puffs and vortex rings in the self-similar regime (the dynamics of the flow are independent of initial conditions and are governed by the local velocity and length scales) are identical except for the proportionality constants (Richards, 1965; Kovasznay *et al.*, 1974; Glezer & Coles,1990):

$$\delta \sim (z - z_o) \tag{1.1}$$

$$(z - z_o) \sim (\frac{I}{\rho})^{1/4}(t - t_o) \tag{1.2}$$

$$\frac{dz}{dt} \sim (\frac{I}{\rho})^{1/4}(t - t_o)^{-3/4} \sim \frac{I}{\rho}(z - z_o)^{-3} \tag{1.3}$$

The virtual origins in space and time, z_o and t_o, depend on the apparatus generating the puff or vortex ring. The puff width increases linearly with the distance from the virtual origin (Eq. 1.1) and the puff celerity decreases rapidly with the axial distance from the virtual origin (Eq. 1.3). Note that the specific impulse, I/ρ, does not influence the puff width scaling law in Eq. 1.1. For compact puffs with nearly spherical geometry, the volume in the far field is expected to scale with the cube of puff width. Sangras *et al.* (2002) measured the penetration and width of turbulent puffs in an aqueous media using video records of the puff visual outline at Reynolds numbers of 3 to 12 thousand. They found that the penetration and width of puffs follow the self-similar scaling for distances greater than 20-30 source diameters (Diez *et al.*, 2003). Moreover, a virtual origin of 8.5 source diameter was reported, independent of the injected volume and Reynolds number for the range of parameters in their experiments.

1.1.2 Effect of Chemical Reaction and Heat Release on Turbulent Jets

Turbulent combustion occurs in most practical combustion devices, including airbreathing propulsion systems, heaters and furnaces, incinerators and numerous other industrial processes (Jones & Leng, 1994; Parr *et al.*, 1996). In certain applications, flames are non-premixed, in that the fuel and oxidizer are not mixed prior to being injected into the combustion chamber. Of key importance to the mixing processes are the

large-scale structures that are common among all turbulent shear flows, including turbulent flames (Mungal & O'Neil, 1989; Mungal *et al.*, 1991). Compared to the case of non-reacting shear flows, the large-scale structures in turbulent flames are modified by the heat release in the flame, the associated volume dilatation, and by buoyancy. Increasing the understanding of these phenomena is critical to improving our understanding of turbulent jet flames.

Pulsed combustion has the potential for high combustion and thermal efficiencies, excellent heat transfer characteristics and low CO, NO_x and soot emissions (Lefebvre, 1975; Haynes & Wagner, 1981; Peters & Donnerhack, 1981; Driscoll *et al.*, 1992; Turns & Bandaru, 1993; Tang *et al.*, 1995; Turns, 1995; Hermanson *et al.*, 2004). A significant amount of research has been performed on pulse combustors, including examination of the overall system characteristics, such as heat transfer, efficiency, frequency of operation, and pollutant formation (Keller & Hongo, 1990).

Much of the research conducted in unsteady reacting jet flows to date has involved direct forcing of the jet with a specified acoustic input. Turbulent flames have been seen to be sensitive to acoustic-level pulsing of the fuel stream (Lovett & Turns, 1990). Forcing with low frequency (approximately 10 Hz) can produce a strong coupling with the buoyant structure in the far field, with a significant impact on the flame length and fuel/air mixing. Other research involving acoustic excitation or feedback has been conducted with both non-premixed and premixed flames in ramjets (Reuter *et al.*, 1990), pulsed combustors (Reuter *et al.*, 1986; Tang *et al.*, 1995), and other ducts (Hedge *et al.*, 1988; Chen *et al.*, 1993). Each of these combustor configurations is; however, characterized by a strong coupling between the combustion process and the acoustic

field. In recent years the understanding of the fundamental fluid mechanics behind these processes has been of interest and is a central focus of the current effort.

A fundamentally different approach to unsteady combustion is to fully-modulate the fuel jet flow, that is, to completely shut off the fuel flow between pulses. This type of flow control can give rise to drastic modification of the combustion and flow characteristics of flames, leading to enhanced fuel/air mixing mechanisms not operative for the case of acoustically excited or partially-modulated jets (Johari & Motevalli, 1993; Hermanson *et al.*, 2000).

Flame tests excluding acoustic coupling or other confinement effects have been conducted and these works represent a useful step towards understanding the complicated combustion behavior in pulsed combustion systems. Experiments on unconfined, widely separated buoyant fuel puffs by Johari & Motevalli, (1993) showed a decrease in mean flame length of fully-modulated flames of up to 70% compared with a steady, turbulent jet at low Reynolds number ($Re_{jet} \approx 2000$). That work examined not only the effects of pulsing frequency on flame length and structure but also those due to the duty-cycle (i.e., the jet-on fraction of each pulsation cycle).

Subsequent work by Hermanson *et al.* (2000) demonstrated a flame length reduction of fully-modulated flames of approximately 50% for Reynolds numbers of up to $Re_{jet} = 20{,}000$. This work also revealed two distinct types of flame structures for fully-modulated flames. For short injection times (small injected volume), puff-like flame structures with a roughly spherical shape and a very short flame length were observed. For relatively longer injection times, more elongated flames resulted. The flame lengths of the elongated flames were generally comparable to those of the corresponding steady-

state cases. It has been argued that the greater entrainment of turbulent puffs is responsible for the observed short flame lengths (Johari & Motevalli, 1993; Hermanson *et al.*, 2000). A puff may entrain ambient air over a larger surface area as compared to the steady jet with lateral entrainment.

The transition from compact, puff-like to elongated flame behavior can be characterized in terms of the following parameter:

$$P \equiv \frac{\sqrt[3]{4V_o/\pi}}{d} = \left(\frac{H}{d}\right)^{\frac{1}{3}} \tag{1.4}$$

where H is the height of the injected slug (as indicated in Fig. 1.2), and d is the exit jet diameter. This parameter was developed by taking the volume of injected gas to be a cylinder having the same volume as that of the injected fuel and with a base diameter equal to the nozzle diameter, d (Hermanson *et al.*, 2000). The height of the cylinder, H, is computed by dividing the total volume of gas injected by the nozzle exit area. The $1/3^{rd}$ power stems from volumetric arguments for isolated, isothermal puffs (Johari & Motevalli, 1993). The puff aspect ratio, H/d, can be used to related to whether a fully-modulated flame puff will be compact, or more elongated in structure. By comparing the visual description of the pulsed flames with their characteristic P value, it is possible to correlate elongated structures with large values of P (long cylinders) and puff-like structures with small values of P (flat cylinders). Generally, puff-like behavior is seen for values of P less than approximately $P = 8$ for ethylene/air flames. Images of four representative flames (one steady and three fully-modulated) are shown in Fig. 1.3 (Usowicz, 2002).

In addition, for isolated, puff-like structures, the parameter P is directly related to the mean flame length, since the latter has been shown previously to scale with the cube root of the injected volume (Johari & Motevalli, 1993; Hermanson *et al*., 2000):

$$L/d \propto (1+\psi)^{1/3} P \tag{1.5}$$

where ψ is the stoichiometric air/fuel ratio. Hermanson *et al.* (2004) showed the normalized flame length decreased to as little as 22% of the steady jet flame length for sufficiently small P. They also showed for isolated flame puffs, the linear dependence of flame length on the P parameter given in Eq. 1.5 persisted to approximately $P \approx 11$. For longer injection times (higher value of P), the flame length approached that of the steady flame. The data result are shown in Fig. 1.4.

Temperature measurements also made by Hermanson *et al.* (2000) suggested that the temperature associated with the puff-like flame structures rises more rapidly with downstream distance than for the corresponding steady-state flame. The temperature characteristics of the elongated structures were more similar to those of the steady-state flame.

1.2 Objective of Present Research

The objective of this research is to improve the understanding of fundamental issues pertaining to the internal structure of puffs and its dependence on the initial conditions. A review of the available literature shows that there is no data or physical description of puff internal structure. To accomplish these objectives, the passive scalar concentration and velocity fields associated with the far field of isolated, non-reacting, turbulent puffs

were measured. The parameter P, derived from the initial conditions, in the range of 4-8, has been used to classify the internal structure and quantitative characteristics of turbulent puffs. So the aim of the study is to address the following questions:

- What is the effect of injection volume (time) on non-reacting puff structure?
- How does the radial and axial concentration profiles of isolated non-reacting puff vary with injection volume (time)?
- How does the volume of isolated non-reacting puffs vary with injection volume (time)?
- How do the velocity and vorticity field of isolated non-reacting puffs vary with injection volume (time)?
- How does the entrainment process for the turbulent isolated puff occur?

To accomplish these objectives, non-interacting turbulent puffs with $4 \leq P \leq 8$, were generated by injecting finite volume of seeded air into a flow chamber with a weak air co-flow. The injection time (and volume) was used to vary the puff injection parameter P, and the associated puff stroke ratio by the use of a fast-response solenoid valve.

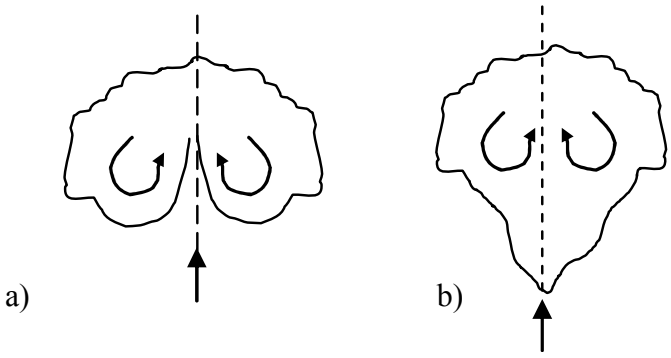

Figure 1.1: Schematic of turbulent puffs: a) short injection time; b) long injection time. An elongated tail is indicated in (b).

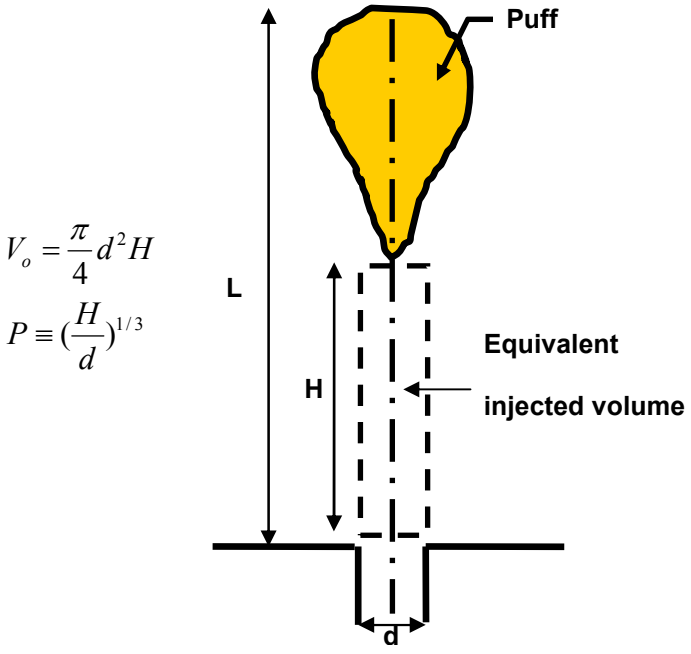

Figure 1.2: Puff injection parameter *P* and visual description.

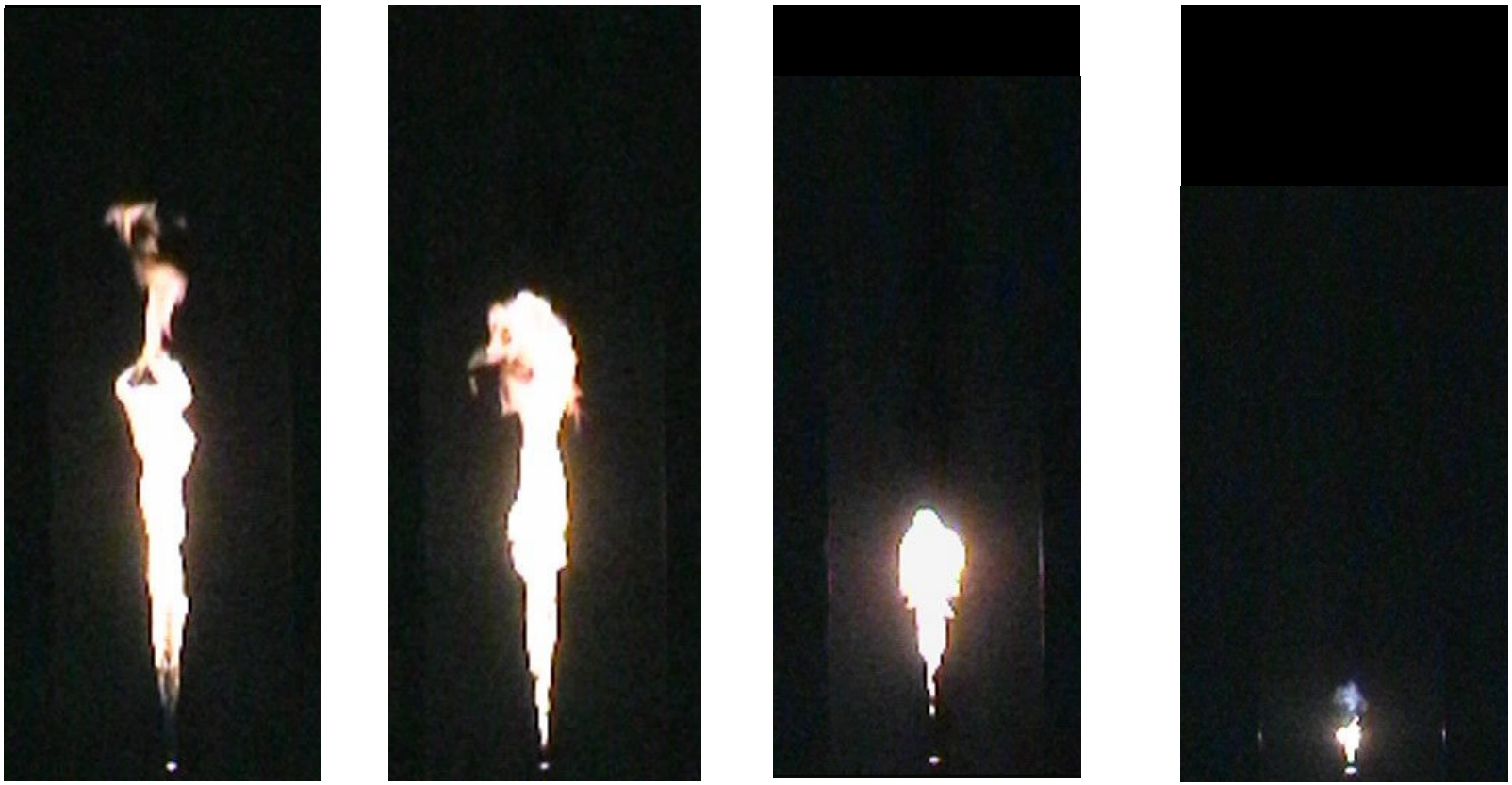

a) Steady Flame **b) $P = 11, \tau = 119$ ms** **c) $P = 8$, $\tau = 46$ ms** **b) $P = 4$, $\tau = 5.745$ ms**

Figure 1.3: Flame comparison, Re_{jet} = 5,000, U_{cof} / U_o = 0.005, Image Height = 58.4 cm (from Usowicz, 2002).

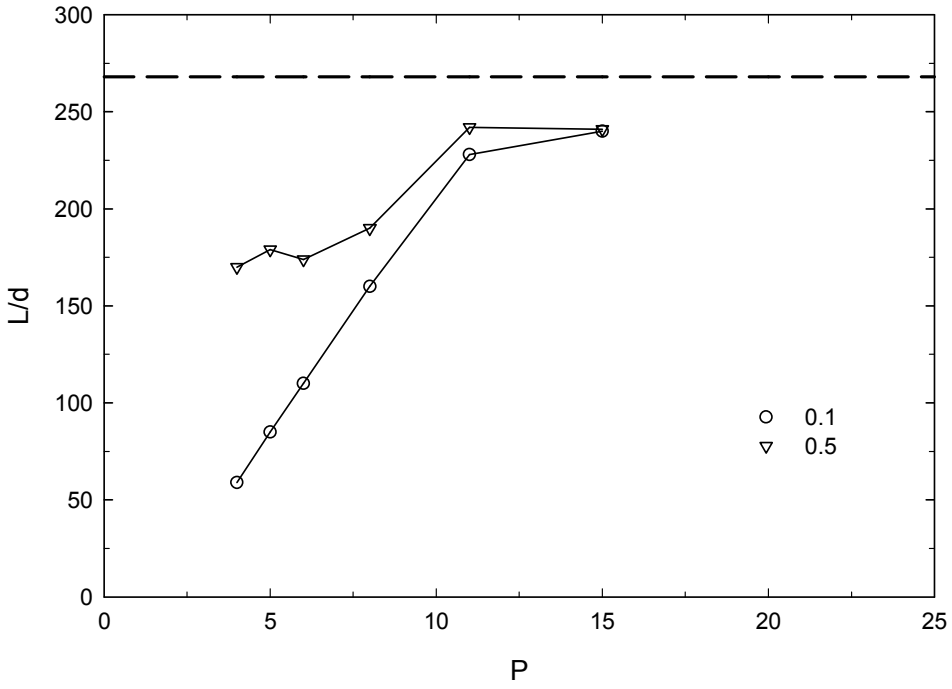

Figure 1.4: Flame length of fully-modulated flames at two duty cycles. The dashed line represents the steady flame length (from Hermanson *et. al.* 2004).

2. Experimental Apparatus and Setup

The experimental apparatus consisted of a co-flowing flow chamber combined with an injection system. Each of these systems is described in detail in the following sections.

2.1 Flow Apparatus

2.1.1 Flow Chamber

The flow chamber setup consisted of a square duct (30 × 30 cm in cross section,) through which co-flow air was supplied, as shown schematically in Figs. 2.1a and visually in Fig. 2.1b. The co-flow duct was 67 cm in length and had walls of glass to facilitate flow visualization. The co-flow conditioning section was 34.8 cm in length and was constructed mainly of aluminum in order to give the flow chamber a rigid base. Co-flow air was supplied to the flow chamber by shop-air supply, which passed through a 1-inch (2.54 cm) diameter PVC tube with a rotameter and pressure gauge attached inline as shown in Fig. 2.2. To ensure the proper flow profile entered the rotameter, ten diameters of straight tube were situated upstream of the rotameter. The PVC tube was constricted down to 1/2 inch (1.27 cm) via copper tubing which was routed around the flow chamber. Air was injected into the bottom of flow chamber from four points, one in the midpoint of each side. Special attention was paid to the lengths of copper tubing used so that there was a fairly even distribution of air flowing into each of the four ports. A honeycomb/screen combination and two perforated plates were situated upstream of the injection nozzle, as shown in Fig. 2.1, with the distance between the nozzle and the top surface of the honeycomb held at 4.1 cm. The honeycomb used had a mesh size of M = 0.125 inch (0.3175 cm) and the screen had a mesh size of 40 per linear inch. The

perforated plates had hole diameters of 0.125 inch (0.3175 cm) and an open area of about 60 percent.

Standard shop air was used for the co-flow fluid. The flow velocities were controlled via an OMEGA FL7412 rotameter. Pressures were monitored downstream of the rotameter and the flows were corrected by using a standard rotameter correction factor based on these pressures.

Calibration was required for the co-flow. This was completed by using the flow meter and the relative calibration factor, SF. The only calibration necessary was for pressure effects. The flow-multiplying factor for the pressure was calculated using the following relation (Brooks, 2004):

$$SF = \sqrt{\frac{P_{Back} + 14.7}{14.7}} \tag{2.1}$$

where P_{Back} is the back pressure in psi as read from one of the installed pressure gage. The flow meter calibration pressure of 14.7 psig (101.325 kPa) was chosen. Appendix A shows the velocity ratios and their corresponding co-flow flow rates for jet Reynolds numbers 5,000.

2.1.2 Air Injector Section

The air injector nozzle consisted of a 5 mm inner diameter stainless steel tube with a length to diameter ratio of 40. The solenoid was positioned in the center of the flow chamber by plumbing the air line through the center of the plenum section. Stainless

steel was used for the air line piping material inside the flow chamber and a combination of brass and stainless steel was used outside of the flow chamber.

A fast-response solenoid valve (Parker Hannifin Series 9) was used to control the air flow. In all cases the jet was fully-pulsed, that is, 100% modulated, at frequencies of up to 3.7 Hz. The valve cycling was controlled by a Parker Hannifin Iota One control unit. The unsteady flow characteristics of the injector system were surveyed using a hot-wire placed immediately downstream of the nozzle exit. The hot-wire anemometer signal was sampled at 6 kHz and low-pass filtered at 3 kHz. Fig. 2.3 shows an ideal pulse cycle where the flow is completely shut on and off, and an actual sample time traces of the jet velocity, U_o, is shown in Fig. 2.4 for the pulsing frequency of 3.7 Hz and injection time of 23 ms. A certain amount of velocity fluctuation was observed during each pulse. To define a precise value of injection time τ, the length of the time when the velocity was greater than 5% of the peak velocity at each cycle was measured for each pulse and averaged over the sampling period. Knowing the actual injection time and the pulsing frequency, an effective duty cycle could be found. The nominal values of injection time and P are compared against the actual values in Table 2.1.

Table 2.1: Pulse characteristics.

$\tau_{nominal}$ (ms)	$P_{nominal}$	f(Hz)	τ_{actual} (ms)	P_{actual}
20	4	2.5	23	4.17
39	5	1.3	38	4.95
68	6	0.7	69	6.03
161	8	0.3	170	8.13

The velocity traces indicate a certain amount of velocity overshoot at the beginning of each pulse. The nozzle length was optimized to remove any spike at the end of each cycle by examining different size of *L/d*.

The actual value of the jet injection velocity was determined using a FMA 1700/1800 series OMEGA mass flow meter under steady flow conditions. Since the pulses were repeatable and sufficiently close to a standard square wave the pulse flow conditions were set from an in-line pressure measurement that was determined under steady flow conditions.

2.2 Diagnostics

2.2.1 Puff Concentration Field (Mie Scattering Technique)

Elastic light scattering from particles, or Mie scattering, is one of the common techniques for flow visualization. The Mie scattering theory is a complete mathematical-physical theory of the scattering of the electromagnetic radiation by spherical particles, developed by Gusta Mie in 1908. Mie theory describes the scattering of light by particles (Hulst, 1957). The Mie theory embraces all possible ratios of diameter to wavelength. Mie scattering technique was used to acquire instantaneous 2D images of the flow field, at desired stations. Light from a laser was formed into a thin sheet with appropriate optics, and directed through the flow. The scattered light by tracer was collected at right angle on a CCD camera. The measured light intensity at each pixel in the CCD array is proportional to the concentration of seed particles in the volume imaged onto that pixel.

For flow visualization, a Spectra-Physics Stabilite 2016-05S argon ion laser was used as the illumination source. This laser had the capability of operating at different wavelengths (458-514nm) which allowed for greater power flexibility. All lines of the laser were used, providing a maximum power output of 1.8 W. The laser beam had a thickness of about 1 mm at the source.

The purpose of the optics was to create a thin sheet of laser light which when directed through the test section. The sheet illuminated the fog particles seeded in the jet flow. Leveling the laser with optics reduced the complexity of the optics setup. Passing the laser beam through a cylindrical lens spread the beam into a narrow sheet, creating a sheet of laser light.

Fog, used as the flow-marking medium, is injected into the test chamber through the nozzle and illuminated when in the area of the laser light sheet. The size of the fog was about 1 micron. When the light is scattered by the fog, the characteristic structures of the flow become visible due to the spatial distribution of fog densities.

2.2.1.1 Fog Generator

For the passive scalar measurement, the injected puff was seeded by fog. In order to obtain quantitative results for the concentration field, it was necessary to have uniformly seeded puffs at the source and the seeding particles to be small. The fog generation and fog-air mixing processes were an important consideration in the setup of the fog generator. In order to obtain a uniform fog seeding in the viewing section, the correct amount of air needed to be diverted through the fog generator and the correct temperature in the generator had to be achieved.

The inlet to the fog generator was supplied through a shop-air source. The inlet air was passed through a 1.4 inch (6.35 mm) diameter brass tube attached to the generator at 85 mm away from the bottom of it. Air along with fog was introduced into the nozzle via a 3/8 inch (9.52 mm) stainless steel tube. A ball valve was installed between the outlet line of generator and main flow to the nozzle. This setup allowed a very fine fog distribution, which was well suited for concentration field measurements and flow visualization.

A pharmaceutical grade ethylene glycol-based water mixture was used as a vaporizing fluid to produce a dense white fog cloud. A fog generator was constructed of a stainless steel tube with a diameter of 4 inches (102 mm) and a length of 13.4 inches (340 mm) as shown in Fig. 2.5. Heating tape along with insulation cloth was wrapped around the generator. Aluminum metal shavings were used to fill the inside of the generator in order to uniformly distribute the heat inside the generator. The temperature of the fog generator was an important parameter, which was controlled by a benchtop Omega (MCS series) controller. If temperature is too low, then not much fog will be formed, and if it is too high, then fog will go too quickly. Temperature was read through the front digital panel on the temperature controller. A type K thermocouple was placed on the generator centerline, halfway between the ends in order to track the temperature inside the fog generator. The generator was initially heated to 650 F and then the vaporizing fluid was inserted through the top of generator via a 1/8 inch (3.145mm) ball valve. The temperature was held between 600 to 700 F during entire run.

2.2.1.2 Imaging Equipment

The cross-sectional images of the seeded puff were recorded by a progressive scanning CCD camera manufactured by Pulnix (model number TM 6702) with a 640 × 480-pixel resolution. The image data were captured using a MuTech MV-1000 frame grabber board. The images were acquired at 60 frames per second for 25 seconds, resulting in 1500 images for each flow condition. A visual programming package, WiT, in conjunction with Matlab was used for processing of the images and data extraction. The details of the image processing routine are given in Appendix B. A Computar zoom lens was used for this setup. This lens had a maximum aperture of *f1*.2, and a focal length range of 1.5 to 10 m.

2.2.1.3 Image Correction

The laser intensity profiles measured by the camera were converted to profiles of concentration according to the characteristics of the scattered laser intensity. The laser intensity variation across the image was an important factor, since it is represented the biggest source of systematic error in the data. The effects of the spatial non-uniformity of the incoming laser sheet and reduction in the laser input power due to scattering needed to be corrected on the recorded images. Moreover, the detected signals (image) depend on the optical arrangement (laser sheet, collection optics), and the characteristics of the imaging sensors. It must be realized that light from a finite volume in the flow field is imaged onto each pixel (Karasso, 1994). The acquired images had significant spatial variation of laser intensity across the imaged region as a result of variation due to the fall-off intensity from the middle part of the laser sheet to its edge, and light absorption along the light propagation path.

Taking into account all the previous factors, image processing was performed on the acquired image to correct each image for the systematic variations, and get the concentration distribution across the image area of the flow

The intensity of the laser beam diminishes along its line of propagation, due to light absorption. The absorption follows the Beer-Lambert law:

$$I_{Laser}(z) = I_o e^{-I(C)l} \tag{2.2}$$

Where l is the direction of propagation of the laser beam, I_{laser} is the laser intensity. I(c) is the attenuation coefficient per unit length at the concentration C. The intensity of laser beam without fog and flow can be corrected as

$$I_{mL} = I_b + I_L \tag{2.3}$$

where I_L and I_{mL} are beam intensity before and after propagating and I_b is background image with camera lens blocked. As fog was used as a seeder, the imaging equation for the intensity of fog alone without any flow can be written as (Karasso, 1994)

$$I_{mS} = I_b + I_L + I_{Laser} \times C^* \tag{2.4}$$

Where I_{mS} is the measured fog signal, C^* is the absorbing species concentration within the flow field volume imaged on a pixel which is a just a constant number, which for our work was taken to be one, and I_{Laser} is the laser beam intensity.

The imaging equation for the signal on every pixel of a digitized flow image for the experimental case can be obtained as follow:

$$I_{mflow} = I_b + I_L + I_{Laser} \times C \tag{2.5}$$

Where I_{mflow} is measured seeded flow signal, and C is the concentration within the flow field volume. Combining Eq. 2.3, 2.4 and 2.5, the image processing for each image evolved as:

$$C = [(I_{mflow} - (I_b + I_L))/ \ I_{Laser}] = (I_{mflow}-I_{mL})/(I_{mS}-I_{mL}) \quad (2.6)$$

Since this technique provides relative measurements, the above equation had to be appropriately normalized for each case to the maximum signal obtained.

2.2.2 Particle Image Velocimetry Technique

The velocity fields of isolated non-reacting puffs were measured using the PIV system. Particle Image Velocimetry (PIV) is a whole field technique providing instantaneous velocity vector measurements in a cross-section of a flow. In PIV, the velocity vectors are derived from subsections of the target area of the particle-seeded flow by measuring the movement of particles between two light pulses. The particulars of the PIV technique are described by Willert & Gharib (1991), and Raffel *et al.* (1998). The PIV system used for our measurements was based on the commercial LaVision hardware and software. The laser used in the LaViosn PIV setup consisted of a Big Sky Laser Nd:YAG laser. This unit included two Nd:YAG lasers, each of which fired independently with variable frequency. The laser pulses were synchronized with the CCD camera frame rate, and the time separation, Δt, between successive pulses was established by a counter/timer board in a PC. The time separation between pulses was set depending on the puff velocity. Each laser pulse had duration of 5 ns and a maximum energy output of approximately 180 *mJ*. Only 25-30 % of the energy output was used for

the experiments. Each laser was pulsed at a frequency of 15 Hz that generated velocity fields at a rate of 15 Hz, due to the frame straddling method used in the PIV measurements. The laser pulses were directed through a cylindrical lens with the focal length of -10 mm to create a laser sheet for illumination of the puff flow field. The laser sheet had a thickness of 3 mm and was oriented parallel with the flow velocity. This setup is shown in Fig. 2.6. In this study, the instantaneous velocity fields were measured by phase-locking the PIV system to the driving signal of the pulsing valve. For this purpose, the TTL output signal of the solenoid controller triggered with the PTU delay time of the laser. The PTU is a PC integrated timing board that allows a precise time management for the trigger pulses needed to control camera and illuminations, like a laser or strobe light. A direct cross correlation was used for the processing.

2.2.2.1 Imaging Equipment

The PIV images were recorded using a CCD camera, which was mounted at a right angles to the puff flow field. The camera used, LaVision Image Pro X, had a 1600 × 1200 pixel resolution and a 30 Hz frame rate. A 50 mm Nikon lens was used for imaging in the PIV experiments. This lens had a maximum aperture of *f*1.8, and a focal length range of 3 to 0.45 m. LaVision's *DaVis* software allowed complete camera function control, synchronization with lasers and peripheral device activation. All software functions are programmable via LaVision's command language (CL). CL allowed the automation of complete measurement sequences including data acquisition and processing.

2.2.2.2 Solid Particle Seeder

A solid particle seeder based on a cyclone generator was designed and constructed (McCabe, 1976; Zenz, 1960). The seeder mixed the incoming air with a bed of particles in the seeder body. The seeder body was made of a PVC tube with a diameter of 5 inch (127 mm) and a length of 700 mm as shown in Fig. 2.7. The seeder had three inlets; each was 1/4 inch (6.35 mm) in diameter. One inlet was the main air inlet; the other two were for agitating the fine particles. The seeded air exited the seeder through a pipe with diameter 3/8 inch (9.52 mm). The seeder exit was connected to the co-flow of the flow chamber. Particles were added to the seeder through a 35 mm diameter hole which was 150 mm away from the bottom of the seeder. A cyclone was used to mix the particles when the inlet air forced the particles way up. Two perforated plates, which had hole diameters of 0.125 inches (31.75 mm) and open area of about 60 percent were located at 200 mm away from the bottom of seeder, were used to get a fairly even distribution of particles in the air flowing into the outlet line. The seeder had been designed for particle sizes ranging from 1 μm to 40 μm.

For the present set of experiments, the co-flow was seeded with aluminum oxide particles that had a mean particle diameter of 9 μm. Table 2.2 lists the properties of aluminum oxide used as seed. Particle inertia is required to allow particle trajectories to deviate from fluid trajectories. The most important measure of particle inertia is the Stokes number. Stoke's number for the particles may be computed by Eq. 2.7:

$$St = \frac{\tau_{particle}}{\tau_{flow}} \tag{2.7}$$

where $\tau_{particle} = \frac{d_p^2 \rho_p}{18\mu}$, and $\tau_{flow} = \frac{\delta}{U_c}$. Particles become more fluid-like as *St* approaches zero and are distributed more uniformly in an incompressible fluid flow. When *St* exceeds unity, particles become less responsive to the flow field, behaving more like random walkers, and as such are also distributed more uniformly. The most non-uniform distributions result when *St* is at or near unity. The corresponding Stoke's number for the present study is shown in Table 2-3. Figure 2.8 provides a good example of the seeding density in the flow field.

Table 2.2: Properties of aluminum oxide.

Physical Form	Solid, Flat, Clear, Plate-shaped Crystal
Melting Temperature	2000C (3632F)
Density	3.8 g/cm^3
Hardness	9 Mohs Scale; 2100 Knoop Scale
Water Solubility	Insoluble
Color	White
Typical Analysis	
Al2O3	99.59%
Na2O	0.35%
Fe2O3	0.03%
SiO2	0.03%

Table 2.3: Stokes numbers for different *P* puffs for 9 μm aluminum oxide.

P	***St***
4	4.71E-04
5	1.22E-03
6	2.24E-03
8	1.74E-02

2.2.2.3 PIV Parameters

The PIV vector processing algorithm used interrogation windows of 32×32 pixels with an overlap step of 16 pixels (50%) in each direction. This corresponds to a spatial resolution of 3.81 mm vertically and horizontally. The area of the velocity field measured was between 40 to 75 nozzle diameter in axial distance and between -15 to 15 (30) nozzle diameter in radial direction. The origin of the coordinate system was defined on the centerline of the nozzle. The laser pulse separation time was set at different values for puffs with different P numbers. The selection of pulse separation time was based on range of 5 to 10 pixels of the particles movement for the image pairs.

The experimental measurements were phase locked by using PIV. The phase locking was performed based on the required position of puffs in the range of 40 to 80 nozzle diameters in axial extent. The phase locked measurements of puffs were controlled by the external triggering frequency and required time delay into the field of view. Phase locked instantaneous data were ensemble-averaged and interpolated in order to obtain the mean velocity field. Figure 2.9 shows a photograph of the PIV experimental equipment.

2.3 Uncertainty Quantification

2.3.1 Uncertainty of the Mie Scattering Technique

The in-plane resolution for the field of view was about 300 μm, and the out-of-plane resolution was dictated by the laser sheet thickness of ≈ 1.5 mm. These values are comparable to the estimated Kolmogorov length scale of ~ 1 mm in the imaged area. The estimated average uncertainty of the concentration measurements was ±3%, based on the

pixel count uncertainty, as well as the uncertainty of puff position and optical alignment (Taylor, 1997). The average standard error of the mean concentration values was 1.4%.

2.3.2 Uncertainty of the PIV Measurements

For the estimation of the uncertainty of PIV velocity measurements many parameters have to be considered (Raffel *et al.*, 1998). Systematic errors occur due to the uncertainty in the determination of the geometrical parameters and the spatial setup of the camera devices and lenses. Non-systematic errors are mainly due to the uncertainty in the determination of the average particle displacement in the interrogation region. These depend on the size of the interrogation region, the time separation between the laser pulses, the magnification of the recording, the out-of-plane velocity component, the turbulence and the length scale of the flow, etc. The choice of the recording and interrogation parameters is therefore of significant importance for accurate and reliable velocity measurements. As the flow in the test section was quasi axisymmetric, the out of plane component of the vectors causes only negligible errors. The software used to cross-correlate the images is capable of resolving the particle displacement to within ±0.04 pixels, however in the interest of maintaining a conservative error estimate, a value of ±0.05 pixels was used. The peak particle movements were kept less than 10 pixels, which occurred in the core region of the flow. The range of pixel movement in the co-flow was less than 1 pixel, and the average particle motion in the center region of the flow was approximately 4 pixels. This corresponds to an error of ±1.25% in the velocity measurements, and ±1.50% for the rms of the velocity (Stanislas, *et al*., 2005).

The vorticity was calculated based on the velocity field, and the method used compounds the error by a factor of 3 (Raffel *et al.*, 1998). Therefore, the error in the vorticity values is approximately ±3.75%. It should be noted that these error values are based on an average pixel motion. Near the leading edge of the flow and in the "core" region, the velocities, and therefore the particle motions, were higher; while near the sides and trailing edge of the flow, they were smaller.

a)

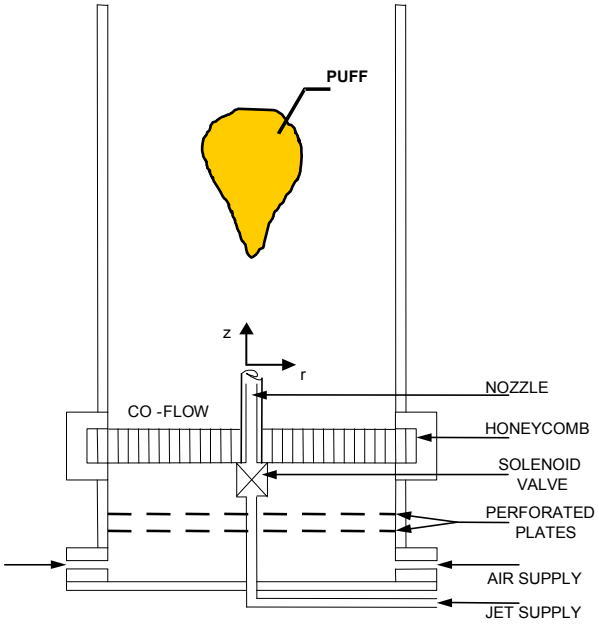

b)

Figure 2.1: Flow Chamber: a) schematic; b) photograph.

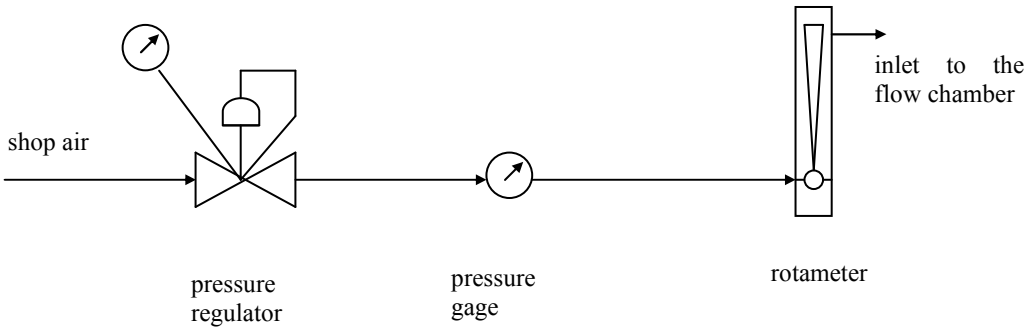

Figure 2.2: Schematic of the co-flow airline.

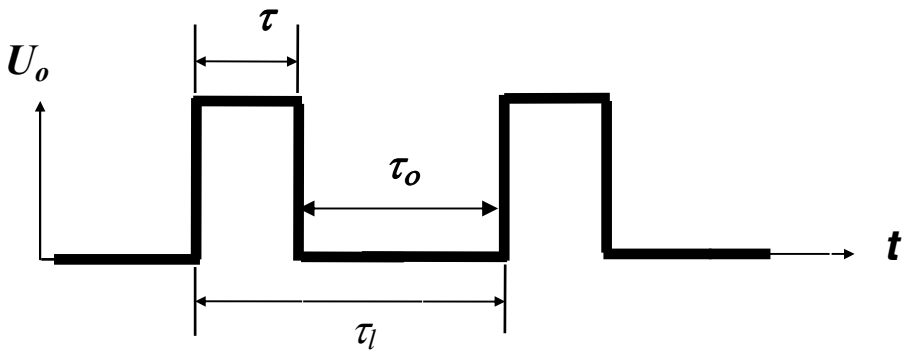

Figure 2.3: Ideal pulse cycle.

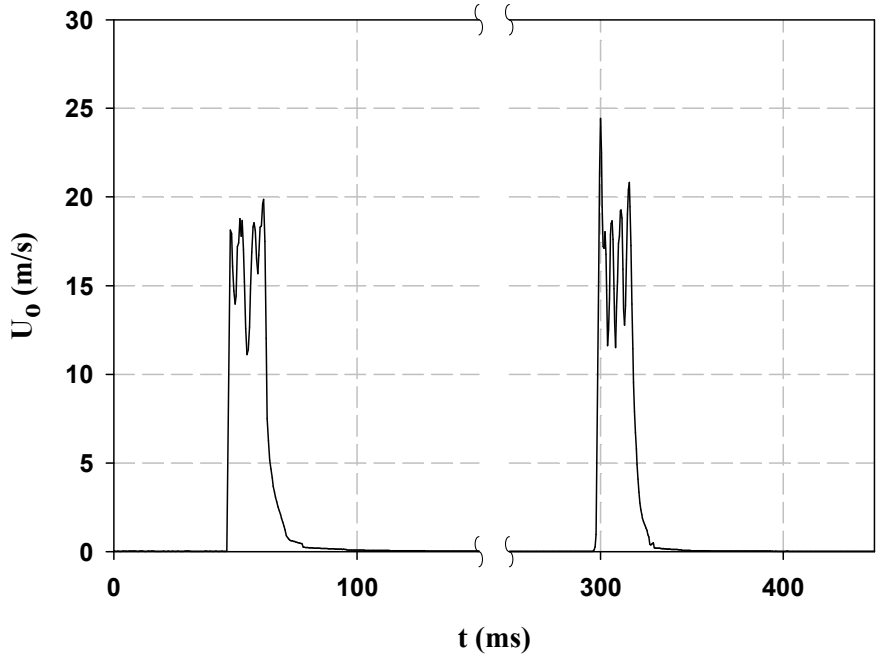

Figure 2.4: Time trace of jet velocity for an injection time of 23 ms.

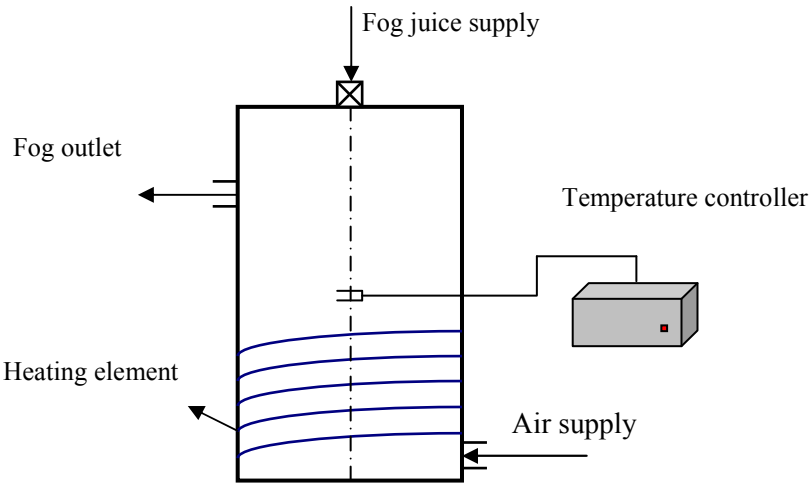

a)

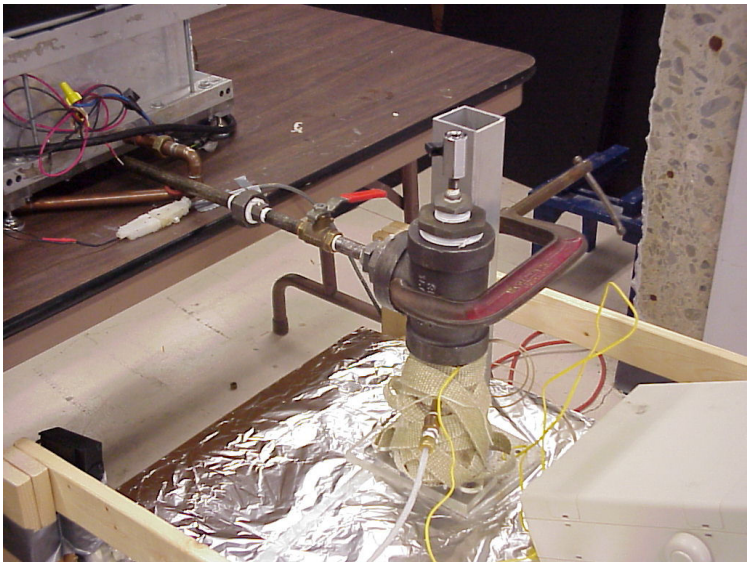

b)

Figure 2.5: Fog generator: a) schematic; b) photograph.

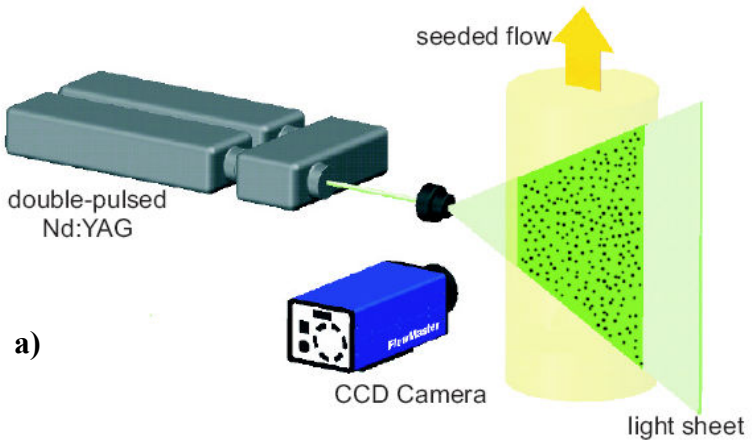

a)

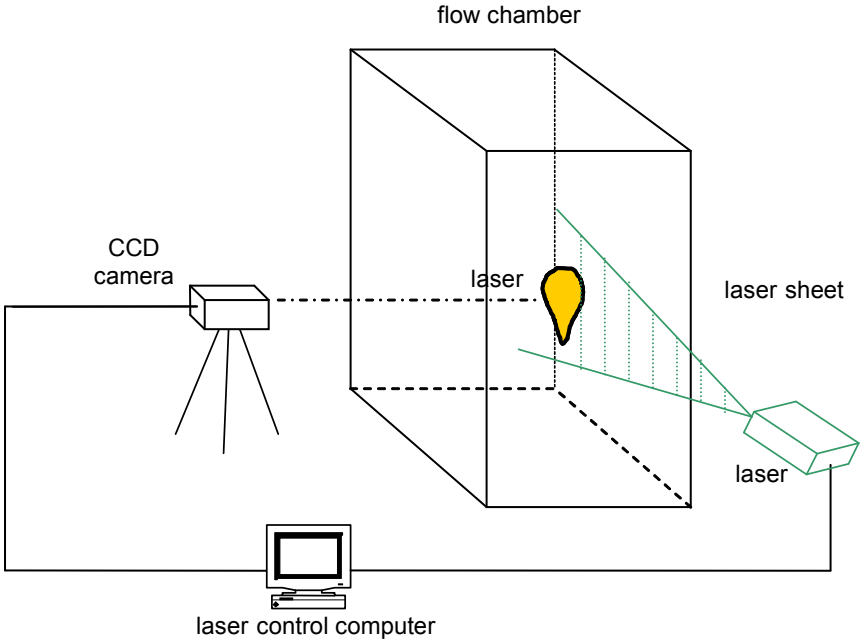

b)

Figure 2.6: PIV laser setup: a) In general (from *www.laviosn.de* webpage); b) Experimental setup.

a)

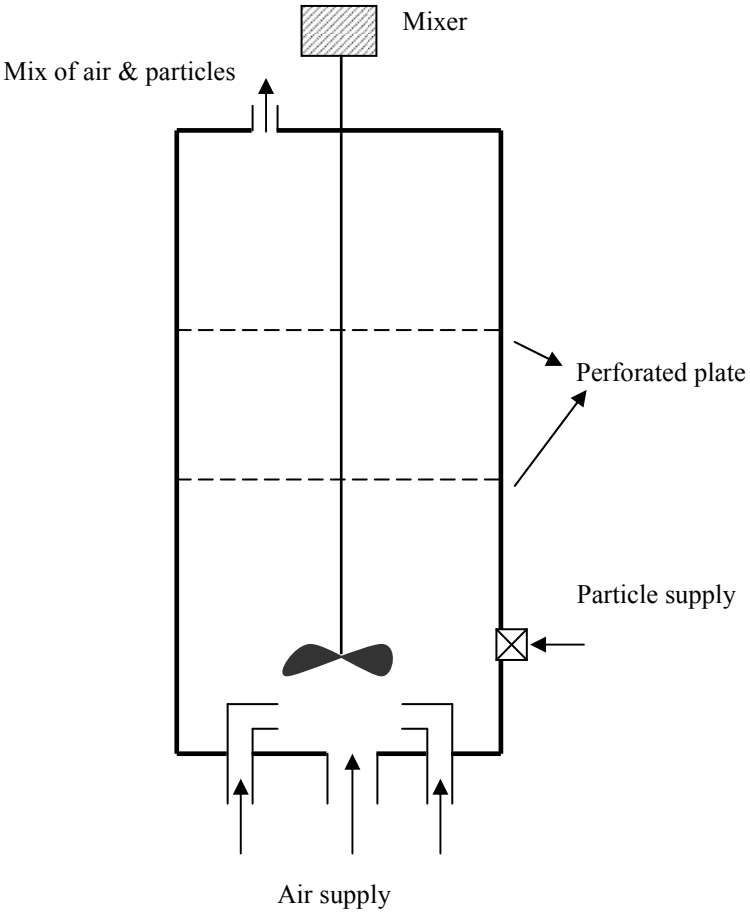

b)

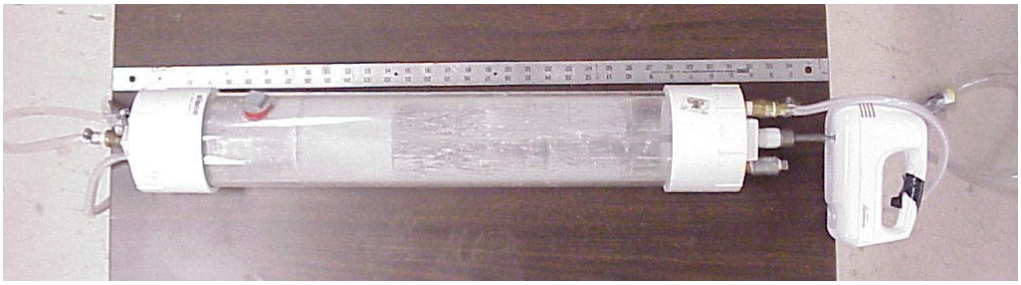

Figure 2.7: Solid particle generator: a) Schematic; b) photograph.

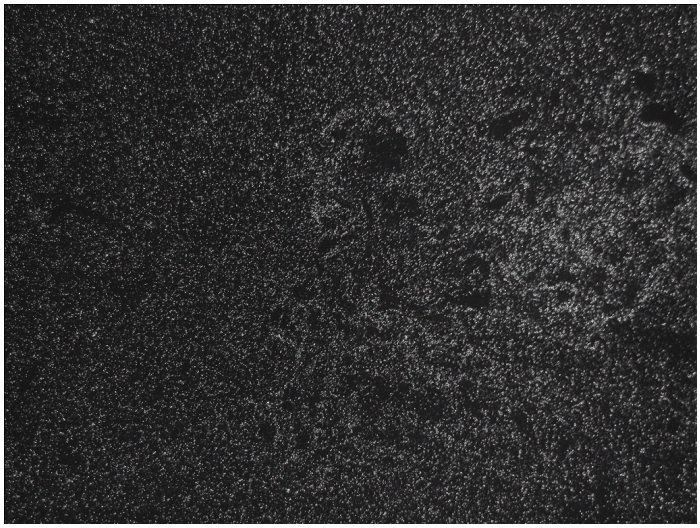

Figure 2.8:. Sample of a seeding image.

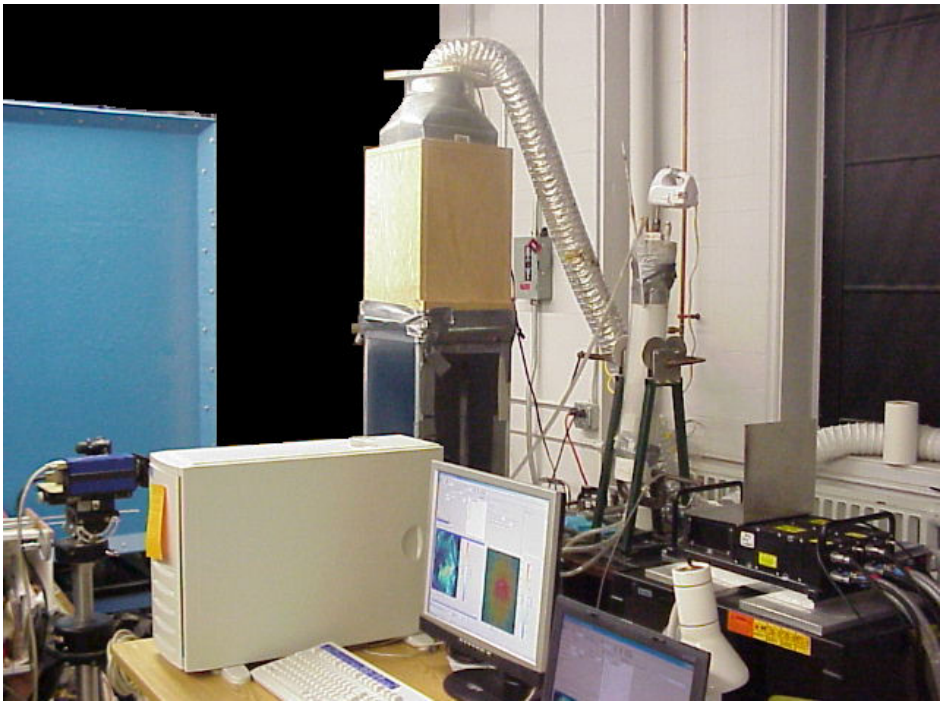

Figure 2.9: Photograph of the experimental setup for PIV measurements.

3. Experimental conditions

The injection time or "on time", represented by τ, was held constant for each P number used. Essentially this parameter controls the volume, $\forall_o = U_o \tau$, injected during each pulse cycle. The duty cycle, α, was held sufficiently low ($\alpha = 0.05$), such that each puff was independent of the preceding one in the range of interest. The P parameter was varied by controlling the injection volume (Eq. 1.4). A summary of selected test conditions is listed in the following section.

3.1 Jet Flow

In this study, air was injected into a co-flowing stream of air. The exit conditions were standard temperature and atmospheric pressure. The injection Reynolds number, based on the velocity of the jet during the injection interval, the air viscosity and the exit nozzle diameter, was *5,000*. This value corresponds to an injected velocity of $U_o = 15.87$ m/s.

The injection parameter P was in the range of 4 and 8. The injected puffs were distinct and no interaction between subsequent puffs was observed. The pulsing frequency, f, was varied from 0.3 to 3.7 Hz, and injection time, τ, was varied from 20±0.5 to 161.1±0.5 ms. Table 2.1 shows the corresponding values of τ and f for varying P numbers for $Re_{jet} = 5000$ and $\alpha = 0.05$.

The momentum flux, as represented by $\iint \rho U_o^2 dA$, was held constant for all cases, since the injector exit area and the mean injection velocity were the same for all experiments. However, the puff impulse $\iiint \rho U_o^2 dA dt \cong \rho U_o \forall_o$, which is linearly

proportional to the injection volume, increased with the injection time and P. The puff impulse only affects the velocity scaling and the trajectory of turbulent puffs, and not the mixing and entrainment rates directly. In fact, the consequences of increasing impulse are reflected in the characteristics of puffs with various P parameters. Table 3.1 shows the corresponding impulse (I) and injected volume ($\forall_o$) for varying P.

Table 3.1: Puff injection characteristics.

P	$\forall_o$(cc)	I (N-s)	$I/(\rho U_o d^3)$
4	6.35	1.40E-04	57.1
5	12.40	2.30E-04	95.4
6	21.43	4.10E-04	172.6
8	50.81	1.01E-03	423.3

One other condition that needs to be highlighted is the steady jet condition. In this case the valve was always open during a given observation time.

3.2 Co-Flow

In this study the co-flow used was supplied through a shop-air source to minimize the effects of confinement on the turbulent puffs. Co-flow strengths were generally quantified as a ratio of co-flow velocity to the injected jet velocity U_{cof}/U_o. This parameter was held constant at a value corresponding to 0.5% of the jet velocity. Since the jet exit velocity exceeds the co-flow velocity by a factor of 200, the co-flow is not believed to have a significant effect on the behavior of the puff.

4. Passive Scalar Field of Non-reacting Puff Flow

The structure of a passive scalar concentration field within isolated puffs is presented in this section. The data correspond to the planar laser Mie scattering technique described earlier. The data averaged from 100 instantaneous concentration fields were interrogated with image processing software. The images were corrected for background non-uniformity prior to averaging. The radial extent of the imaged area was *40 d* and the images covered the range of 25 – 55 *d* in the axial direction. Puffs centered within this field of view are expected to have achieved self-similarity according to Sangras *et al.* (2002).

4.1 Puff Structure

Instantaneous images of puffs with P = 4, 5, 6, and 8 are shown in Fig. 4.1. For the minimum P, the puff appears similar to a buoyant thermal (Scorer, 1957), with little or no fluid left behind in the wake. As the injection time and P increase, the volume of fluid in the wake of the puff increases. Moreover, the width of the puff within the head area decreases. Closer inspection of the image sequences revealed a toroidal vortex-like structure within the puff head for the two lower P cases. For the case of puff with P = 8, the vortex structure was not clearly discernible. It appears that puffs evolve from an approximately spherical geometry to that with a "tail" as the injection time increases.

For $P = 4$ puffs, compact, spheroid structures without a tail were always observed. For puffs with $P \geq 5$, injected fluid was present in a tail of varying size. The width of the tail was always smaller or equal than that of the puff diameter. The axial extent of the tail increased for puffs with larger P. The other noteworthy feature in the images of Fig.

4.1 is the general increase in the scattering intensity within the puff as P increases. This indicates an overall reduction in the dilution and mixing for the higher P cases.

The averaged passive scalar concentration field was normalized by the peak value in the puff center. Contours of the average concentration are shown in Fig. 4.2a, and b for puffs with P = 4 and 5, in Fig. 4.3a, and b for puffs with P = 6 and 8, and in Fig. 4.4 for the steady jet. In all figures, the bold dot represents the location of puff center, which is denoted by the largest relative concentration. The maximum contour has a relative concentration of 0.9 and the adjacent contours are spaced by 0.1. The estimated average uncertainty of the concentration measurements is ±3% of its peak value. The nearly circular contours in Fig. 4.2, when contrasted against the instantaneous image in Fig. 4.1a, and b, are a result of the averaging. These contour plots clearly indicate that puffs elongate and become narrower as the injection volume and P increase. As P increases the contour geometry gets closer to the steady jet. In other word, the structure of the larger puff becomes similar to the steady jet.

4.2 Radial Concentration Profiles

To quantify the radial extent of puffs and to contrast it against that of the steady jet at the same Reynolds number, the radial concentration profile corresponding to the location of peak concentration within the puff was extracted from the averaged fields. The radial concentration profile through the puff center for P = 4 and 5, corresponding to the cases in Fig. 4.2, is shown in Fig. 4.5, and for P = 6 and 8, corresponding to the cases in Fig. 4.3, is shown in Fig. 4.6. The radial concentration profile of the steady jet at z/d = 36 is shown in Fig. 4.7. The best-fit Gaussian curves to the data are also shown in the plots

with a dashed curve. Although all cases exhibit some asymmetry, the $P = 8$ case is much closer to the Gaussian fit than that of the $P = 4$ case. In fact, as the injection time increases, the Gaussian fit improves.

The puff half-width, $\delta_{0.5}$, was defined as the radial extent where the concentration is one-half of the maximum value in the puff center, i.e. full width at half-height as shown in Fig. 4.8a. The puff full-width, $\delta_{0.1}$, was defined as the radial extent where the concentration has reduced to one-tenth of the maximum value in the puff center as shown in Fig. 4.8a. The puff half- and full-widths normalized by the nozzle diameter, $\delta_{0.5}/d$ and $\delta_{0.1}/d$, were extracted from the radial concentration profiles and are shown in Fig. 4.9. The experimental uncertainty of the half-width and full-width measurements based on the pixel movement are ±3.8% and ±3.5%, respectively. Both half- and full-width of puffs decrease with increasing P and the injection volume. The decrease in the half-width is particularly noticeable for the half-width data in Fig. 4.9a.

Since the puff center was at different axial locations for the various cases considered, $\delta_{0.5}$ and $\delta_{0.1}$ were normalized with the puff center location z_c, and compared among the various cases. Table 4.1 compares the normalized half- and full-widths for the cases examined. The values for the steady jet measured in our facility are also included in the Table. The steady jet values are consistent with the data in the literature (Dahm & Dimotakis, 1987). The normalized puff widths decrease as P increases. The half-width for a puff with $P = 4$ is comparable to that of buoyant thermals (Scorer, 1957). As P increases, the half-width decreases to a value close to the steady jet as P increases to 8. Again, the relative decrease of the full-width with increasing P is less than that for the half-width.

Table 4.1: Puff widths normalized by the location of puff center.

P	z_c/d	$\delta_{0.5}/z_c$	$\delta_{0.1}/z_c$
4	38.00	0.32	0.51
5	38.40	0.30	0.48
6	38.00	0.27	0.46
8	31.00	0.23	0.43
Steady jet	36.10	0.22	0.5

4.3 Axial Concentration Profiles

The axial concentration profile corresponding to the location of peak concentration within the puff was also extracted from the images. The axial concentration profile for puffs with $P = 4$ and 5 are shown in Fig. 4.10, and for puffs with $P = 6$ and 8 are shown in Fig. 4.11. The scalar concentration drops rapidly away from the puff center for the $P = 4$ puff when compared with the $P = 6$, and 8 puffs. The puff with $P = 5$ profile is in between $P = 4$ and 6 cases. The axial concentration profiles indicate that as P increases these profiles become less symmetric. In a perfectly symmetric puff, the upper and lower half of the puff would be mirror images of each other. Moreover, puffs with higher P values tend to have a broader peak. For the $P = 6$ and 8 puffs, the entire axial extent of the puff was not captured by the imaging system. This was due to the elongated tail of the puffs.

Puff length, $L_{0.1}$, was defined as the axial extent where the axial concentration is one-tenth of the maximum value in the puff center, i.e. full length at 10% height as shown in Fig. 4.8b. The puff half-length, $L_{0.5}$, was defined as the axial extent where the concentration is equal to one-half of the maximum value in the puff center, i.e. full length at half-height as shown in Fig. 4.8b. The puff lengths normalized with the nozzle diameter, $L_{0.5}/d$ and $L_{0.1}/d$, are shown in Fig. 4.12. The experimental uncertainty of the

$L_{0.5}/d$ and $L_{0.1}/d$ measurements are ±4.2% and ±3.4%, respectively. It is important to note that puffs are sufficiently spaced so that they do not interact with their neighbors. For the case of puff with $P = 8$, the length extended beyond the imaged area. In Fig. 4.12 the presented data for $P = 8$ case was obtained by doubling the value of upper half of the puff. The data indicate that the puff length increases with P until about $P = 6$, beyond which the length, $L_{0.5}/d$, as defined here, becomes nearly constant. The puff length $L_{0.1}$ appears to increase linearly with P. In any case, increasing the value of the injection volume leads to a longer puff. The increasing length associated with the larger injection volumes is also discernible in the instantaneous images of Fig. 4.1.

To estimate the relative elongation of the puff as the injection time increases, the puff aspect ratio, defined as the ratio of width to length for both half-height ($\delta_{0.5}/L_{0.5}$) and 10% height ($\delta_{0.1}/L_{0.1}$), were computed and are shown in Fig. 4.13, and Table 4.2. The estimated experimental uncertainty of the $\delta_{0.5}/L_{0.5}$ and $\delta_{0.1}/L_{0.1}$ measurements are ±5.7% and ±4.9%, respectively. A perfectly spherical puff will have an aspect ratio of one, while an elongated puff will have an aspect ratio smaller than 1. The values in Table 4.2 indicate that the aspect ratio decreases from about 1.12 to 0.33 for $\delta_{0.5}/L_{0.5}$ and from 0.94 to 0.35 for $\delta_{0.1}/L_{0.1}$ as P increases from 4 to 8. Thus, increasing the injection time results in geometrically elongated puff structures.

Table 4.2: Puff aspect ratio.

P	$\delta_{0.5}/L_{0.5}$	$\delta_{0.1}/L_{0.1}$
4	1.12	0.94
5	0.68	0.71
6	0.50	0.57
8	0.33	0.35

4.4 Entrained Volume

To assess the puff volume, $\forall$, the concentration contour corresponding to value of one-tenth of the maximum concentration was selected. The volume was computed by revolving this contour around the vertical axis and calculating the enclosed volume. The volumes from the left and right hand side were averaged. The estimated experimental uncertainty of the volume measurement is ±6%. This volume represents the total puff volume including the injected and entrained volumes. As injection time and P increase, the puff volume also increases. The entrained volume is the difference between the puff volume and injection volume. The normalized entrained volume plotted in Fig. 4.14. Figure 4.14 illustrates the ratio of entrained volume to injection volume $((\forall - \forall_o)/\forall_o)$, effectively showing the mixing of the injected fluid with the ambient at the imaged location. The data indicate that ratio of entrained volume to initial volume decreases as the injection time increases. Although the puff volume increases with P, the initial volume is also larger. For example, going from $P = 4$ to 8, the injected volume increases eight fold. Therefore, puffs with smaller injection time/volume mix more rapidly than those with a larger injection time. This confirms the increasing length of flame puffs for larger P puff.

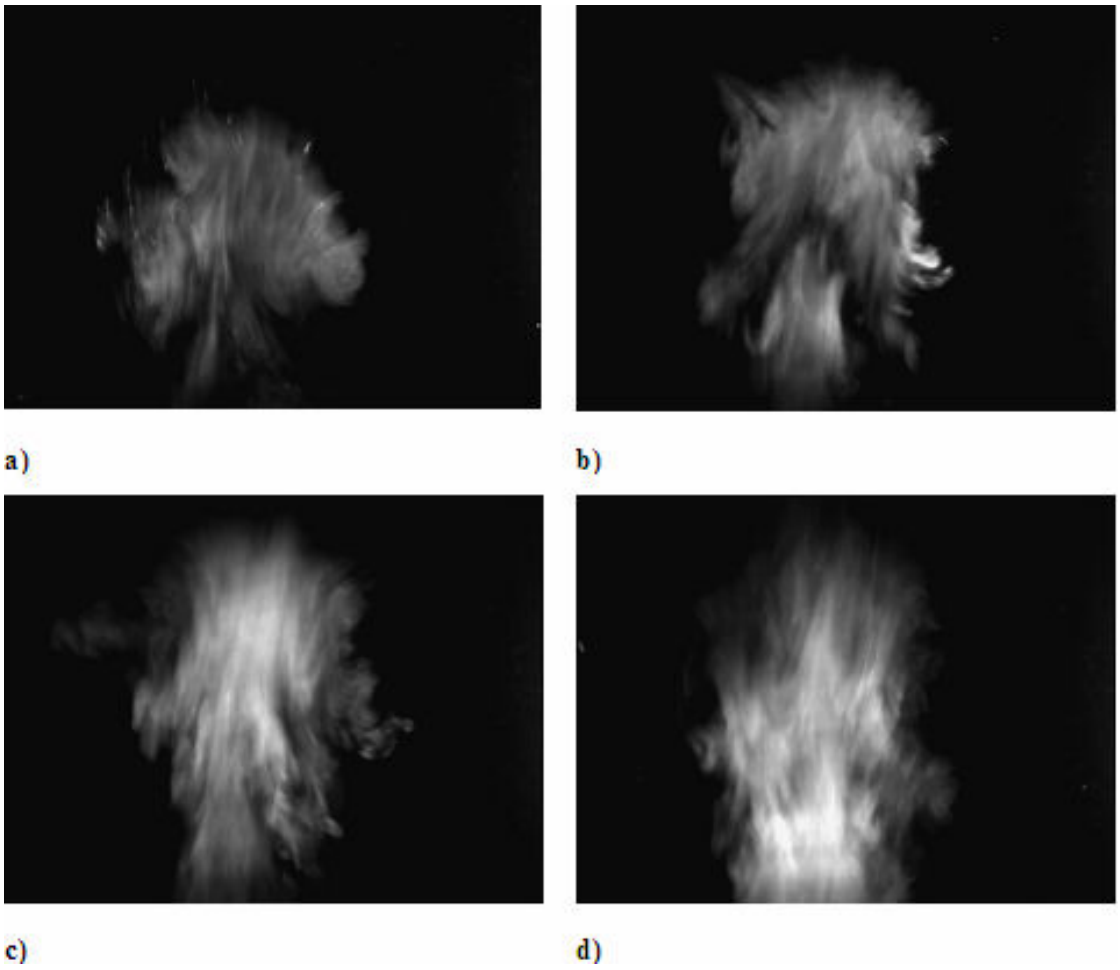

Figure 4.1: Sample instantaneous images of individual puffs with a) P=4, b) P=5, c) P=6 and d) P=8. Axial extent of each image is from 25d to 55d.

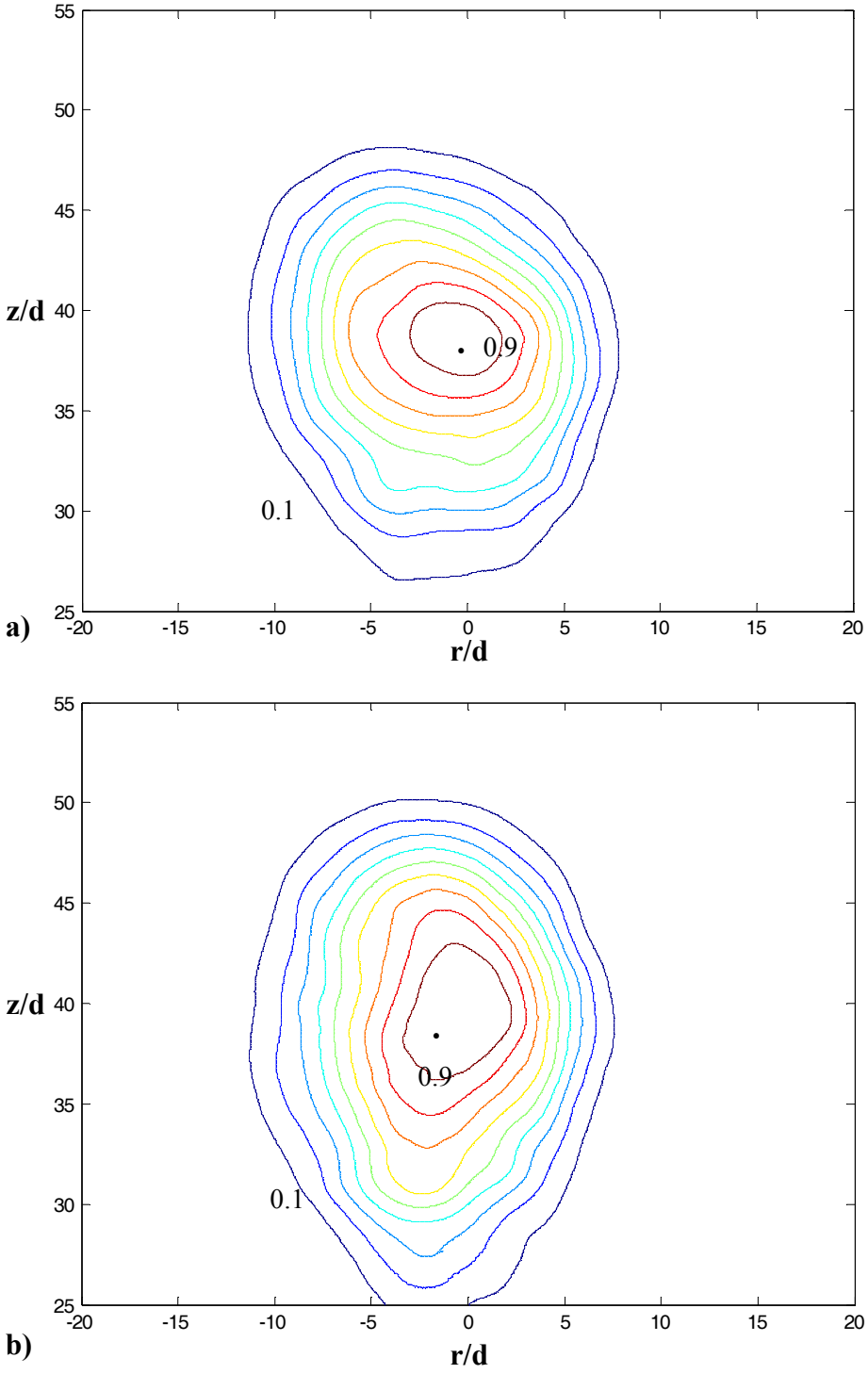

Figure 4.2: Average passive scalar concentration field, normalized by the peak value, for isolated puffs with a) P = 4 and b) P= 5. The bold dot donates the location of puff center. The maximum contour has a relative concentration of 0.9 and the adjacent contours are spaced by 0.1.

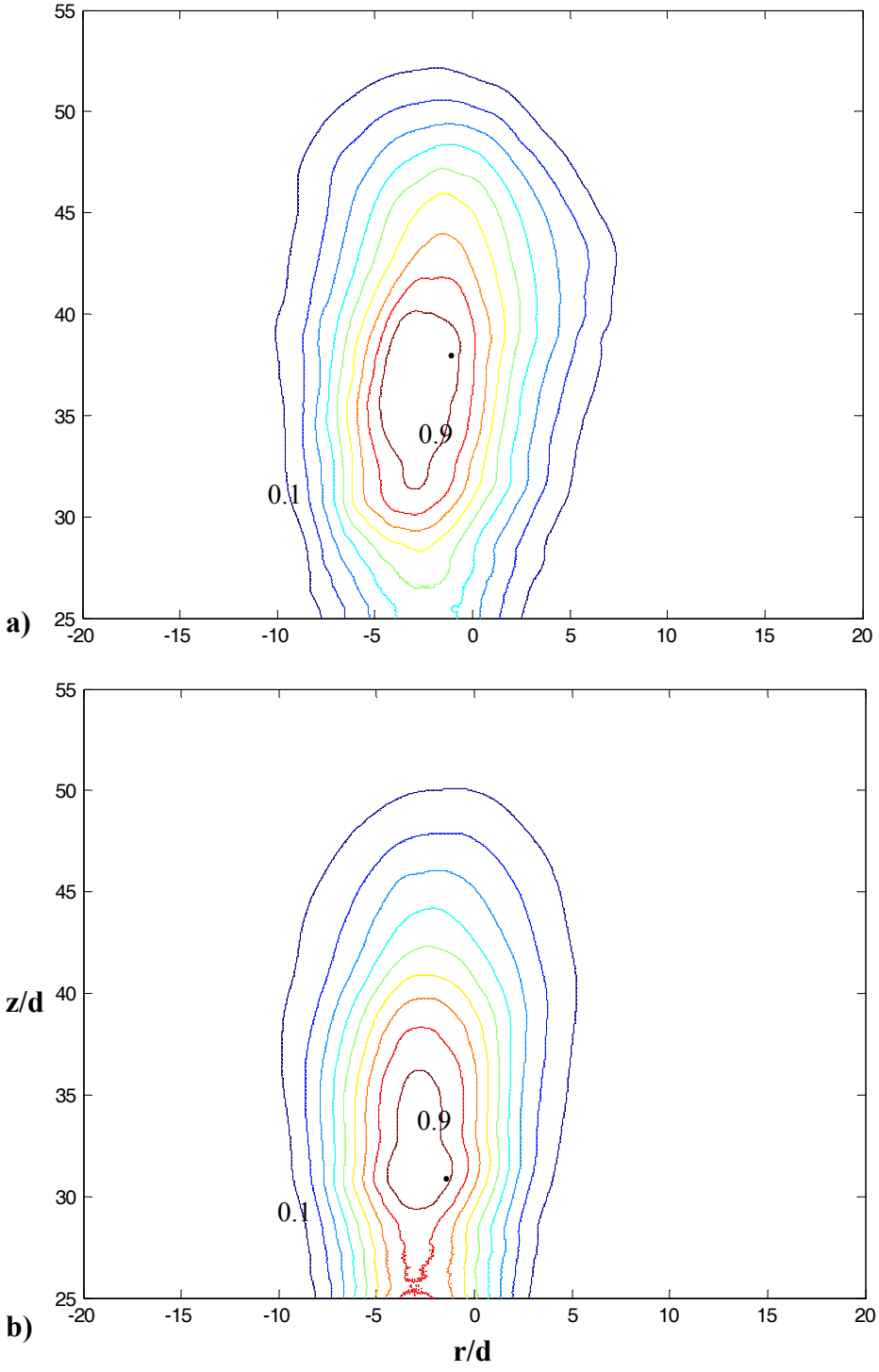

Figure 4.3: Average passive scalar concentration field, normalized by the peak value, for isolated puffs with a) P = 6 and b) P= 8. The bold dot donates the location of puff center. The maximum contour has a relative concentration of 0.9 and the adjacent contours are spaced by 0.1.

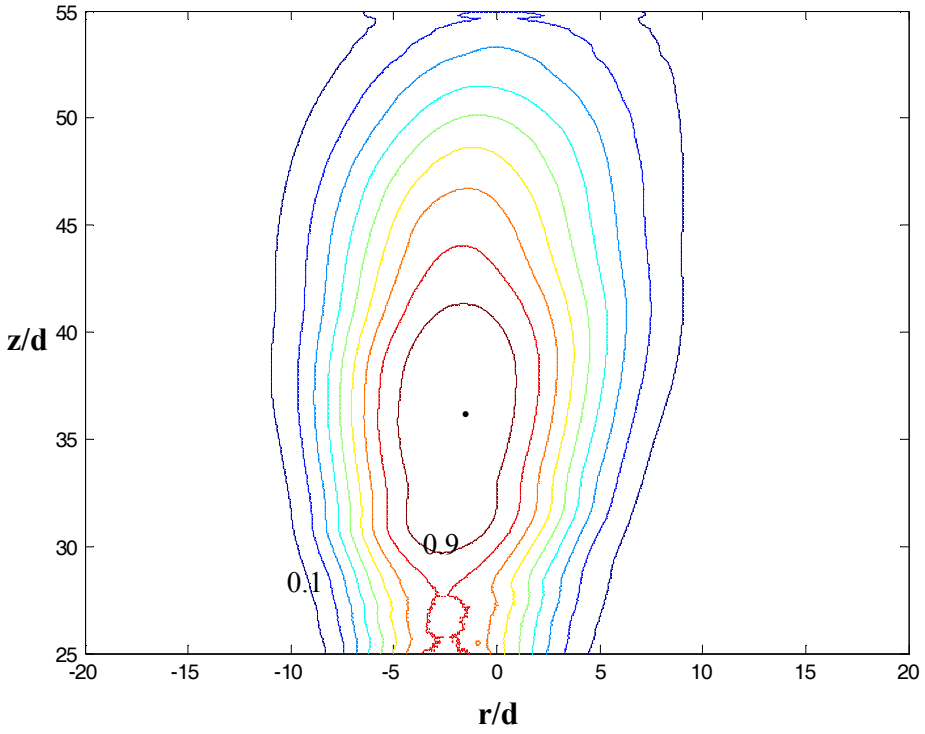

Figure 4.4: Average passive scalar concentration field, normalized by the peak value, for steady jet. The bold dot donates the location of peak value. The maximum contour has a relative concentration of 0.9 and the adjacent contours are spaced by 0.1.

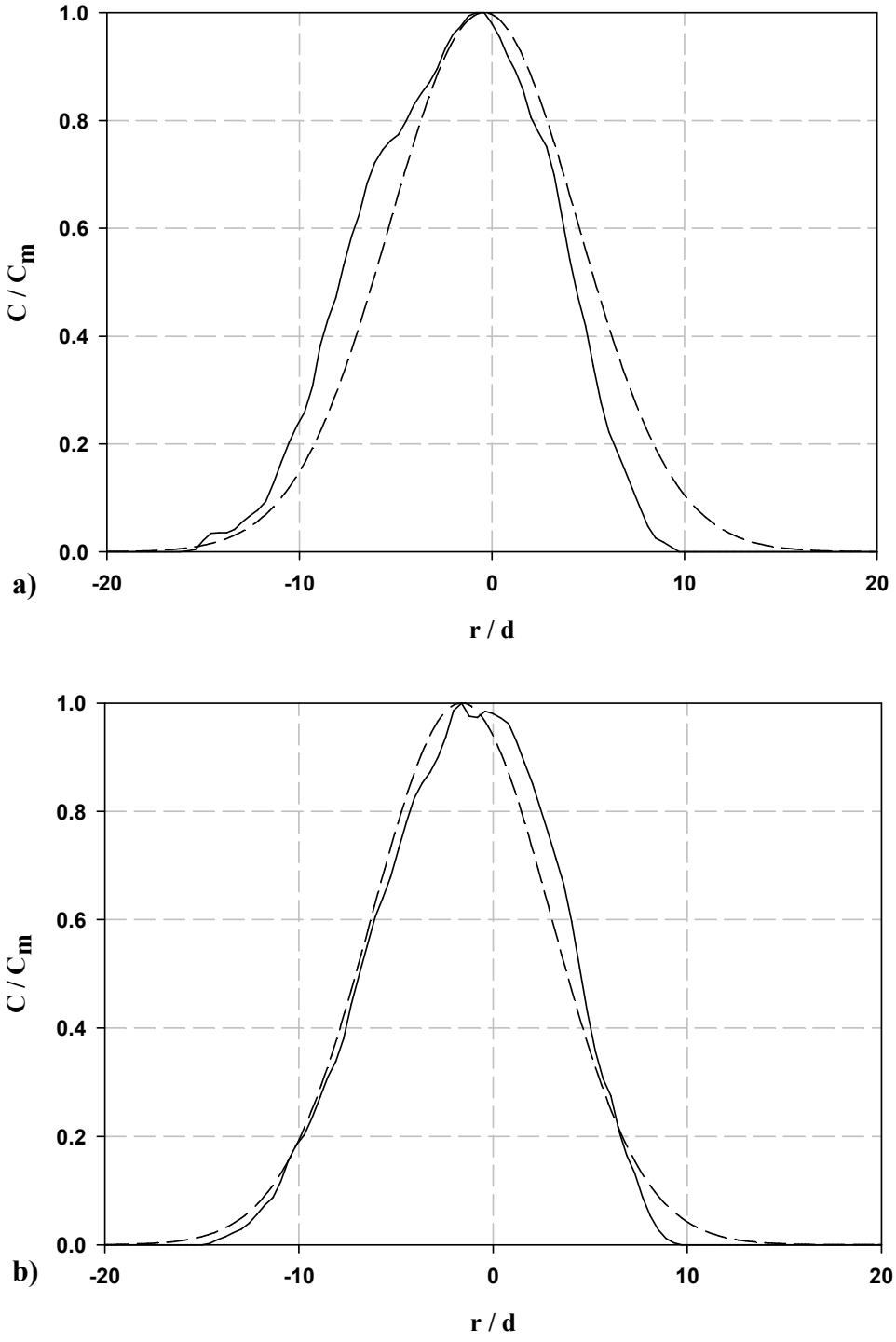

Figure 4.5: Radial concentration profiles (solid line) through puff center with a) $P = 4$ and b) $P = 5$. Dashed curves represent Gaussian curve fit to the data.

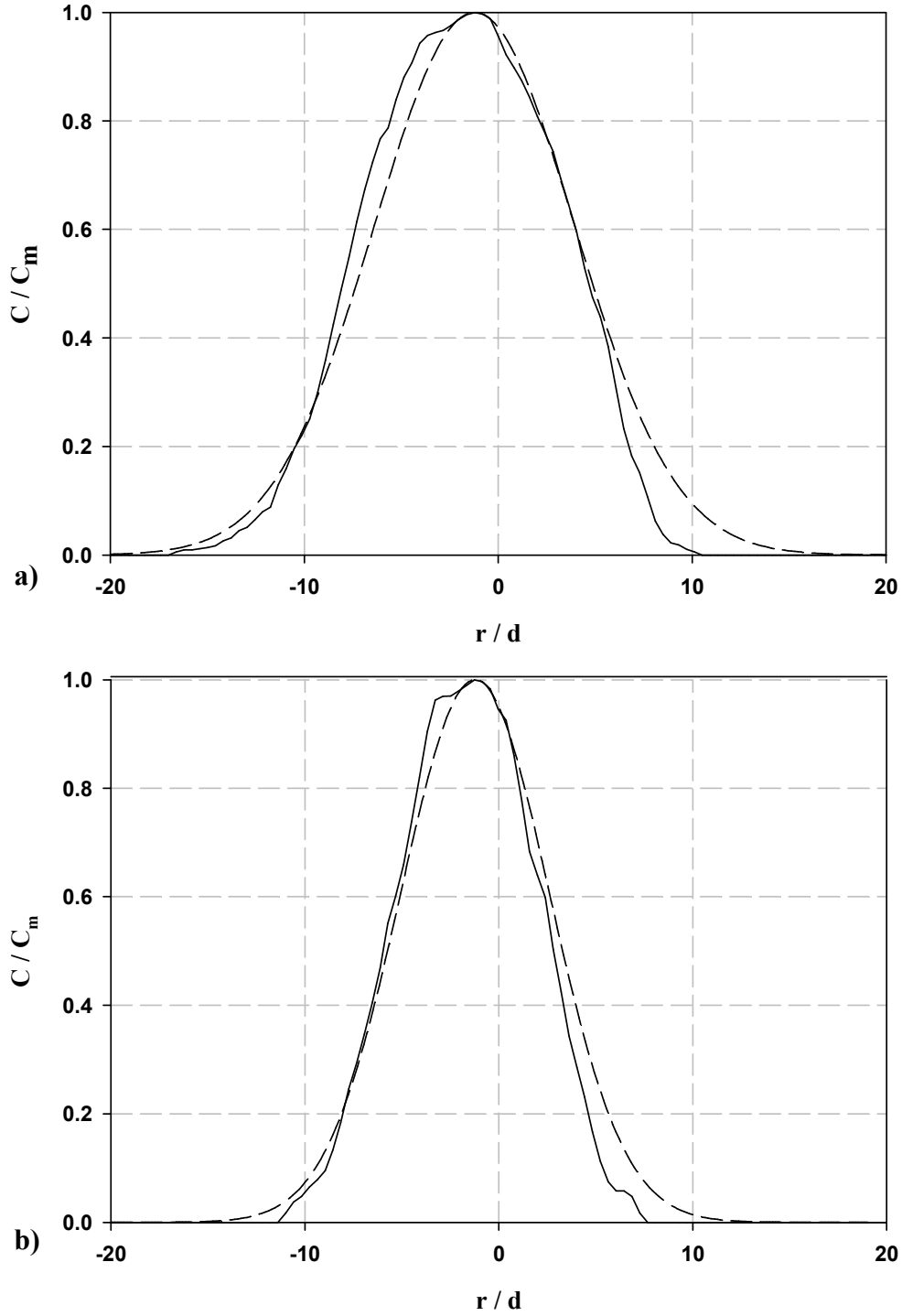

Figure 4.6: Radial concentration profiles (solid line) through puff center with a) $P = 6$ and b) $P = 8$. Dashed curves represent Gaussian curve fit to the data.

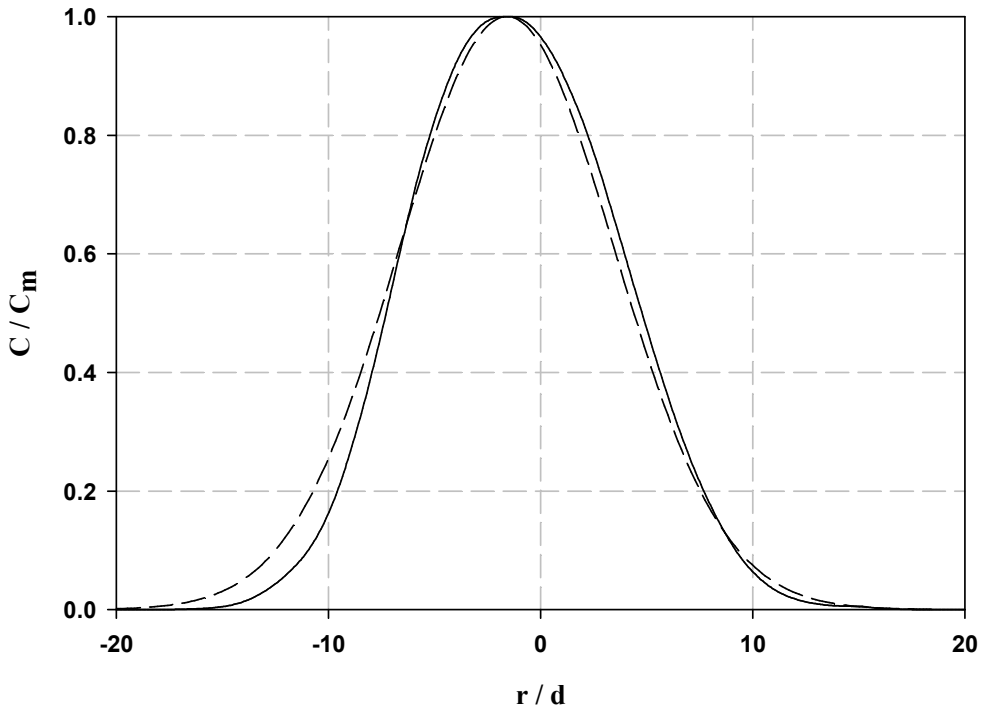

Figure 4.7: Radial concentration profiles of the steady jet. Dashed curves represent Gaussian curve fit to the data.

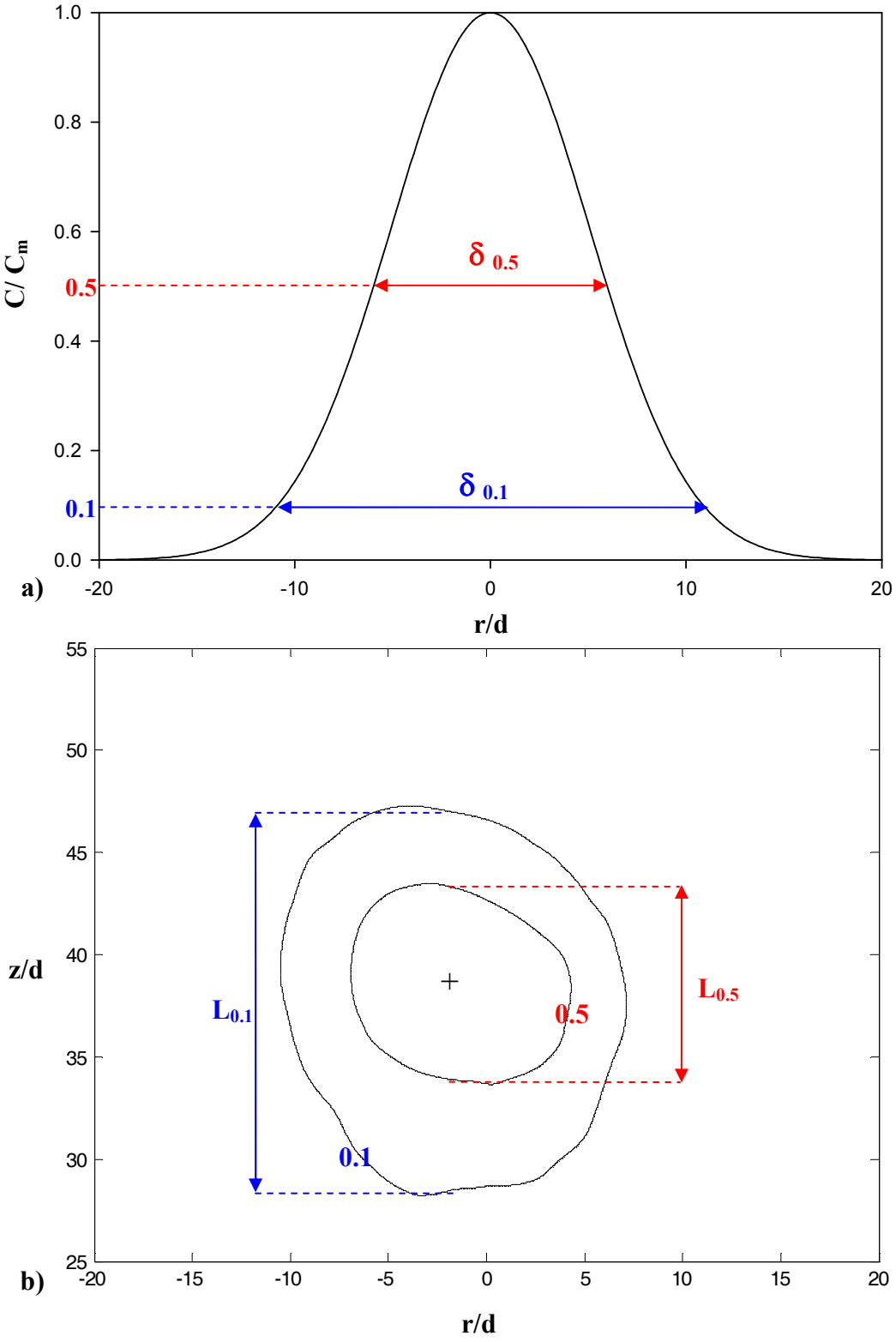

Figure 4.8: Definition of puff width in (a), and puff length in (b).

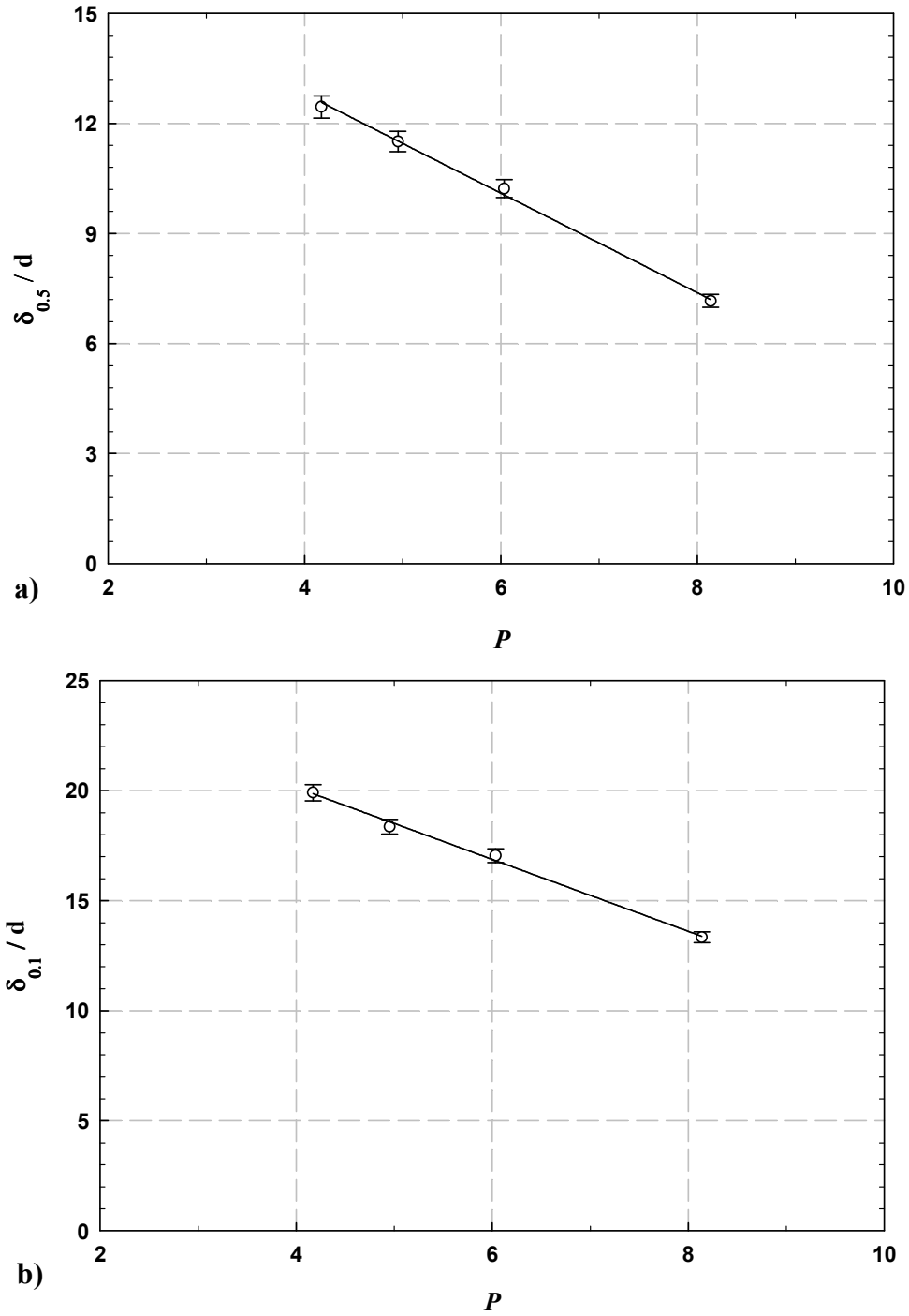

Figure 4.9: Puff width as a function of *P*; a) full-width at half-height; b) full-width at 10% height.

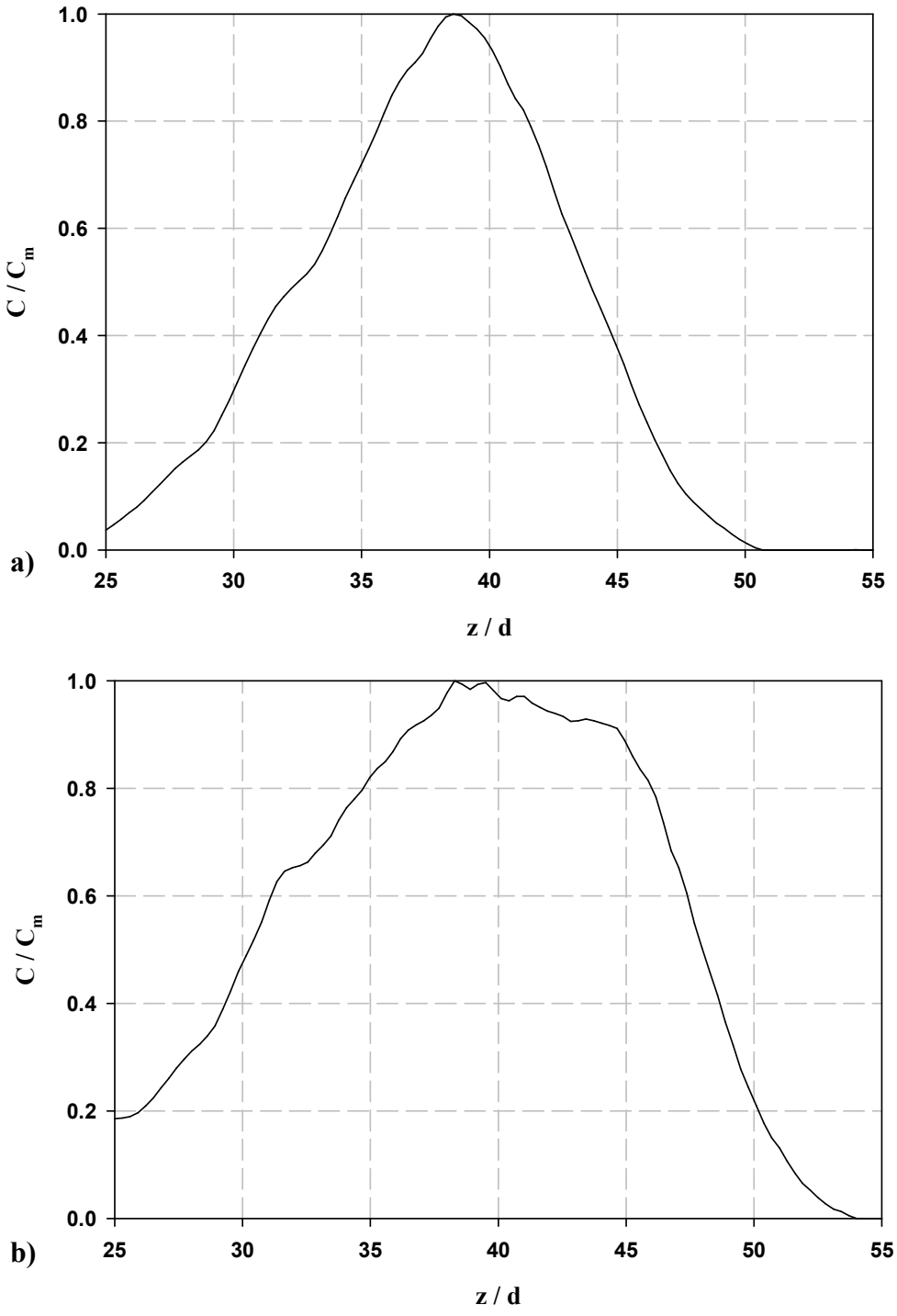

Figure 4.10: Axial concentration profiles through puff center with a) $P = 4$ and b) $P = 5$.

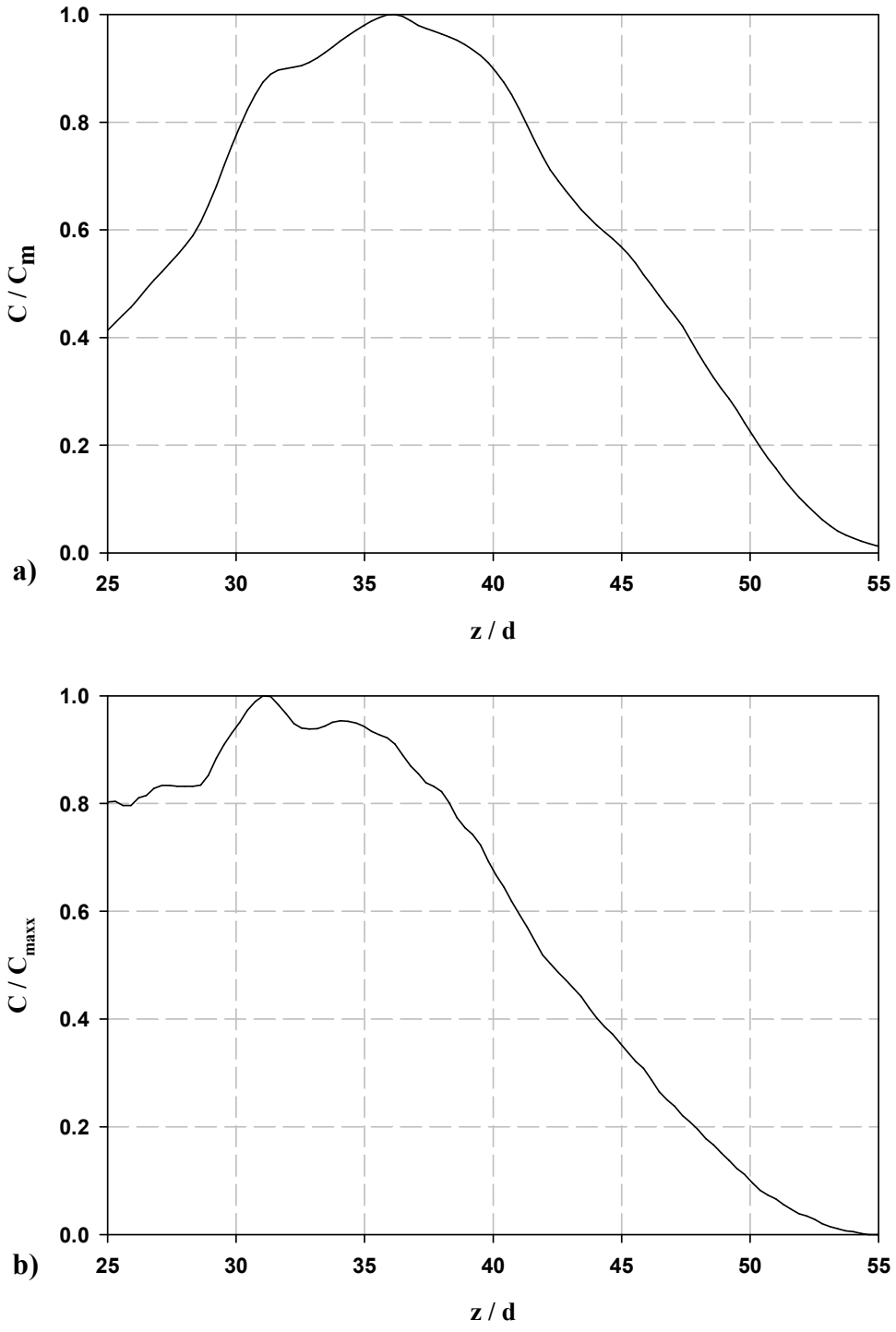

Figure 4.11: Axial concentration profiles through puff center with a) $P = 6$ and b) $P = 8$.

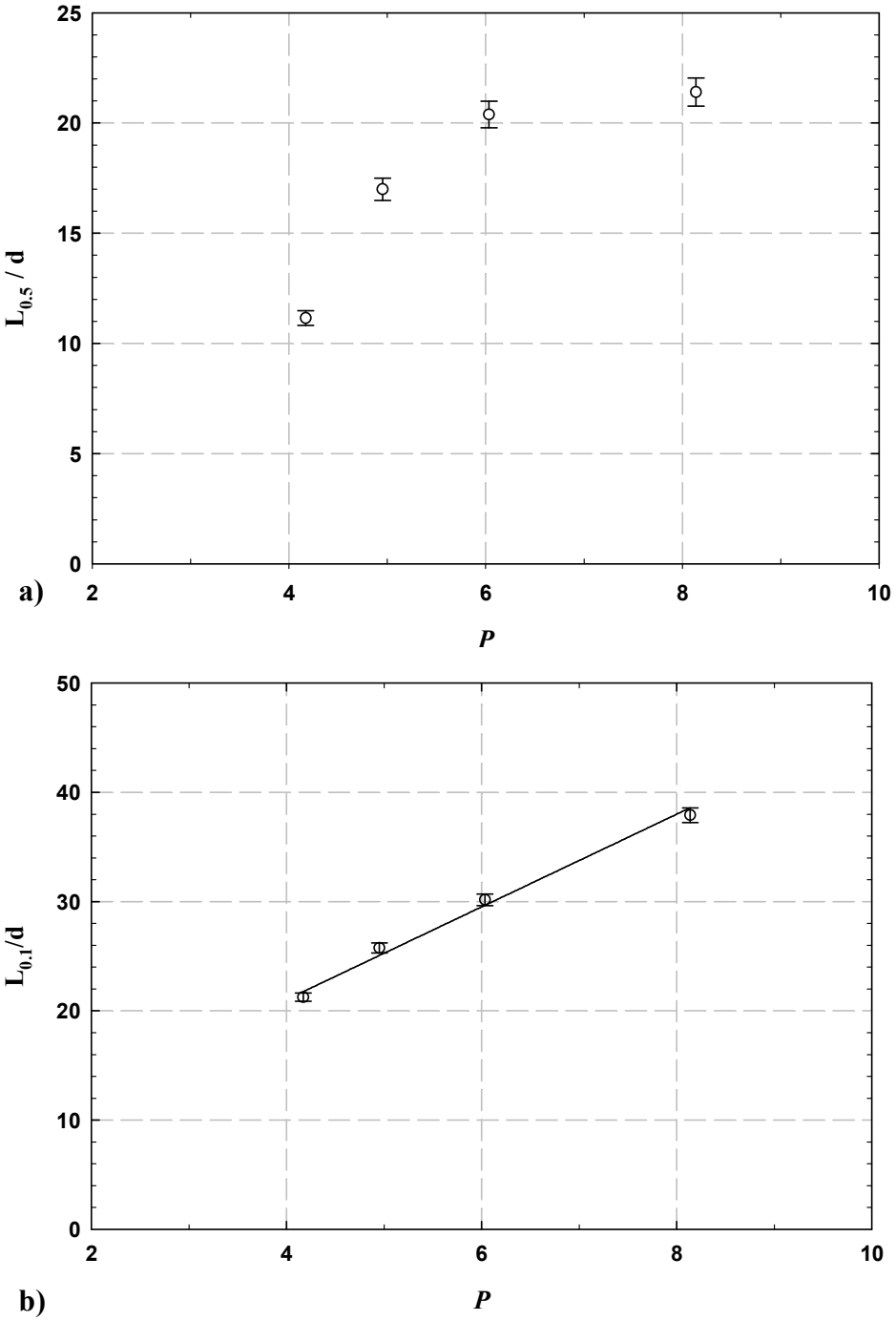

Figure 4.12: Puff length as a function of *P*; a) full length at half-height and b) full length at 10% height.

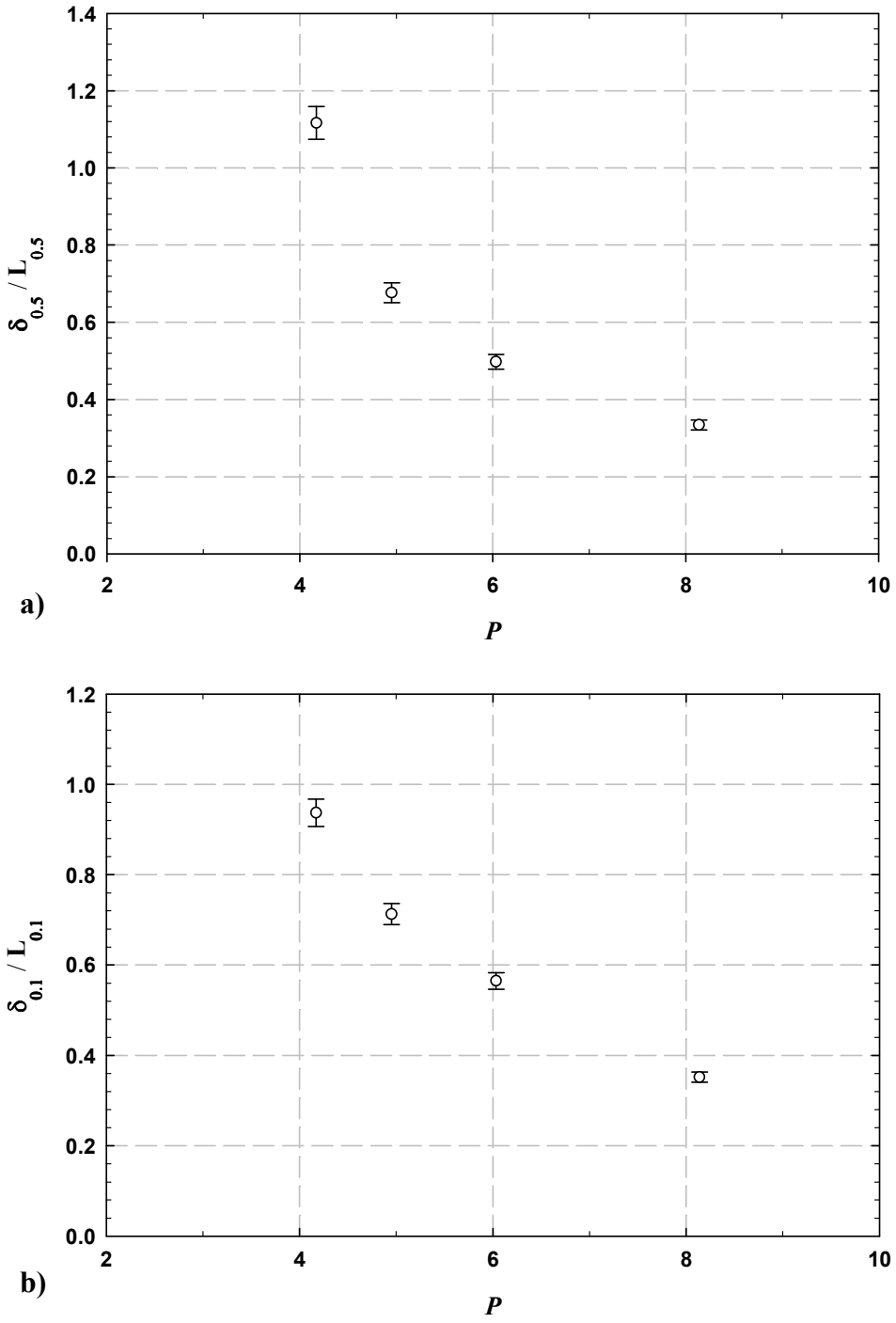

Figure 4.13: Puff aspect ratio as a function of *P*; a) aspect ratio at half-height and b) aspect ratio at 10% height.

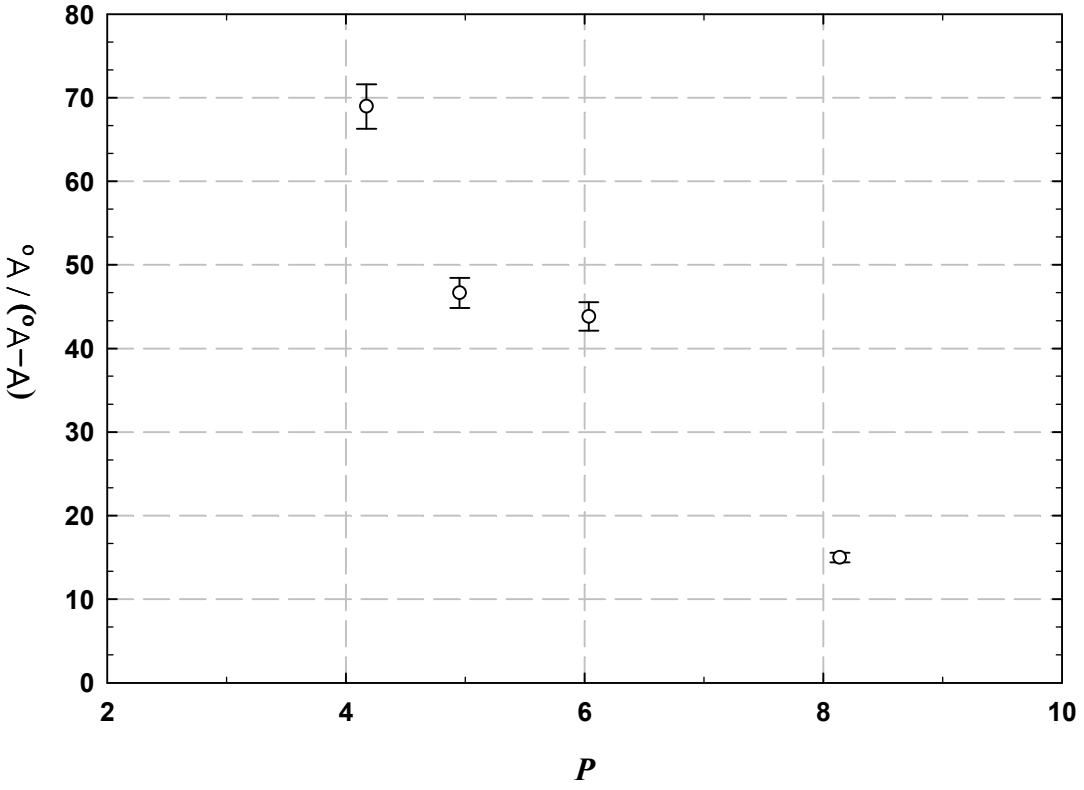

Figure 4.14: Normalized entrained volume by the injected volume as a function of *P*, cube root of stroke ratio.

5. Velocity Field of Non-Reacting Flow

The velocity field of isolated turbulent puffs and steady jet were examined experimentally using the Particle Image Velocimetry (PIV) techniques.

5.1 Steady Jet Verification

In order to verify the measurement technique, the steady jet velocity field is examined in detail first and compared with the measurements in the literature. This was used as a baseline for comparison of the puffs. Recall that data were collected in the range of 40 – 75 *d* in the axial direction for the PIV sets. The results of time averaged velocity field of 6500 data fields for steady jet are discussed below.

5.1.1 Time Averaged Velocity Field of Steady Jet

Figure 5.1 shows the decay of mean centerline velocity as a function of the axial distance from the nozzle. The results include the experimental uncertainty of ±1.25% (Scarano & Riethmuller, 1999). The centerline velocity profiles for a self-similar jet are described by:

$$\frac{U_c}{U_o} = B_u d /(z - z_o) \tag{5.1}$$

where U_c is the centerline velocity, U_o is the nozzle velocity, z_o is the so-called virtual origin, B_u is the decay constant which, in general, has a value between 5 to 6.2 depending on the experimental setup (Wygnanski & Fiedler,1969; Fischer *et al.* ,1979; Hussein *et al.*, 1994; Boersma *et al.*, 1998; Webster *et al.*, 2001). Self-similar flows can be thought of as generated by a point or line source located at the virtual origin of the flow (Chen & Rodi, 1980). The virtual origin typically depends on the jet Reynolds number and the setup of the jet. The present data, fitted to Eq. (5.1) with B_u and z_o as parameters, show

the z^{-1} decay of the jet. The fitting results in a virtual origin of 6.98 mm = 1.4d. In a recent DNS study by Boersma *et al.* (1998), the $z_o = 4.9d$ for the $Re_{jet} = 2.3\times10^3$, and $z_o = 4d$ in the experimental study of Hussein *et al.* (1994) at $Re_{jet} = 10^5$. Thus, our experimental data are consistent with the data in literatures.

The steady jet half-radius, $r_{1/2}$, was defined as the radial extent where the mean velocity is one-half of the maximum value. The development of the normalized half-radius, $r_{1/2}/d$, is shown in Fig. 5.2. As expected, the jet width increases linearly with downstream distance, while the velocity magnitude decreases. It is important to examine the development of the jet in detail, since the present jet is not an ideal free jet. In the far downstream region, the walls of the flow chamber restrict the flow development. The half-radius results show a linear development (solid line in Fig. 5.2) on this length scale, i.e. $r_{1/2} = 0.099z$ or $r_{1/2} = 0.0934(z\text{-}18.555)$. Thus, there is little or no effect of wall containment on the jet development within the present experimental extent. Therefore, it can be expected that a self-preserving turbulent jet is present in the present experiment. The coefficient 0.099 for the streamwise development of half-width agrees with the average previous result ($r_{1/2} = 0.107z$) by Fischer *et al.*, (1979) and Webster *et al.* (2001). Therefore it can be expected that self-similarity turbulent jets are established in the present experiment.

The mean axial velocity normalized by the centerline velocity, U/U_c, is plotted versus non-dimensional radial coordinate, $r/r_{1/2}$, for eight axial downstream locations in Fig. 5.3. The uncertainty on the mean is estimated ±1.8%. All the profiles collapse onto a single profile within the experimental region. The mean axial velocity distribution is, therefore, self-similar and can be described by a functional form of the type:

$$U = U_c \exp[-k_u(r/z)^2] \quad (5.2)$$

The average of the least-square fit to all the data gives the Gaussian fitting constant k_u = 68.5 ($U = U_c \exp[68.5(r/z)^2]$), whereas in the experiment by Panchapakesan & Lumley (1993) a value of 75.2 ($Re_{jet} = 1.1\times10^4$), and in the DNS study by Boersma *et al.* (1998) a value of 76.1 ($Re_{jet} = 2.4\times10^3$) have been found, respectively. Thus, the present study is consistent with the previous work on steady jet.

Figure 5.4 shows the mean radial velocity profile normalized by the centerline velocity, V/U_c, for eight axial downstream locations. The uncertainty on the V/U_c is estimated ±1.78%. The averaged peak values (in a range of 0.02 to 0.03) and the distribution of the velocity profile agree well with the results available from other studies reported in the literature (Wygnanski & Fiedler, 1969; Panchapakesan & Lumley, 1993; Hussein *et al.*, 1994). The data profiles nearly collapse onto a single profile except for the profile at z/d = 75. This could be due to the effect of the wall confinement on the velocity profile at z/d = 75, and also due to the small absolute value of the V with respect to the axial velocity to the PIV resolution. This plot shows the radial flow in the vicinity of the centerline is outward due to the decay of the centerline velocity. The maximum value of V is about 2% of U_c.

5.1.2 Steady Jet Velocity Fluctuations

Aside from the averaged velocity field, the root-mean-square (rms) of fluctuating velocities and turbulent shear stresses were also examined. The velocity fluctuation is defined as the deviation of velocity from its average value. The rms of radial and axial velocity is as follows:

$$u'_{rms} = \sqrt{\frac{\sum_{i=1}^{n}(U-\overline{U})^2}{n}} \; ; \quad v'_{rms} = \sqrt{\frac{\sum_{i=1}^{n}(V-\overline{V})^2}{n}} \tag{5.3}$$

The radial profiles of the fluctuating axial and radial velocity are shown in Fig. 5.5 and Fig. 5.6, respectively. The experimental uncertainty of the axial and radial velocity fluctuations based on the fractional error from N individual samples ($error = \frac{Z_c \sigma}{\mu\sqrt{N}}$, where Z_c is the confidence coefficient, which can be obtained from normal curve tables, σ is the variance of the fluctuating velocity and μ is the mean) are ±1.95% and ±2.14%, respectively (Scarano & Riethmuller, 1999). The local velocity scale is the mean centerline velocity. For both u'_{rms}, and v'_{rms}, in the range of z/d = 45-60, the profiles have a peak value away from the centerline. The axial velocity fluctuation (u'_{rms}/U_c) is nearly self-similar. There is a slight scatter near the centerline. The radial velocity fluctuation (v'_{rms}/U_c) does not exhibit self-similarity and increases in height with downstream location (z/d) near the centerline. The axial and radial velocity fluctuations are positive and symmetric about the centerline, as expected. The experiments by Wygnanski & Fiedler (1969), and Hussein *et al.* (1994) have found that a value of 0.28 for the u'_{rms}/U_c peak and a value of 0.22 for the v'_{rms}/U_c peak. The present results for both axial (u'_{rms}/U_c) and radial (v'_{rms}/U_c) velocity fluctuation peak agree with the past results.

The Reynolds shear stress, $<u'v'>$, profile is shown in Fig. 5.7 for eight axial locations. The uncertainty on the $<u'v'>$ is estimated ±2.89%. In contrast to the data in Fig. 5.6, the Reynolds shear stress data are very nearly self-similar, especially near the jet centerline. There is a bit of scatter near the peak value at $r = 0.5r_{1/2}$. The profile does not pass through the origin at the centerline, perhaps due to larger uncertainty near the jet

centerline. The location of the peak value of the Reynolds shear stress is $r/r_{1/2}$.= 0.06-0.07, which agrees with that of the radial velocity profile in Fig. 5.4. The Reynolds shear stress is anti-symmetric about the centerline. It is positive where the mean shear ($\partial U/\partial r$) is negative and negative where the mean shear is positive. The sign of the shear stress agrees with the net transport of high momentum away from the centerline. The Reynolds shear stress measurements agree with the profiles of Wygnanski & Fiedler (1969), and Hussein *et al.* (1994), with the peak value of $<u'v'>$ around $0.02U_c^2$.

5.2 Puff Velocity Field

In this section, the ensemble averaged velocity fields of non-reacting, isolated turbulent puffs with P = 4, 5, 6, and 8 are discussed. The data were obtained from phase locked measurements of 2000 instantaneous PIV data fields. The estimated experimental uncertainties of the axial and radial puff velocity are shown in Table 5.1.

Table 5.1: Uncertainty of axial and radial velocity.

P	Uncertainty % (U/U_c)	Uncertainty % (V/U_c)
4	±2.57	±3.33
5	±2.62	±2.52
6	±2.85	±4.00
8	±3.41	±3.72

5.2.1 Velocity Fields of Puffs

The axial and radial velocity contours for puffs with P = 4, 5, 6, 8, and the steady jet are shown in Fig. 5.8 and Fig. 5.9, respectively. The horizontal axis is the normalized radial extent (r/d), and vertical axis is the normalized axial distance (z/d) from nozzle. The flow direction is from the bottom to the top. The puff center is the location where the peak value of the axial velocity occurs. The axial location of puff center for puff with P = 4, 5, 6, and 8 is shown in Table 5.2. The puff center in these figures denoted by a bold plus (+) symbol.

Table 5.2: Axial location of puff center from nozzle.

P	$(z/d)_c$
4	59.7
5	65.7
6	62.7
8	46

It appears from Fig. 5.8 that the axial velocity contours evolve from an oblong geometry to one with a "tail" as the injection time increased. The axial velocity contour for puffs with P = 4, 5 and 6 are similar, except for the P = 8 puff. The contours get elongated as P increases. The largest velocities are found within the central portion of the puff; however for the steady jet, the largest velocity is at the trailing edge. The axial velocity of the jet gradually drops as z^{-1} as indicated earlier.

Figure 5.9 shows the radial velocity contour for puffs with P = 4, 5, 6, 8, and the steady jet. The puff center is denoted by a bold plus symbol (+) in Figure 5.9. The radial velocity sign for puff can be found both positive and negative at both sides of the puff center. For a vortex ring, there is a change of the sign each side of the centerline. This shows the toroidal vortex motion within the puff. Above the puff center, the positive sign of the radial velocity is located at the right side of the puff center, which indicates that the puff head pushes out the surrounding flow. For the bottom section of the puff center, the positive region is located at the left side of the puff center. This indicates that there is an inward radial velocity for the bottom section of the puff center. This behavior gets stronger for the P = 4 puff. As P increases, there is a weak inward flow, which occurs at the tailing edge of puff. The high velocity regions of the jet are on the edges of the steady jet and the change of sign occurs at the jet centerline. The radial velocity on the jet centerline is zero. For the steady jet case, there is an inward radial flow, which is seen outside the jet. This is due to the interface of the flow with the flow chamber wall that causes a reverse flow.

In order to normalize the velocity of the puff, the puff center axial velocity (U_c) was calculated. Then the velocity distribution of each puff was normalized by the axial

velocity at the puff center. For the steady jet, the velocity at each axial location was normalized by the centerline velocity at the same location. This is done to show the self-similarity behavior of the jet.

The radial distribution of axial velocity of puffs corresponding to the location of puff center was extracted from the averaged field. Figure 5.10 shows the normalized axial velocity (U/U_c) corresponding to the location of puff center as a function of r/d. The profile for the steady jet (dashed line in Fig 5.10) corresponds to the Gaussian fit curve in Fig. 5.3. The measured data at puff center for the puffs follow the exponential distribution expressed as

$$U = U_c \exp[-k_u ((r-r_o)/r_{1/2})^2] \quad (5.4)$$

where k_u is the fitting constant. The Gaussian fitting constant for puffs is shown in Table 5.3.

Table 5.3: Gaussian fitting constants for puffs.

P	k_u	$r_o/r_{1/2}$
4	0.63	0.087
5	0.71	0.195
6	0.70	-0.0362
8	0.61	-0.002
Steady	0.68	0.004

As the puffs may be off center, the r_o (virtual origin) parameter has been used. The peak value of U/U_c for puff does not occur at the centerline, due to jitter in the radial position of the puff and the averaging of such images. In the experiments by Bremhorst & Hollis (1990), a value of $k_u = 0.69$ has been found for the $Re_{jet} = 6\times10^4$, and $P = 3.6$. The profile distribution of U/U_c for $P = 8$ puff resembles that of the steady jet.

The puff half-radius, $r_{1/2}$, was defined as the half of radial extent where the mean velocity is one-half of the maximum value at the puff center. Then the puff center half-width, $\delta_{1/2}$, was defined as twice the puff half-radius ($\delta_{1/2} = 2r_{1/2}$). The puff width ($\delta_{1/2}$) was extracted from the averaged axial velocity field profiles from Fig. 5.10. For the steady jet, the half-width data are obtained from Fig. 5.2 ($\delta_{1/2} = 2r_{1/2}$). The half-width normalized by nozzle diameter, $\delta_{1/2}/d$, for puffs with P = 4, 5, 6 and 8 is shown in Fig. 5.11. The result shows that the puff center half-widths decrease with increasing P, and get closer to the steady jet value. The ratio of puff half-width to the steady jet half-width corresponding to the puff center location was calculated ($(\delta_{1/2})_{puff}/(\delta_{1/2})_{steady}$), and the result is shown in Fig. 5.12. This plot shows that for the same axial location, the puff half-width is larger than that of the steady jet by up to 19%.

The mean axial velocity normalized by the centerline velocity, U/U_c, is plotted versus non-dimensional radial coordinate, $r/r_{1/2}$ for puffs at the puff centerline in Fig. 5.13. This plot shows how the distribution of U/U_c depends on P. The profile for the steady jet corresponds to the Gaussian fit curve in Fig. 5.3. The normalized axial velocity profile at puff center in the radial range of $-1 \le r/r_{1/2} \le 1$ nearly collapses onto the steady jet profile. However, moving beyond the puff half-width, there is a slight scatter in data. It is to be noted that the radial peak location of puffs are not located at zero. The profile of puff with P = 8 is very close to the steady jet.

5.2.2 Fluctuating Velocity Field of Puffs

The root-mean-square of radial and axial velocity for puff are obtained from Eq. 5.3. The estimated experimental uncertainties of the axial velocity fluctuation are shown in Table 5.4 (Scarano & Riethmuller, 1999).

Table 5.4: Uncertainty of axial and radial fluctuating velocities.

P	Uncertainty % (u'_{rms}/U_c)	Uncertainty % (v'_{rms}/U_c)
4	±2.11	±1.96
5	±2.02	±1.90
6	±2.12	±1.99
8	±2.48	±2.34

Contours of axial velocity fluctuation, u'_{rms}, normalized by the maximum velocity in the puff center, are shown in Figure 5.14 for puffs with P = 4, 5, 6 and 8 and the steady jet. The puff center is denoted by a bold plus (+) symbol in the plots. These contour plots clearly indicate that the peak value for the puffs occur above the puff center. The high value contours for the puff with P = 4 have a rounded shape while for higher P is more elongated. By moving from the center of the puff to trailing edge of it, the fluctuations decrease and form a chevron shape. The "Λ" shape grows with increasing P. For the case of P = 4 puff, the trailing edge of the puff looks flat. For the steady jet case, the axial velocity fluctuation at each axial extent was normalized by the centerline axial velocity of the same axial location. The steady jet contour of axial velocity fluctuation indicates the growth of a highly turbulent region with increasing z.

Figure 5.15 shows the root-mean-square values of axial mean velocity fluctuation normalized by the centerline velocity, u'_{rms}/U_c, as a function of r/d for puffs with P = 4, 5,

6 and compared individually with the steady jet. The u'_{rms}/U_c profiles correspond to the location of puff center. The difference between the peak value of the puff and the steady jet is highest for the $P = 4$ puff. The puff with $P = 8$ is much closer to the steady jet than that of the other cases.

Figure 5.16 presents the root-mean-square values of axial velocity fluctuation normalized by the centerline velocity, u'_{rms}/U_c, plotted against $r/r_{1/2}$ at puff center. For comparison, the self-similar profile of the steady jet is also shown in Fig. 5.16. This plot shows how the behavior of u'_{rms} changes with increasing P. The profiles of u'_{rms} for the puffs are quantitatively similar to that of the steady jet. The axial velocity fluctuation is positive and almost symmetric about the centerline. It can be seen from Fig. 5.16 that the puff with $P = 4$ has the highest u'_{rms} peak value of $0.52U_c$ among the puffs examined. The maximum magnitude of u'_{rms}/U_c for the $P = 4$ puff is about 1.8 times the ones for the steady jet. The $(u'_{rms}/U_c)_{max}$ for the puffs and the steady jet is shown in Table 5.5. Figure 5.16 clearly indicates that the u'_{rms}/U_c profiles get closer to the steady jet profile as P increases. Moreover, the profile becomes wider as P increases.

Table 5.5: The peak value of normalized axial velocity fluctuation.

P	$(u'_{rms}/U_c)_{max}$
4	0.52
5	0.48
6	0.40
8	0.28
Steady	0.28

Figure 5.17 shows contours of radial velocity fluctuation, v'_{rms}, normalized by the centerline velocity for puffs with $P = 4$, 5, 6 and 8 and steady jet. It is to be noted that for

the steady jet case, the radial velocity fluctuation at each axial extent was normalized by the centerline axial velocity of the same axial location, while for the puffs, it was normalized by the puff center axial velocity. These contour plots clearly indicate that the peak of v'_{rms} for puffs occurs near the puff center as indicated by the bold plus (+) symbol in the plots. The higher v'_{rms} regions (red color in Fig. 5.17) have rounded shapes which get elongated as P increases. The puff with $P = 4$ has the highest value of v'_{rms}. The peak value of v'_{rms} decreases as P increases, and eventually gets closer to the steady jet for $P = 8$. The steady jet contour of radial velocity fluctuation indicates the growth of a highly turbulent region with increasing z.

Figure 5.18 and Fig. 5.19 show the root-mean-square values of radial mean velocity fluctuation profiles normalized by the centerline velocity, v'_{rms}/U_c, versus r/d, and $r/r_{1/2}$, respectively, for puffs at puff center and the steady jet. Figure 5.18 presents the profiles of v'_{rms}/U_c versus r/d for different puffs, and compares the puffs individually with the steady jet, while Fig. 5.19 shows v'_{rms}/U_c versus $r/r_{1/2}$ for different puffs. The puff profiles have higher levels of v'_{rms}/U_c than that of the steady jet. Puffs with larger P have profiles close to the steady jet, and the puff with $P = 4$ has the highest value of v'_{rms}/U. The profiles for puffs and the steady jet are positive and quite symmetric about the centerline. It can be seen in both figures that the difference between peak value of puffs and steady jet has the highest value for puff with $P = 4$. The puff with $P = 8$ is much closer to the steady jet than that of the other cases. The increase in maximum magnitude of v'_{rms}/U_c for $P = 4$ puff is two times the steady jet. The $(v'_{rms}/U_c)_{max}$ for the puffs examined and the steady jet is shown in Table 5.6.

Table 5. 6: The peak value of normalized radial velocity fluctuation.

P	$(v'_{rms}/U_c)_{max}$
4	0.43
5	0.40
6	0.33
8	0.22
Steady	0.20

5.2.3 Turbulent Shear Stress within Puffs

Figure 5.20 shows contours of turbulent shear stress, $<u'v'>$, normalized by the square of the mean centerline velocity for puffs with P = 4, 5, 6 and 8 and the steady jet. The estimated experimental uncertainty of the turbulent shear stress ($\sqrt{(\Delta u'_{rms}\%^2 + \Delta v'_{rms}\%^2)}$) is shown in table 5.7 .

Table 5.7: Uncertainty of puff turbulent shear stress.

P	Uncertainty % $<u'v'>/U_c^2$
4	±2.88
5	±2.77
6	±2.91
8	±3.41

The Reynolds shear stress of the steady jet at each axial location is normalized by the square of the centerline axial velocity of the same axial location, while for the puffs, it was normalized by the square of puff center axial velocity. The puff center is denoted by a bold plus (+) symbol in the plots. These contour plots clearly indicate that fluctuations peak for puffs located off the centerline, and there is a change of sign at puff center. The plot of the turbulent shear stress is antisymmetric about the centerline, as expected. The

sign of the turbulent shear stress indicates that the direction of the turbulent stress transport is away from the centerline. The turbulent shear stress distribution for the steady jet indicates the change of sign at the jet centerline, and the magnitude of turbulent shear stress increases with z. The puff with $P = 4$ has the highest value of $<u'v'>$. The peak value decreases as P increases, and eventually gets closer to the steady jet for puff with $P = 8$.

Figure 5.21 and Fig. 5.22 show the Reynolds shear stress profiles normalized by the square of the mean centerline velocity, $<u'v'>/U_c^2$, versus r/d *and* $r/r_{1/2}$, respectively, for puffs at puff center and the steady jet. It is to be noted that for the steady jet case, the Reynolds shear stress at each axial position was normalized by the square of the centerline axial velocity of the same axial location, while for the puffs it was normalized by the square of puff center axial velocity. Figure 5.21 shows the profiles of $<u'v'>/U_c^2$ versus r/d for different puff, and compares the puffs individually with the steady jet, while Fig. 5.22 presents $<u'v'>/U_c^2$ versus $r/r_{1/2}$ for different puffs. It was shown earlier for the steady jet that the turbulent shear stress is self similar in the studied range. The measured Reynolds shear stress for puffs is observed to follow a trend similar to the steady jets but is of much larger magnitude especially for the lowest P puff. The absolute maximum magnitude of $<u'v'>/U_c^2$ for puff with $P = 4$ increases by about 2.5 times the steady jet. The $(<u'v'>/U_c^2)_{max}$ for the puffs examined and the steady jet is shown in Table 5.8. The shear stress is asymmetric about the centerline: positive where the mean shear ($\partial U/\partial r$) is negative and negative where the mean shear is positive. The sign of the shear stress agrees with the net transport of high momentum away from the centerline.

Table 5.8: The peak value of normalized Reynolds shear stress.

P	$(\langle u'v' \rangle / U_c^2)_{max}$
4	0.064
5	0.049
6	0.041
8	0.029
Steady	0.025

The distribution profile of turbulent shear stress gets closer to steady jet profile as *P* increases. The puff with *P* = 8 is much closer to the steady jet than that of the other cases. The centerline value doesn't cross zero for puffs due to random motions of the puffs. It can be seen in both figures (Fig. 5.21 and Fig. 5.22) that *P* = 4 puff has the highest peak value of $\langle u'v' \rangle / U_c^2$ among the puffs.

5.2.4 Turbulent Kinetic Energy of Puffs

The turbulent kinetic energy, *TKE*, of the puff was computed from the averaged fluctuation velocities as follow:

$$TKE = 1/2(u'_{rms} + v'_{rms} + w'_{rms}) \quad (5.5)$$

where w'_{rms}, is azimuthal velocity fluctuation. It was assumed that the magnitude of azimuthal, w'_{rms}, is the same as the radial velocity fluctuation (v'_{rms}).

Figure 5.23 shows contours of kinetic energy of velocity fluctuations normalized by the square of the mean centerline velocity for the puffs and the steady jet. The puff center is denoted by a bold plus (+) symbol in the plots. The estimated experimental uncertainty of the turbulent kinetic energy ($\sqrt{(\Delta u'_{rms}\%^2 + \Delta v'_{rms}\%^2 + \Delta w'_{rms}\%^2)}$) is shown

in table 5.9. It should be mentioned that the *TKE* was normalized by the square of the puff center axial velocity, and for the steady jet, the *TKE* at each axial extent was normalized by the centerline axial velocity of the same axial location. These contour plots indicate that the peak turbulent kinetic energy for the puffs is near the centerline. In terms of kinetic energy magnitudes, the puff with $P = 4$ generates larger turbulent kinetic energy than either the puffs with higher P or the steady jet. In other words, the peak value decreases as P increases, and eventually gets closer to the steady jet for $P = 8$ puff.

Table 5.9: Uncertainty of puff turbulent kinetic energy.

P	Uncertainty % (TKE/U_c^2)
4	±3.48
5	±3.36
6	±3.52
8	±4.13

The region of high turbulent kinetic energy grows as P increases; however, the magnitude decreases. This is consistent with the fluctuating velocity profiles in the previous sections. As P increases, the region of high turbulent kinetic energy is located towards the leading edge of the puff. The kinetic energy maps show elongated contours in the downstream direction for higher P puffs, which reflect the lateral diffusion associated with the longitudinal convection. The steady jet turbulent kinetic energy contour indicates the growth of a turbulent region with increasing z.

5.2.5 Vorticity Fields of Puffs

By calculating the vorticity fields from the velocity field ($\omega = \nabla \times \vec{V}$), it is possible to follow the motion of coherent structures. The averaged azimuthal vorticity field, ω_θ, of the puff was computed from the averaged velocity field as follow:

$$\omega_\theta = \frac{\partial V}{\partial z} - \frac{\partial U}{\partial r} \tag{5.6}$$

The normalized mean vorticity contours, $\omega_\theta d/U_c$, for puffs with P = 4, 5, 6 and 8 and the steady jet are shown in Fig. 5.24. The vorticity for the puffs has been normalized by puff center axial velocity over nozzle diameter (U_c/d), and for the steady jet at each axial location was normalized by the centerline velocity at the corresponding axial location over d. The flow direction is from the bottom to the top. The puff center is shown by a bold plus (+) symbol in the plots. The estimated experimental uncertainty of the vorticity ($\sqrt{(\Delta\omega'_{rms}\%^2 + \Delta U_c\%^2 + \Delta d\%^2)}$) is shown in table 5.10.

Table 5. 10: Uncertainty of the puff vorticity.

P	Uncertainty% ($\omega d/U_c$)
4	±4.55
5	±4.47
6	±4.54
8	±4.95

Averaging the data, $\overline{(\nabla \times \vec{V})}$, makes small scale eddies vanish. These measurements illustrate the presence of a vortex ring, which develops and moves downstream. The mean flow essentially results from the self-induced motion of the vortex ring, in which controls the whole flow dynamics. The puff structure consists of a ring vortex, which the

maximum and minimum values are located at the center of the cores. There is no vorticity observed at the puff centerline. The magnitude of the normalized vorticity doesn't change much as P increases. This indicates the normalized vorticity magnitude is less dependent on P than the turbulent fluctuation velocities. These contour plots indicate that the structure become more elongated as P increases.

Figure 5.25 shows normalized vorticity, $\omega_\theta d/U_c$, versus r/d for different puffs at the puff center, and compares the puffs individually with the steady jet. It is to be noted that for the steady jet, the vorticity at each axial extent was normalized by the centerline axial velocity of the same axial location over the nozzle diameter, while for the puffs, it was normalized by the puff center axial velocity over nozzle diameter. The $\omega_\theta\, d/Uc$ profile for puffs is observed to follow a trend similar to the steady jets. The puff with P = 8 is much closer to the steady jet than the other cases. The centerline value does not cross zero for puffs due to random motions of the puffs.

The root-mean-square of vorticity is obtained as follow:

$$\omega'_{rms} = \sqrt{\frac{\sum_{i=1}^{n} (\omega - \overline{\omega})^2}{n}} \tag{5.7}$$

Figure 5.26 shows the root-mean-square values of mean vorticity contours normalized by the centerline velocity over nozzle diameter, ($\omega'_{rms}\, d/U_c$), for the puffs and the steady jet. The estimated experimental uncertainty of the vorticity rms is shown in table 5.11.

The maximum ω'_{rms} occurs nearly around the center of puff. For the puffs with P = 4, 5, and 6, the profiles exhibit some similarity. For P = 8 puff the peak occurs at the trailing edge of the flow field. The steady jet contour of ω'_{rms} indicates the growth of

ω'_{rms} region with increasing z. The steady jet peak value of ω'_{rms} occurs at the trailing edge of the flow field along the centerline of the jet.

Table 5. 11: Uncertainty of the puff vorticity rms.

P	Uncertainty % ($\omega_{rms}d/U_c$)
4	±6.19
5	±6.21
6	±6.25
8	±6.33

5.2.6 Entrainment

Entrainment is quantitatively defined as the radial inflow of ambient fluid into the turbulent region. The rate of entrainment controls the mixing rate of the injected flow with the ambient fluid. Entrainment in equilibrium turbulent flows is related to the Reynolds shear stress (Bremhorst & Hollis, 1990). Results of the preceding sections have shown that the puffs have a higher Reynolds shear stress than that of the steady jet at the same Reynolds number. Therefore, the entrainment of a puff is expected to be greater than that of the steady jet.

One method for calculating entrainment in jets involves analyzing the inward radial flow of entrained fluid into the jet through a cylindrical control surface of radius *r*. Volume flow rate, Q, in the axial direction at any location for the axisymmetric flow is defined by:

$$Q = \int_0^{\infty}\int_0^{2\pi} U dr r d\theta = \int_0^{\infty} 2\pi r U dr \tag{5.8}$$

Since the axial velocity can be written as $U = U_o \frac{d}{z - z_o} \exp[-k_u (r / r_{1/2})^2]$, then the integration provides

$$Q = U_o \frac{\pi d}{(z - z_o) k_u} r_{1/2}^2(z) \tag{5.9}$$

Then the entrainment rate will be as follows since $r \sim z$.

$$\frac{dQ}{dz} = C_e \frac{Q_o}{d} \tag{5.10}$$

where C_e is entrainment constant, and Q_o is the injected volume flow rate. For the steady jet, the entrainment rate grows from a low value at the nozzle exit to $C_e = 0.32$ in far field (Gharib *et al.*, 1998; Han & Mungal, 2001; Falcone & Cataldo, 2003). The local C_e varies with many parameters such as heat release, buoyancy, co-flow speed, and axial position, but in the far field of homogenous jets is a constant.

Since the Gaussian velocity distribution at the puff centers were in excellent agreement with the measurements, the analytical expression $U = U_c \exp[-k_u ((r-r_o)/r_{1/2})^2]$ was used to compute the volume flow rate. Replacing the Gaussian distribution of (Eq. 5.4) into Eq. 5.8, we obtain:

$$Q = \frac{\pi}{k_u} U_c(z) r_{1/2}^2(z) \tag{5.11}$$

The estimated experimental uncertainty of the Q/Q_0 is shown in table 5.12.

Table 5.12: Uncertainty of the puff volume flow rate.

P	Uncertainty % (Q/Q_o)
4	±3.79
5	±3.83
6	±3.99
8	±4.41

Figure 5.27 shows the volume flow rate normalized with initial injected volume flow rate (Q_o) of steady jet, Q/Q_o, versus *z/d* for puffs at puff center and the steady jet. This plot shows much larger volume flow for the puffs than for the steady jet, except for $P = 8$ puff. The trend for steady jet is quite linear except at the larger *z/d* values (Eq. 5.9). The linear fit to the steady jet data is shown by a solid line in Fig. 5.27. This illustrates that the volume flux of the steady jet increases with increasing distance from the jet exit as expected (Han & Mungal, 2001; Falcone & Cataldo, 2003). The puff with $P = 4$ has the highest volume flow rate at the puff center. As P increases, the Q/Q_o decreases. The value of Q/Q_o for the $P = 4$ puff is about 2.4 times the steady jet value at the $P = 4$ puff center. The Q_{puff}/Q_o, and $Q_{steady\ jet}/Q_o$ for the examined puffs and the steady jet are shown in Table 5.13.

Table 5.13: Volume flow rate ratio of puff to the initial injected steady jet volume flux.

P	***(z/d)c***	Q_{puff}/Q_o	$Q_{steady\ jet}/Q_o$
4	59.7	44	18.40
5	65.7	32	20.30
6	62.7	30	19.37
8	46	16	14.21

The entrainment coefficient, C_e, for the steady jet can be obtained from Fig. 5.27 using Eq. 5.9. The entrainment coefficient of previous studies for non-reacting free jet approaches $C_e = 0.32$, while the present steady jet converges to the value $C_e = 0.3$ (Han & Mungal, 2001; Agrawal & Parsad, 2003; Falcone & Cataldo, 2003). Our steady jet value for C_e is smaller than the free steady jet value reported previously, because the present experiments took place in a weak co-flow. Han & Mungal (2001) showed that the entrainment coefficient of jet reduces as the co-flow speed increases. This is due to the

fact that the behavior of jets in co-flow is known to show a jet like behavior in near field and wake-like behavior in the far field (Han & Mungal, 2001). For a fully developed self-similar non-reacting flow, the entrainment rate defined by Eq. 5.11 is a constant. However, for a fully developed wake with a small excess velocity, the entrainment is achieved by the encroachment of the boundary on the surrounding fluid and should decrease associated with self-similarity.

The ratio of volume flow rate of puff to the steady jet volume flow rate, $Q_{puff}/Q_{\text{steady}}$, is shown in Figure 5.28. It should be mentioned that the Q_{steady} corresponds to the location of each puff center. This plot illustrates the volume flow rate of the puff is greater than that of the steady jet at puff center for the same Reynolds number. Moreover, the increase in entrainment resulted in a larger Q for the puffs in comparison with the steady jet. Therefore, puffs with smaller P mix more rapidly than those with a larger P.

The entrainment rate at large r can be defined as (Liepmann & Gharib, 1992; Han & Mungal, 2001; Falcone & Cataldo, 2003):

$$\frac{dQ}{dz} = \lim_{r\to\infty}(-2\pi rV) \tag{5.12}$$

In our measurement, the result of $2\pi rV$ for the puff and the steady jet is shown in Fig. 5.29. The estimated experimental uncertainty of the $2\pi rV$ is shown in table 5.14.

Table 5. 14: Uncertainty of the entrainment rate.

P	Uncertainty % ($2\pi rV$)
4	±3.56
5	±2.81
6	±4.19
8	±3.92

Figure 5.29 shows the value of $2\pi rV$ as a function of $r/r_{1/2}$ at different axial location for the right half of the puff flow field, and compares the puffs individually with the steady jet. The circled line denotes data at the puff center. The $2\pi rV$ in these plots has two signs, positive and negative. The negative sign is for $z/d < (z/d)_{center}$ which shows the existence of inflow of surrounding flow into the puff below the puff center. For axial location beyond the puff center, the parameter $2\pi rV$ has a positive value which indicates fluid is being pushed out the puff. The data shows that the majority of entrainment into the puff occurs from below the puff center while the puff cap pushes out into the surrounding fluid. The data in the left half of the puff show a similar pattern.

Figure 5.30 illustrates the measured $2\pi rV$ for puffs with P = 4, 5, 6, and 8 and the steady jet versus normalized radial position ($r/r_{1/2}$) at the puff center. This plot shows that at the puff center, no entrainment takes place. The steady jet entrains from the sides, whereas the puff does not entrain at the puff center except the P = 8 case.

In the current work, it was initially tried to calculate the entrainment by defining the volume of the puff. The primary difficulty of this measurement was associated with the puff boundary. For this purpose, the instantaneous streamline of the puff flow obtained from the velocity field was needed. Figure 5.31a shows the instantaneous streamlines of puff with P = 4, in a laboratory reference frame. In order to be able to see the physical extent of the puff, the measurement needs to be taken in a frame moving with the puff. This could be accomplished by subtracting the puff celerity from the measured axial velocity. The celerity of the puff was measured from the axial location of peak vorticity in the cores. In this study, phase locked measurements at two different times for each puff had been done. Figure 5.31b shows the same puff (P = 4) in its moving frame. The

shape of the streamlines is very sensitive to the celerity value. In order to computing the puff volume, a closed streamline is required. In the present study, no closed streamline could be found, presumably due to the lack of perfect symmetry and the precise value of celerity. This method requires a very accurate measurement of the puff trajectory in order to compute the puff celerity (velocity of the puff center). This is the method that Dabiri & Gharib (2004) used for calculating the entrainment of isolated, laminar vortex rings.

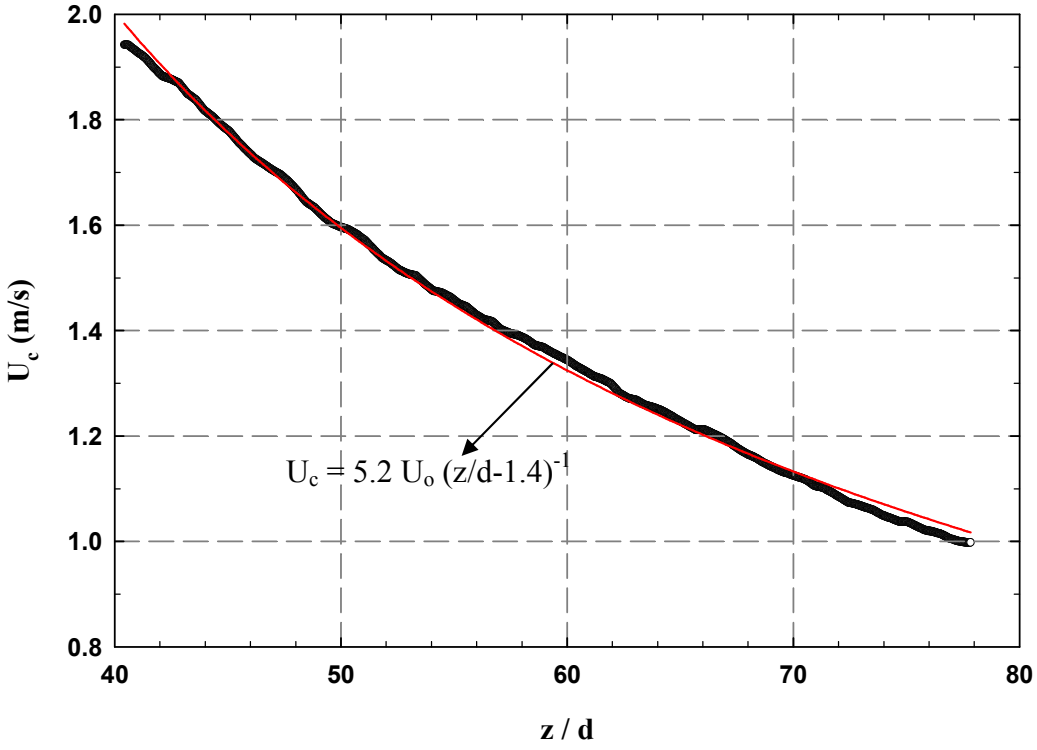

Figure 5.1: Variation of centerline velocity along the steady jet axis.

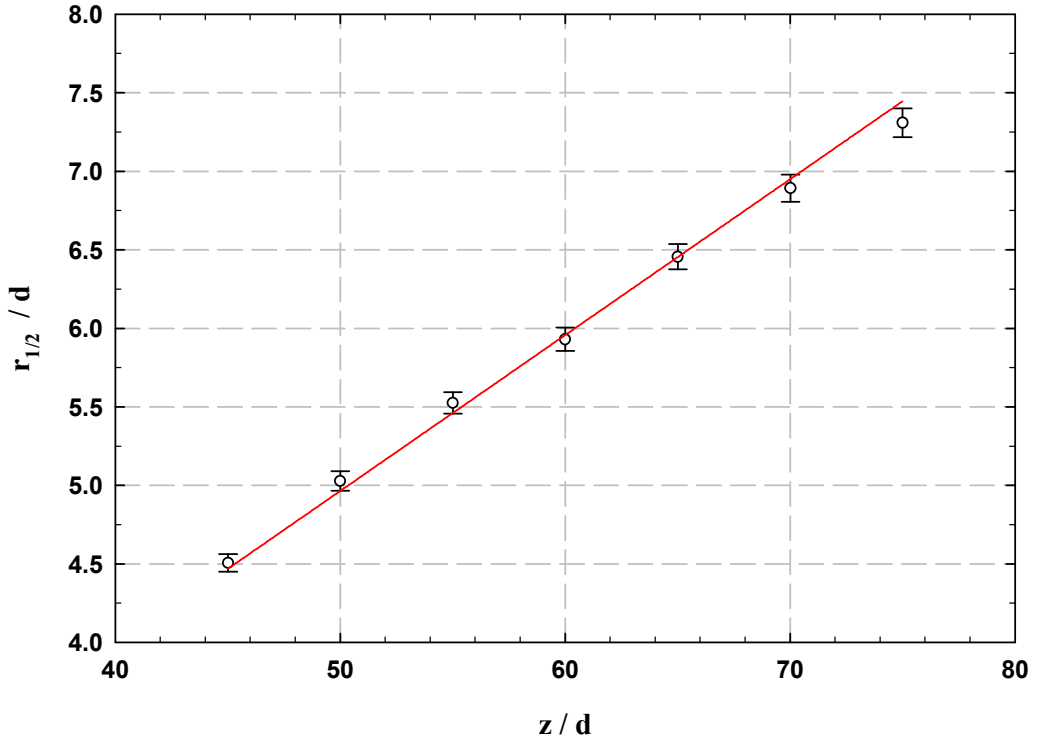

Figure 5.2: Development of the half-width for the velocity field of steady jet. Solid curve represent the linear fit to the data.

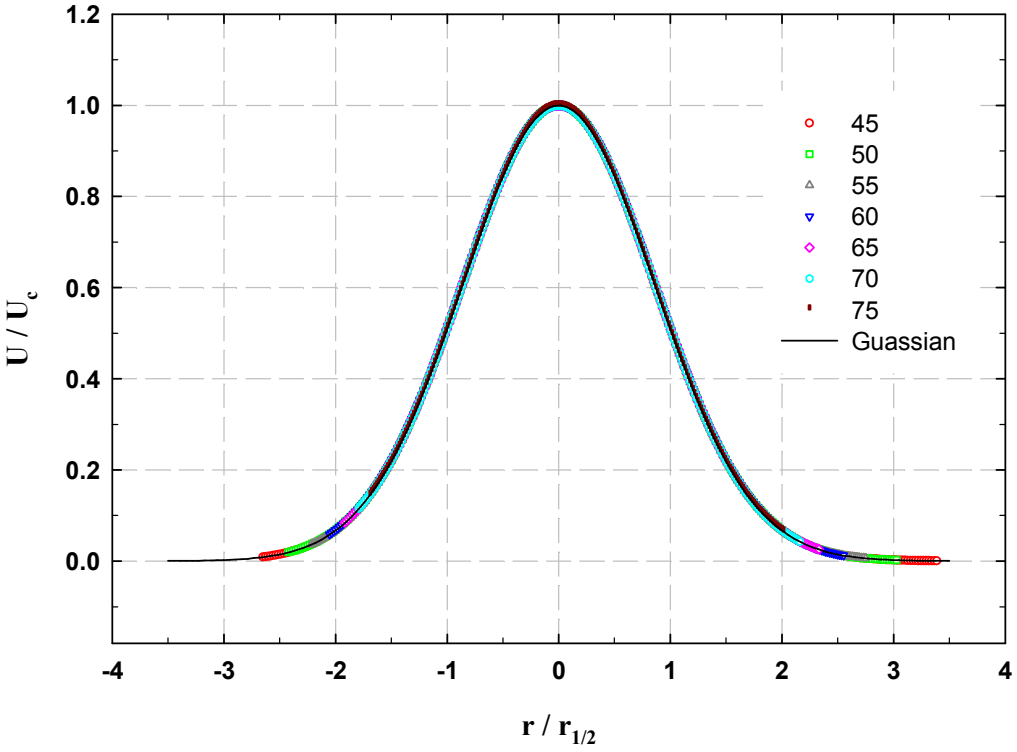

Figure 5.3: Axial velocity profile across the steady jet in a self-similar format.

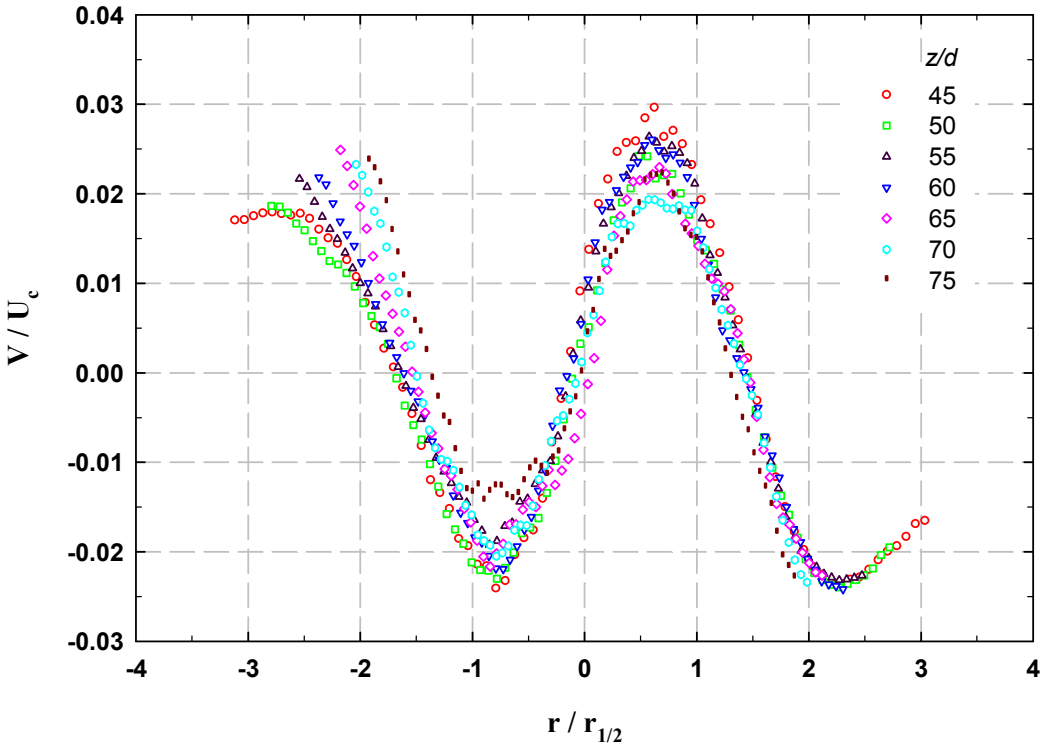

Figure 5.4: Radial velocity profile across the steady jet.

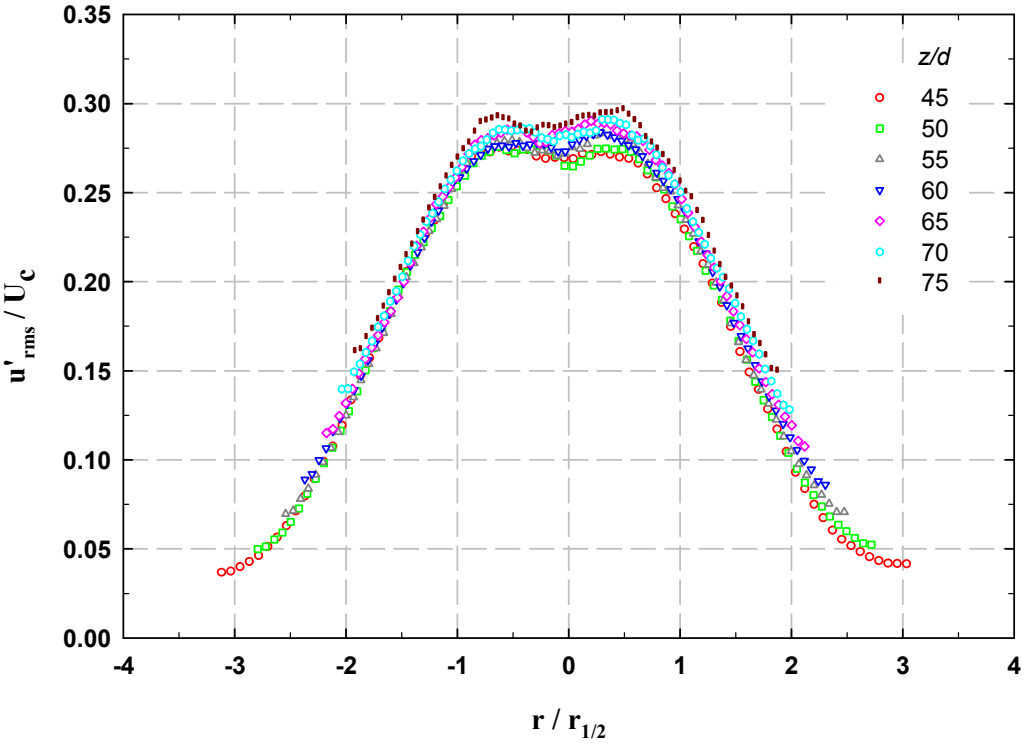

Figure 5.5: Radial velocity fluctuation profile across the steady jet.

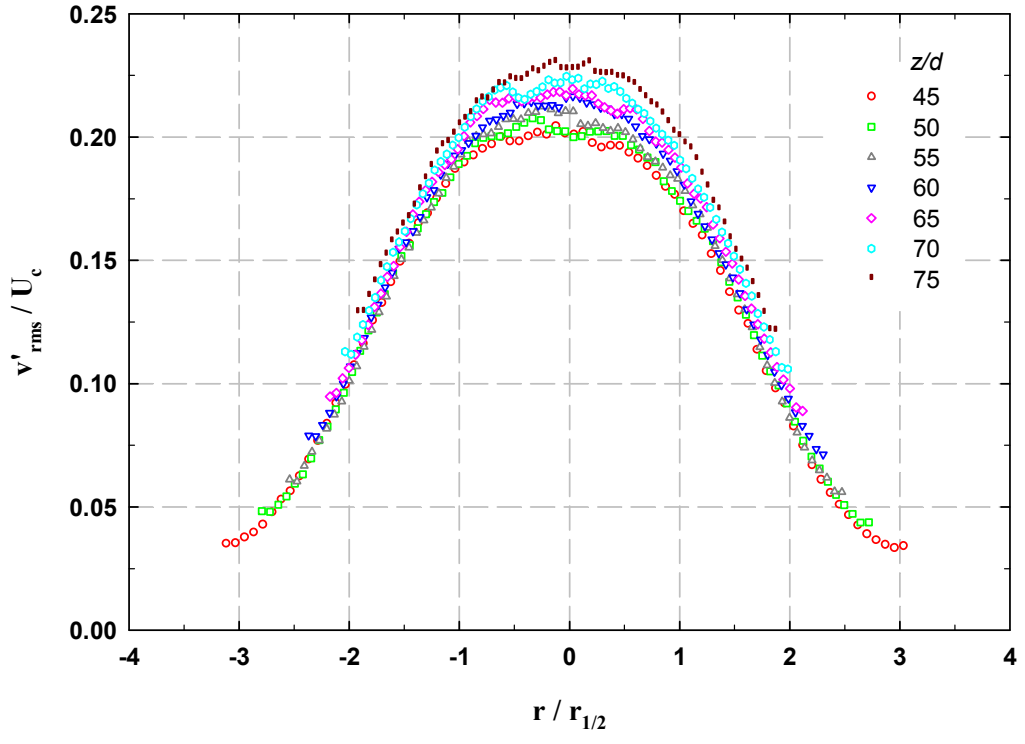

Figure 5.6: Axial velocity fluctuation profile across the steady jet.

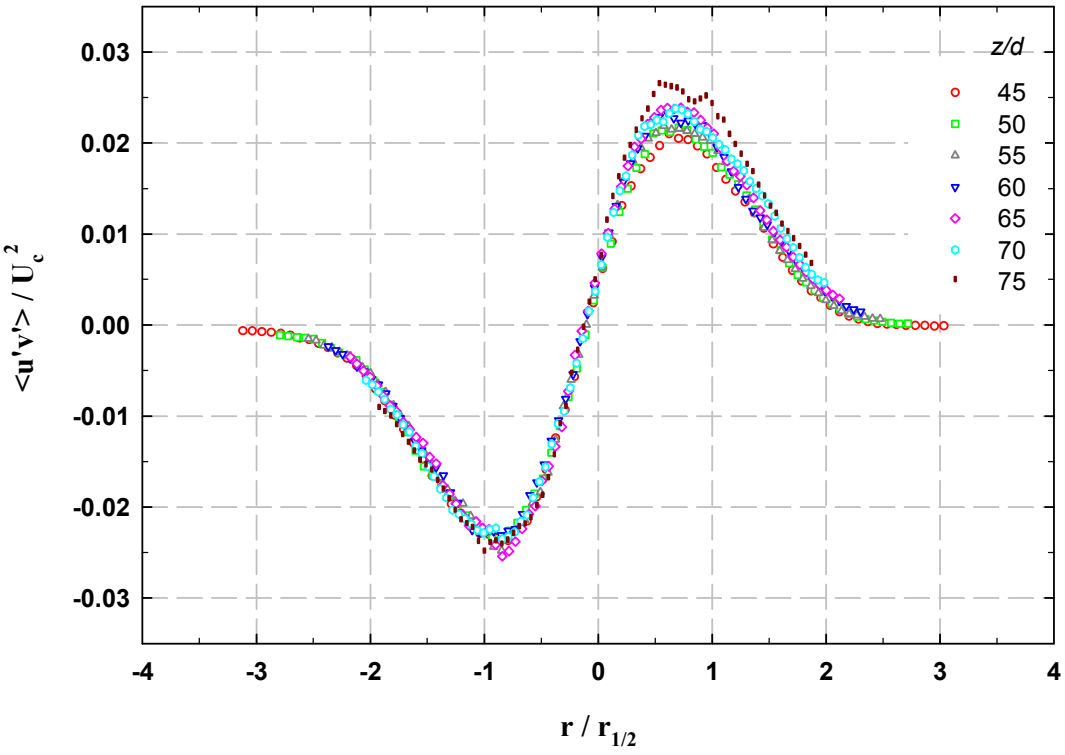

Figure 5.7: Turbulent shear stress profile across the steady jet.

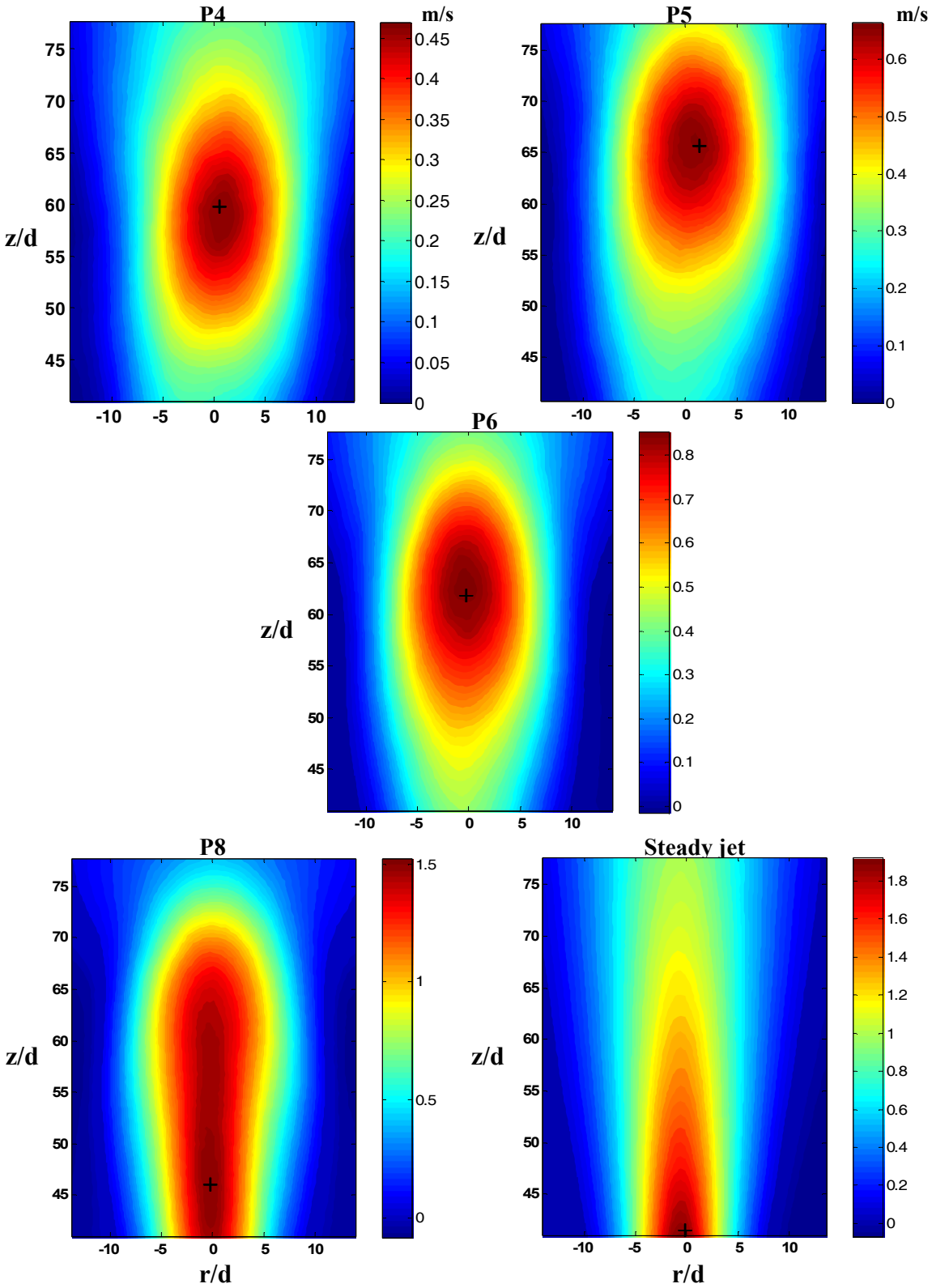

Figure 5.8: Axial velocity profile for the puff, and the steady jet. The unit is m/s, and the flow direction is from the bottom to the top. The bold plus denotes the location of puff center.

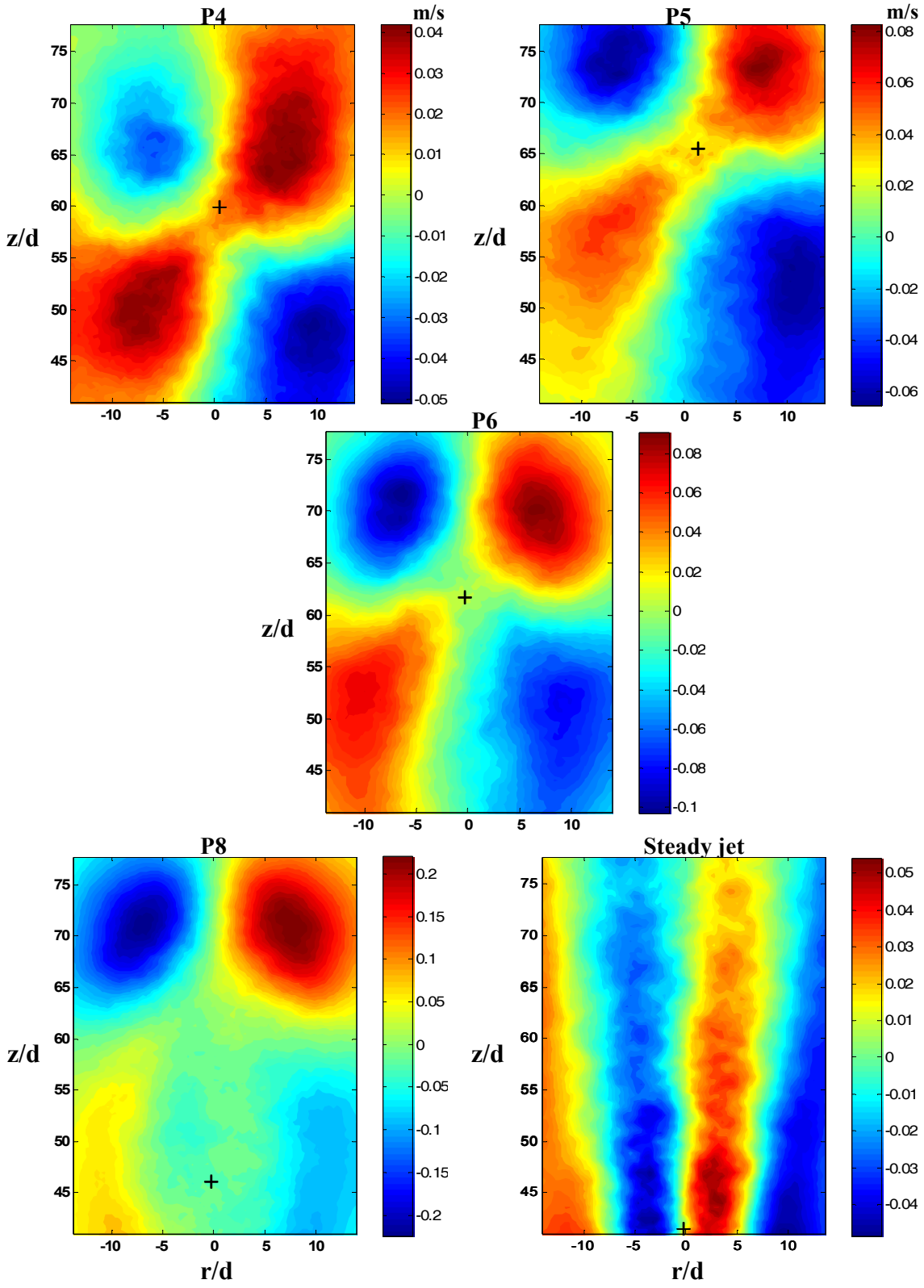

Figure 5.9: Radial velocity profile for the puff, and the steady jet. The unit is m/s, and the flow direction is from the bottom to the top. The bold plus denotes the location of puff center.

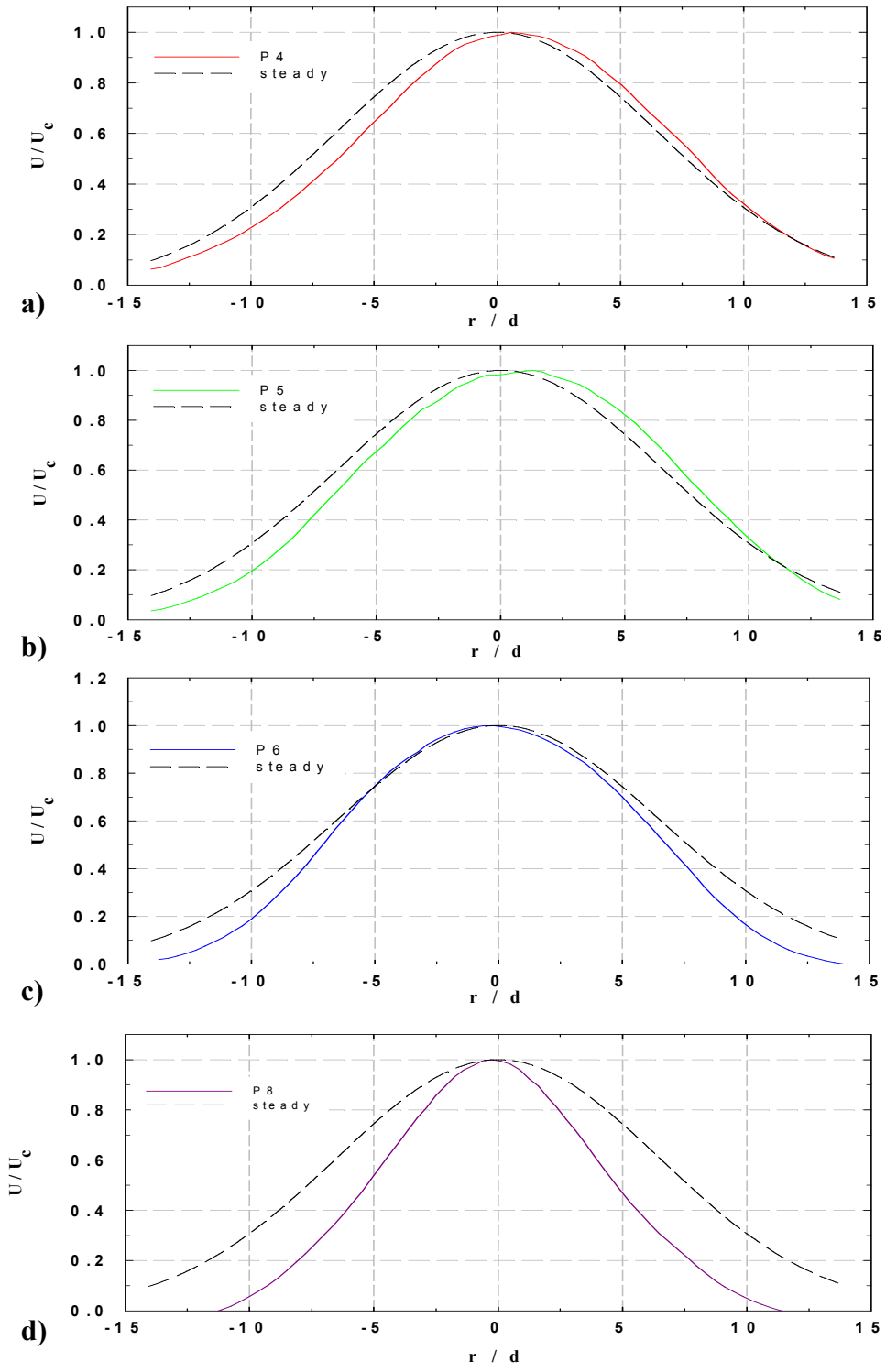

Figure 5.10: Normalized axial velocity profiles at puff center for the puff and the steady jet. a) *P*=4; b) *P*=5; c)*P*=6, and d) *P*=8. Dashed lines denotes for the steady jet at the same axial location as the puff center.

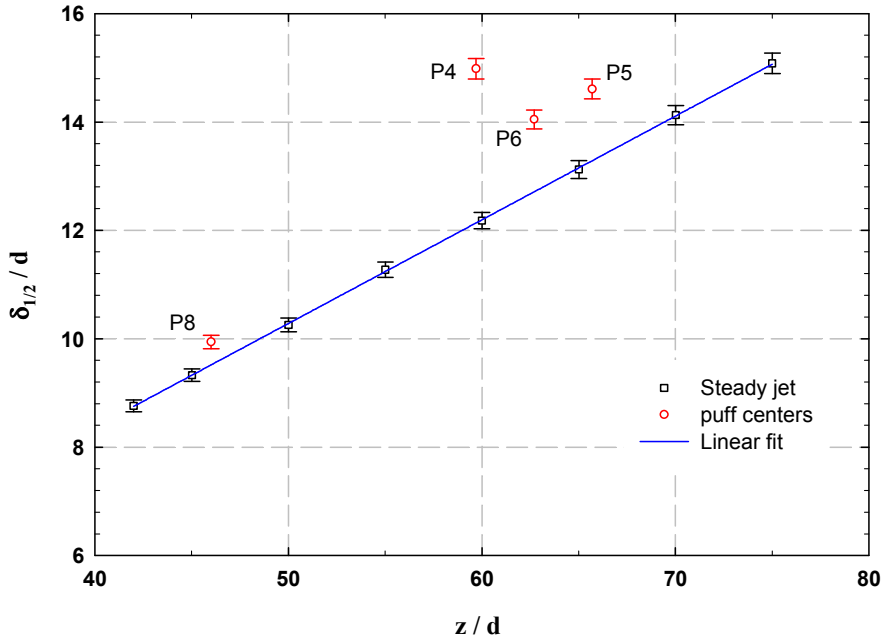

Figure 5.11: Normalized puff half-width as a function of *z/d*.

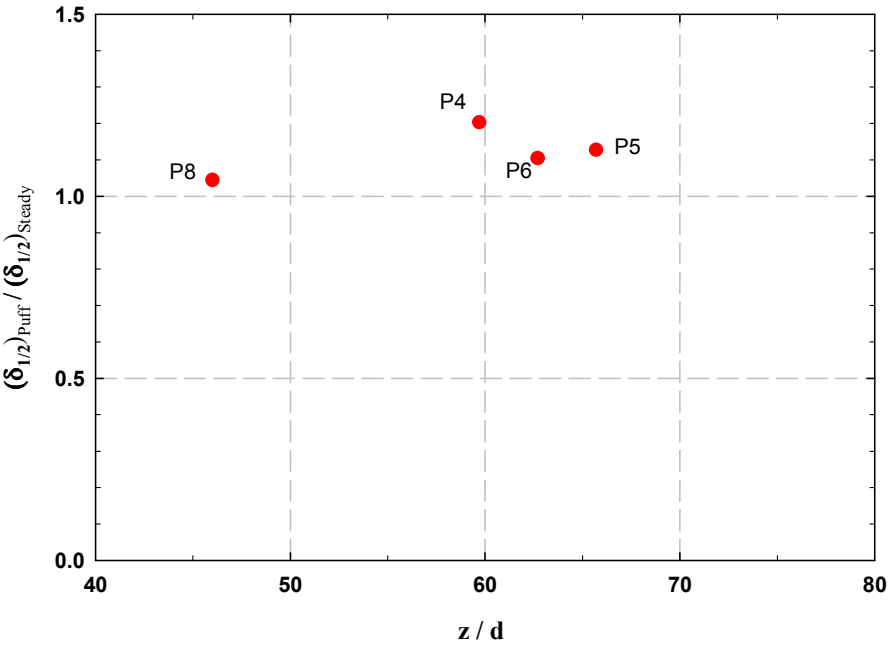

Figure 5.12: The ratio of the puff half-width to steady jet at puff center.

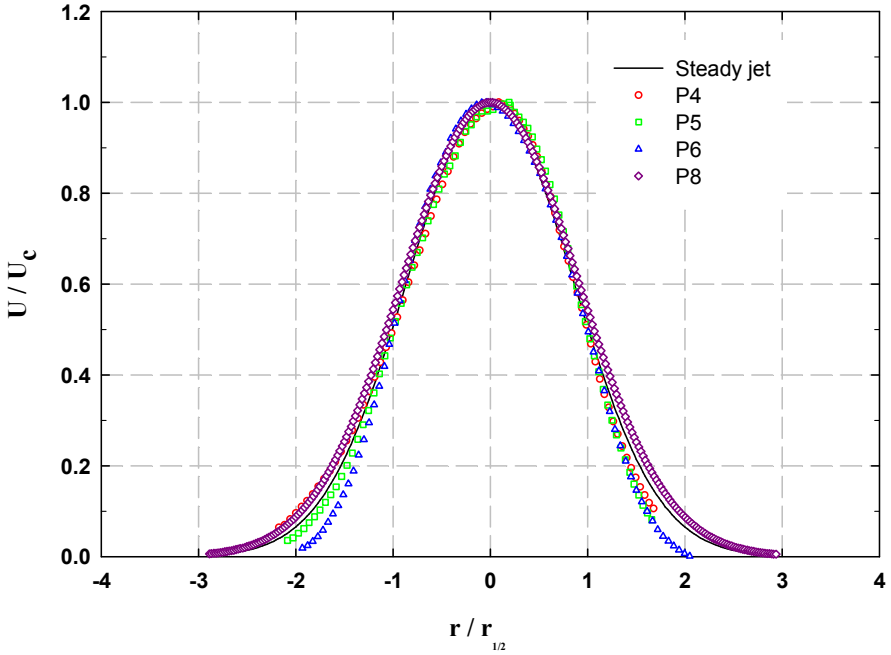

Figure 5.13: Normalized axial velocity profile across the puffs. Puff data corresponding to the location of puff center. The steady jet data are from Fig. 5.3.

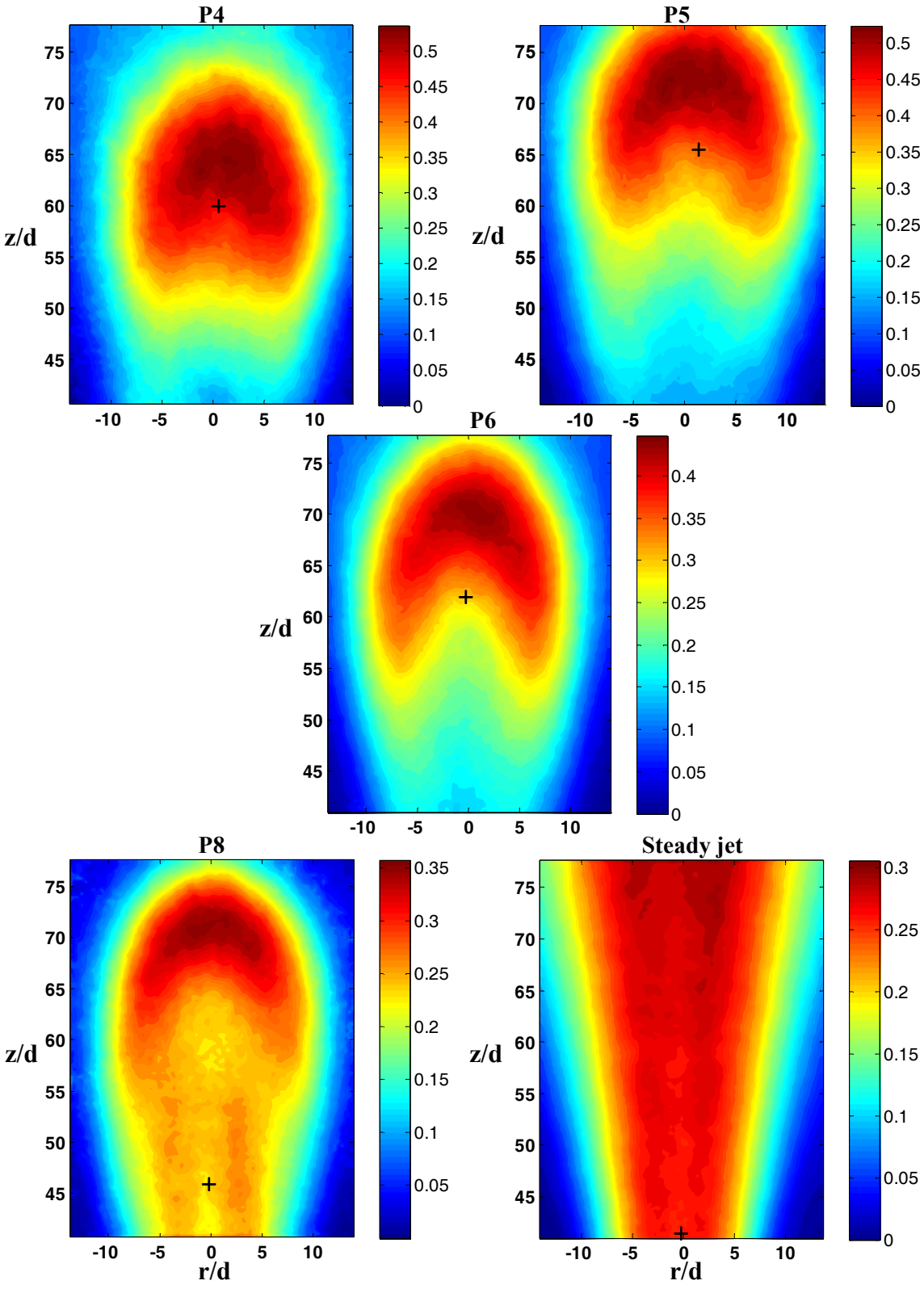

Figure 5.14: Normalized axial fluctuation velocity contours for the puff and the steady jet. The flow direction is from the bottom to the top. The bold plus denotes the location of puff center.

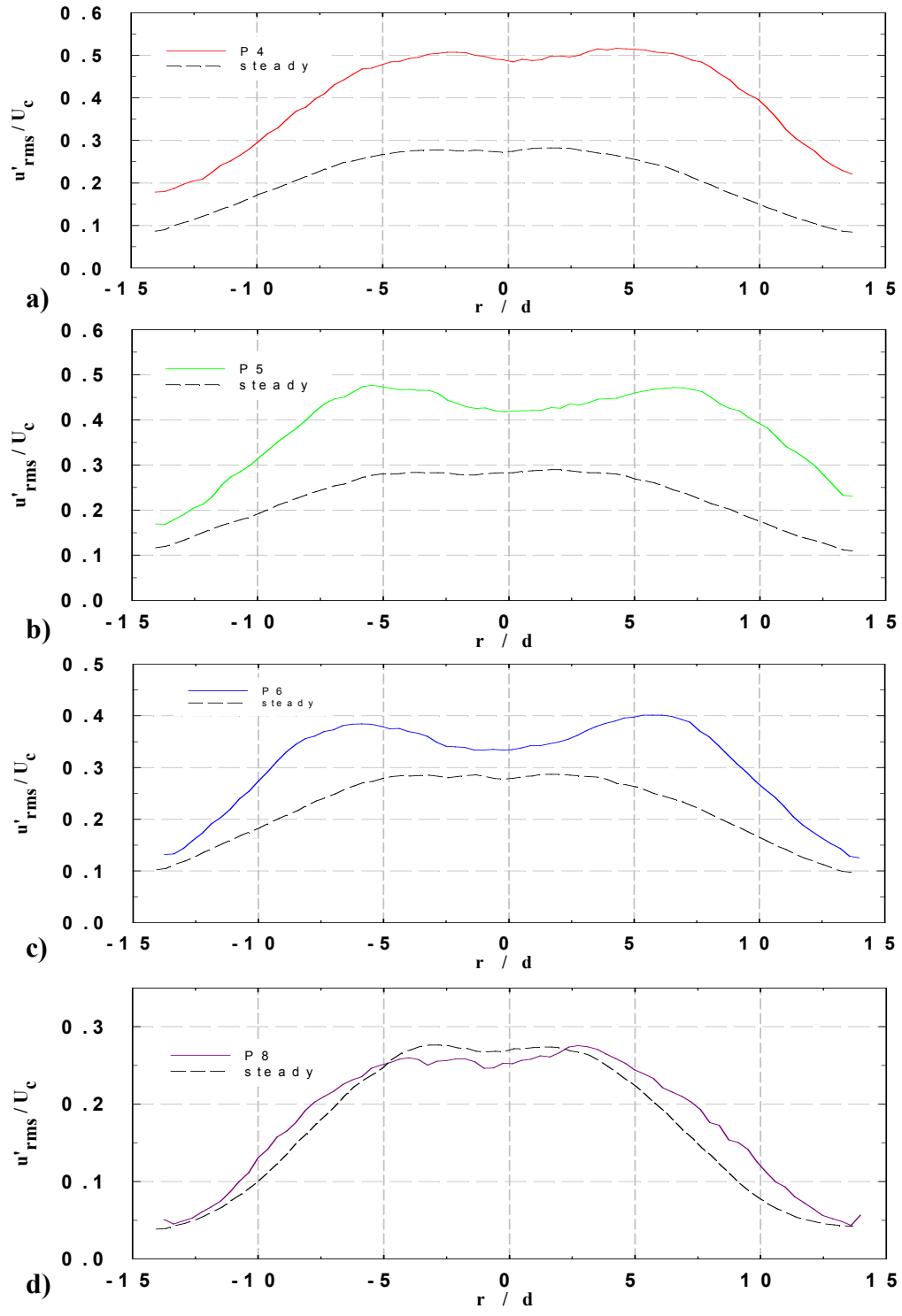

Figure 5.15: Normalized axial fluctuation velocity profiles at puff center for the puff and the steady jet. a) *P*=4; b) *P*=5; c)*P*=6, and d) *P*=8. Dashed line denote for the steady jet at the same axial location as the puff center.

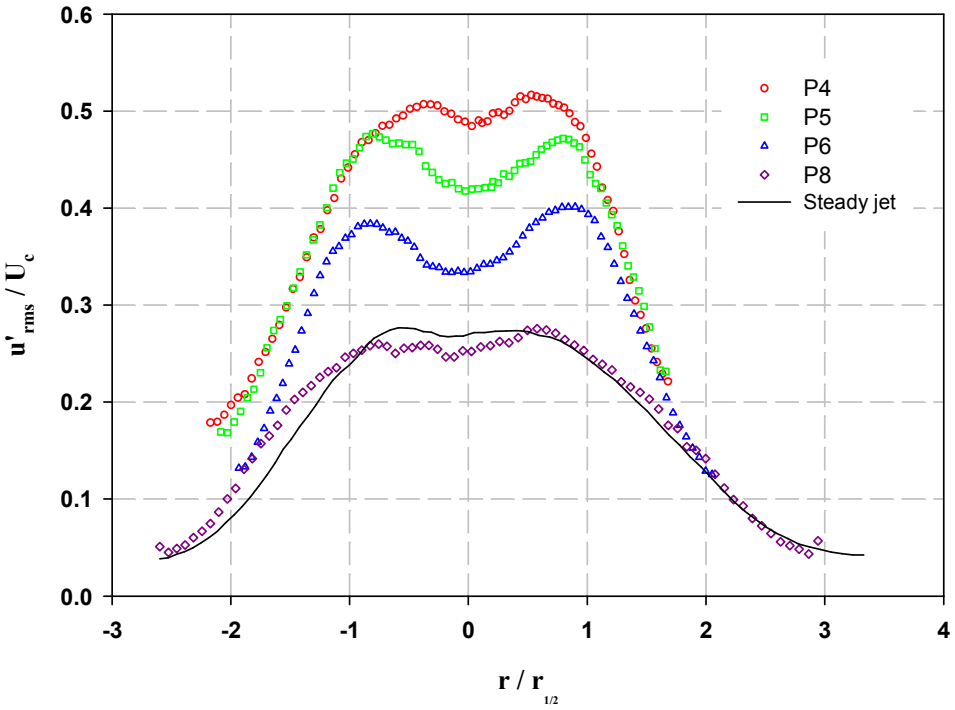

Figure 5.16: Normalized axial fluctuation velocity profiles for puff with $P = 4, 5, 6, 8$ and the steady jet.

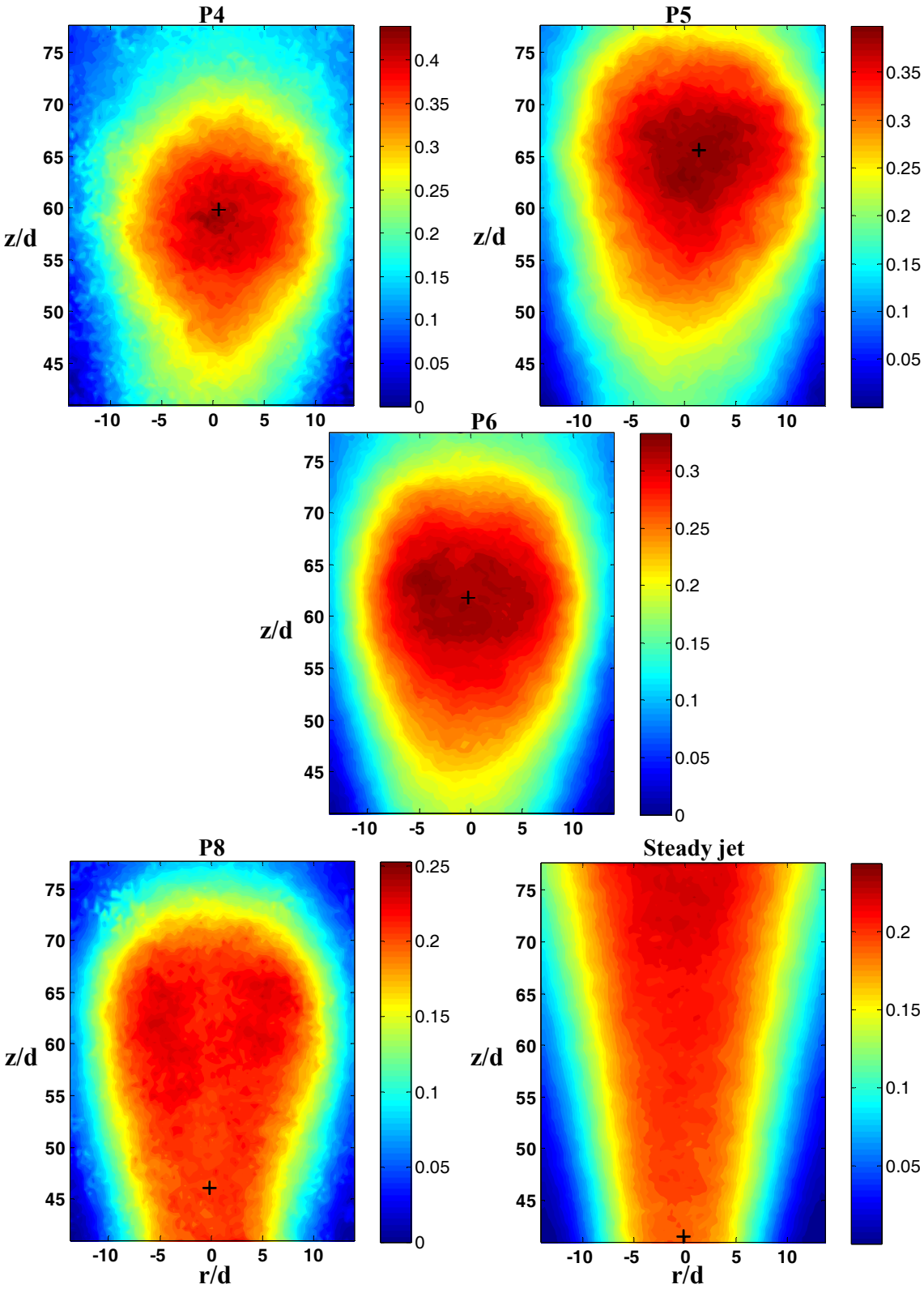

Figure 5.17: Normalized radial fluctuation velocity contours for the puff and the steady jet. The flow direction is from bottom to top. The bold plus denotes the location of puff center.

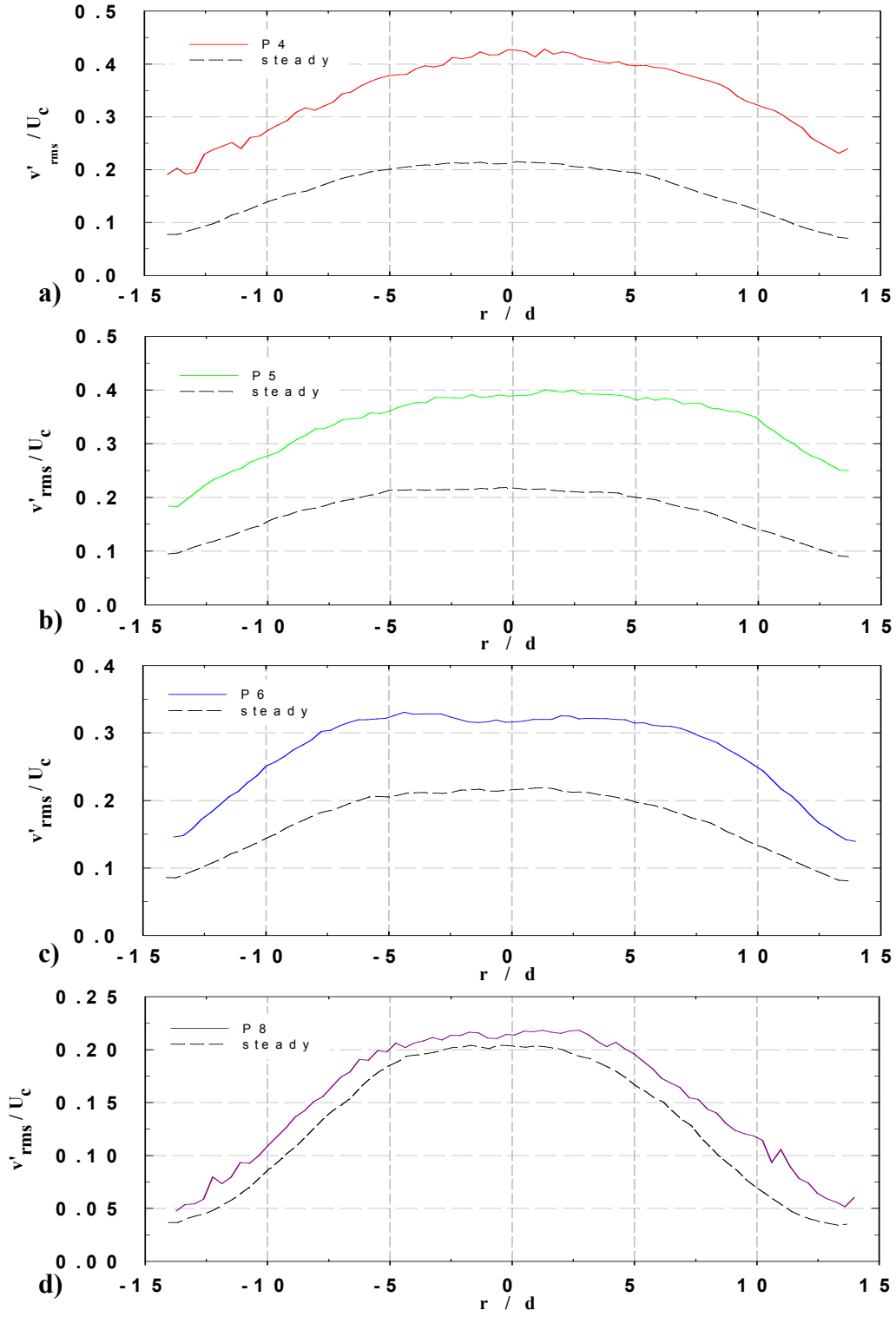

Figure 5.18: Normalized radial fluctuation velocity profiles at puff center for the puff and the steady jet. a) *P*=4; b) *P*=5; c)*P*=6, and d) *P*=8. Dashed lines denote for the steady jet at the same axial location as the puff center.

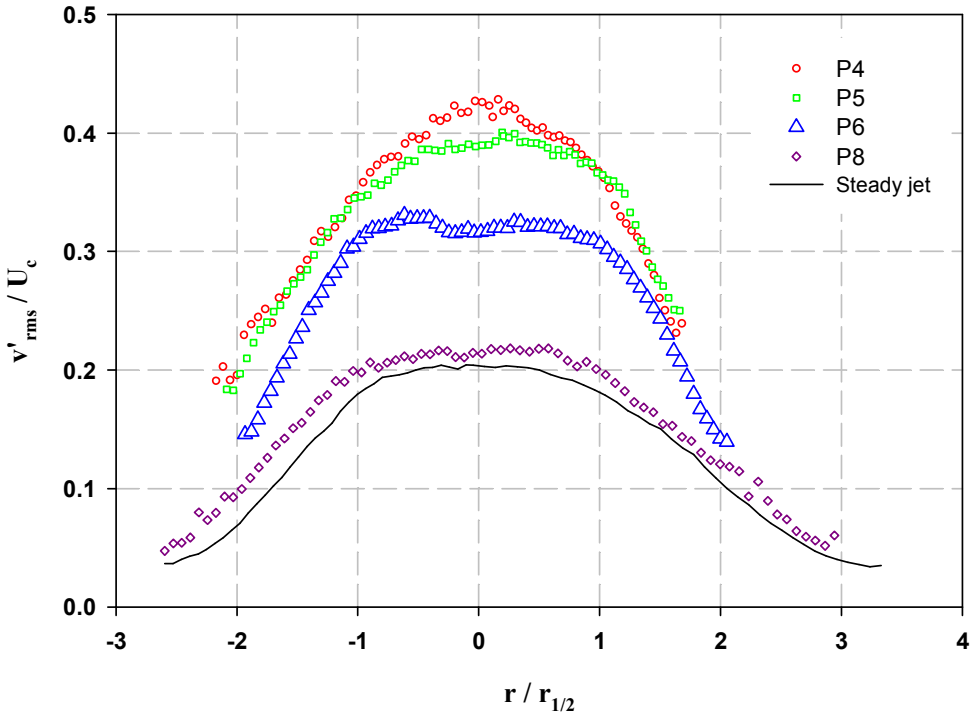

Figure 5.19: Normalized radial fluctuation velocity profiles for puff with P = 4, 5, 6, 8 and the steady jet.

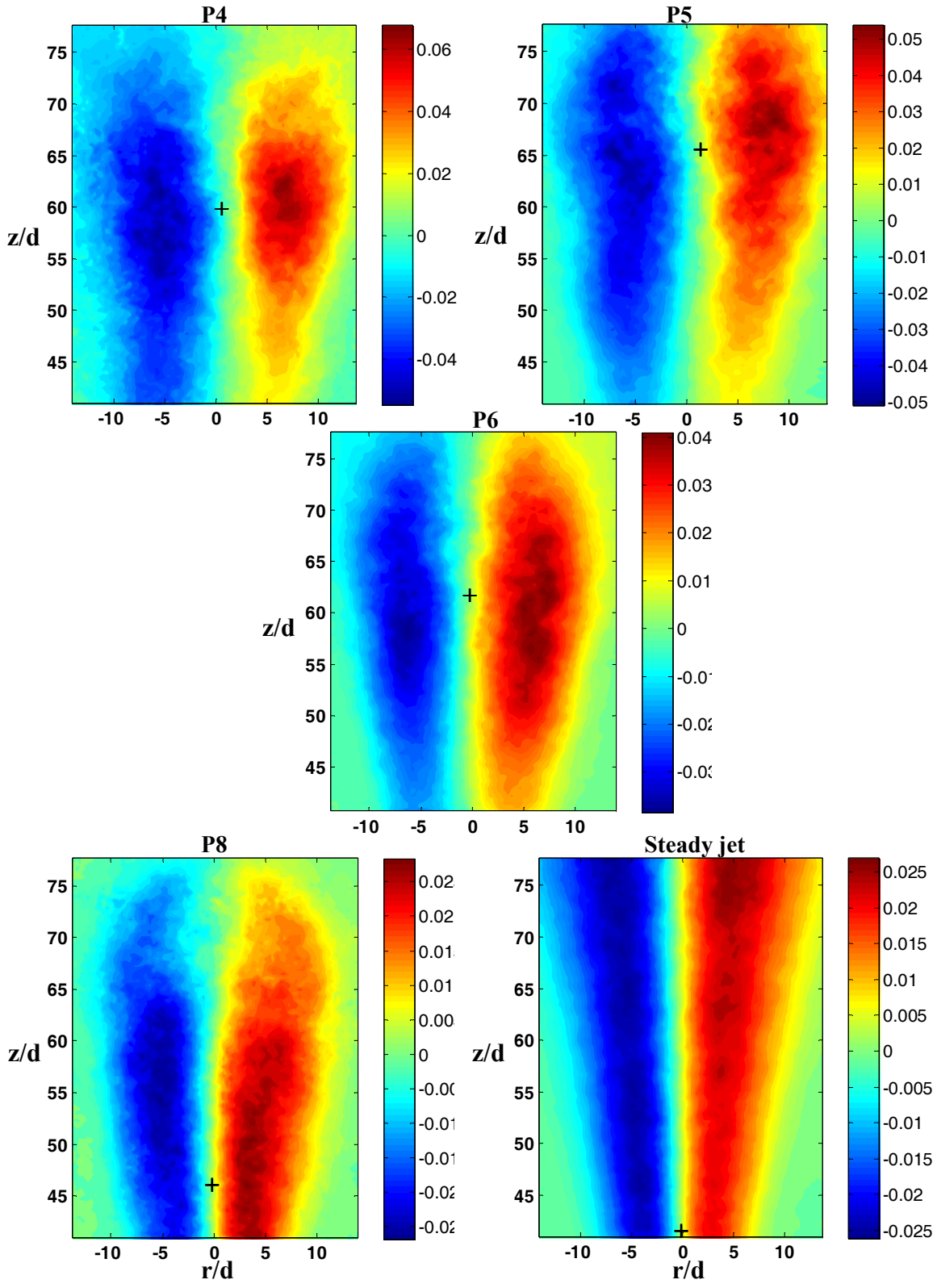

Figure 5.20: Normalized turbulent shear stress contour for the puff and the steady jet. The flow direction is from the bottom to the top. The bold plus denotes the location of puff center.

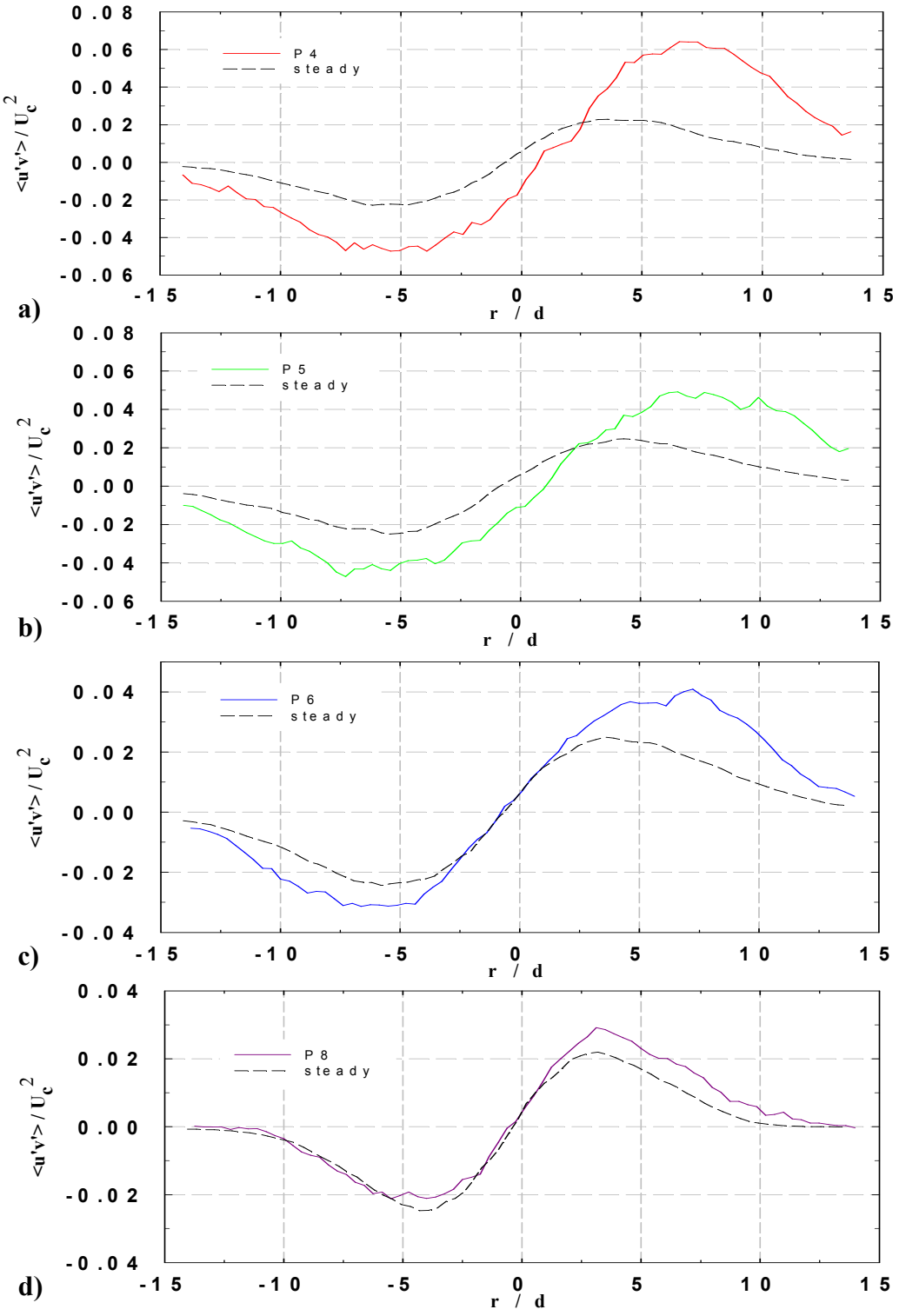

Figure 5.21: Normalized turbulent shear stress profiles at puff center for the puff and the steady jet a) *P*=4; b) *P*=5; c)*P*=6, and d) *P*=8. Dashed lines denote for the steady jet at the same axial location as the puff center.

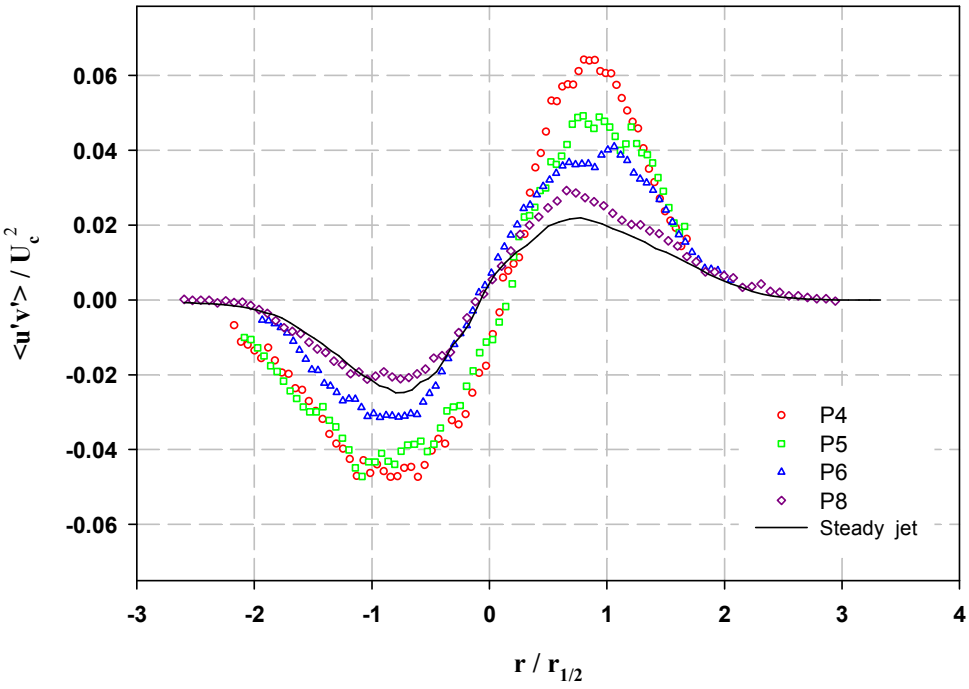

Figure 5.22: Normalized turbulent shear stress profiles for puff with P = 4,5,6, 8 and the steady jet.

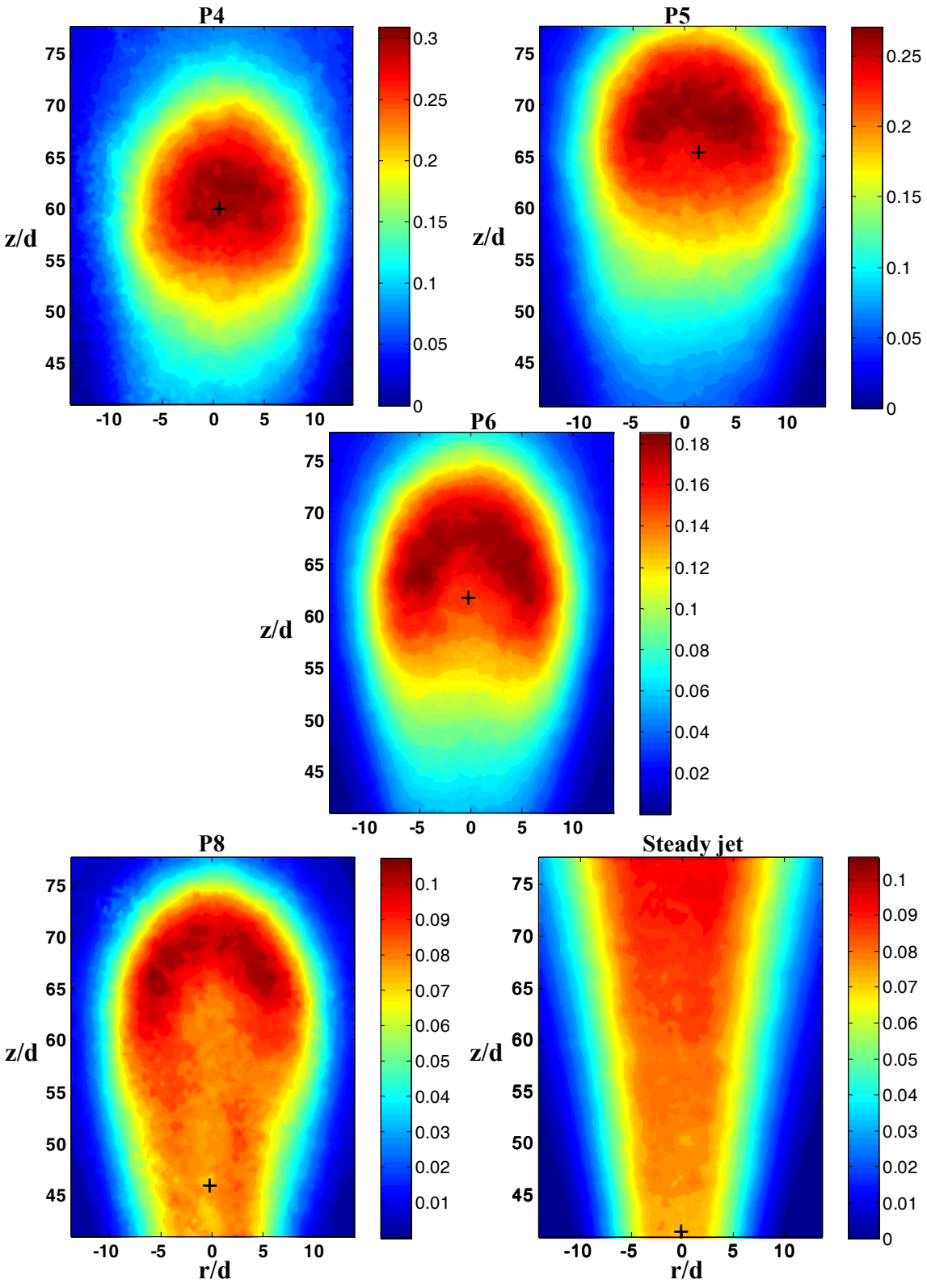

Figure 5.23: Normalized turbulent kinetic energy contour of the puffs and the steady jet. The flow direction is from the bottom to the top. The bold plus denote the location of puff center.

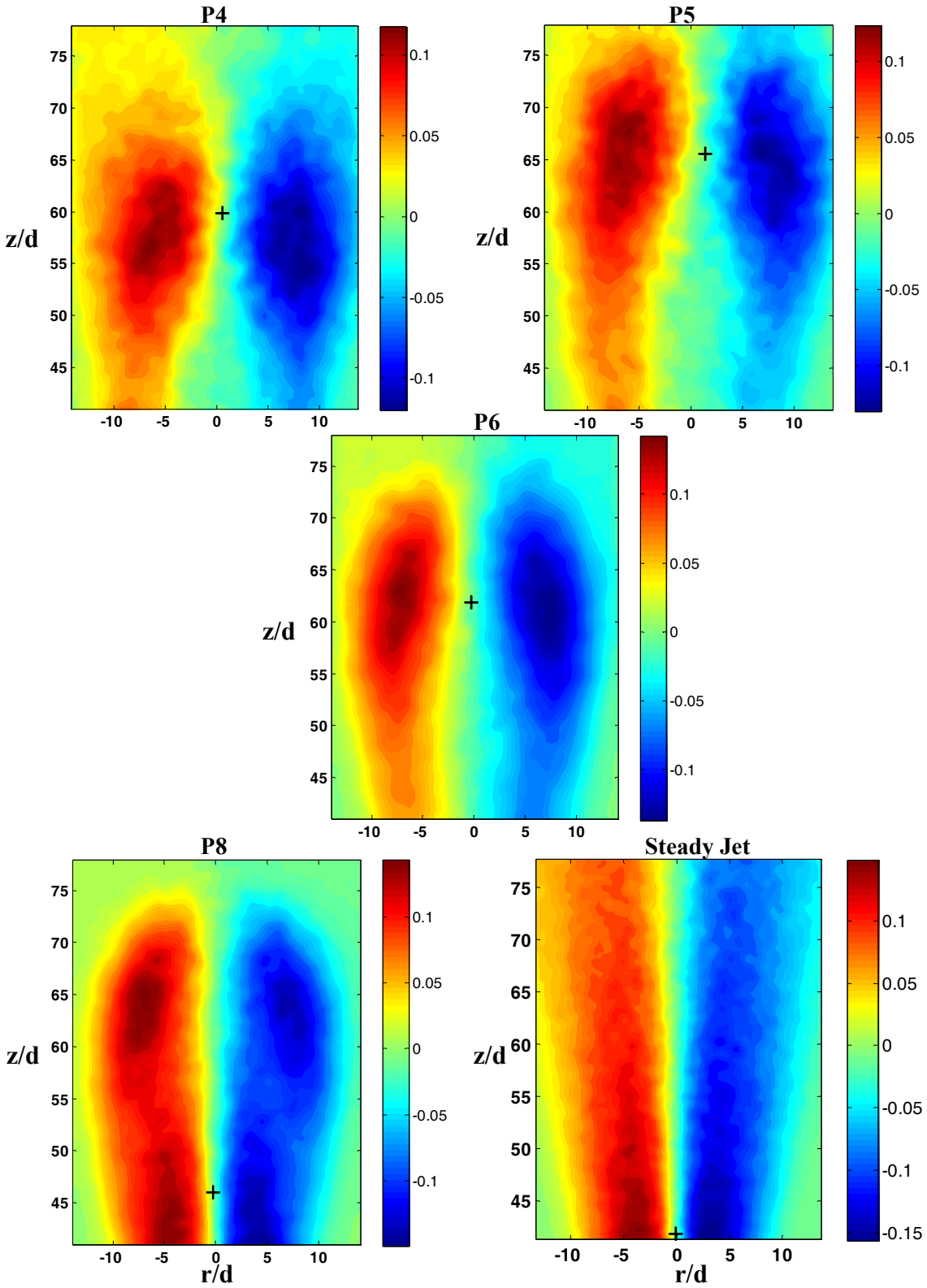

Figure 5.24: Normalized vorticity contour ($\omega_\theta d/U_c$) for the puff and the steady jet. The flow direction is from the bottom to the top. The bold plus denote the location of puff center.

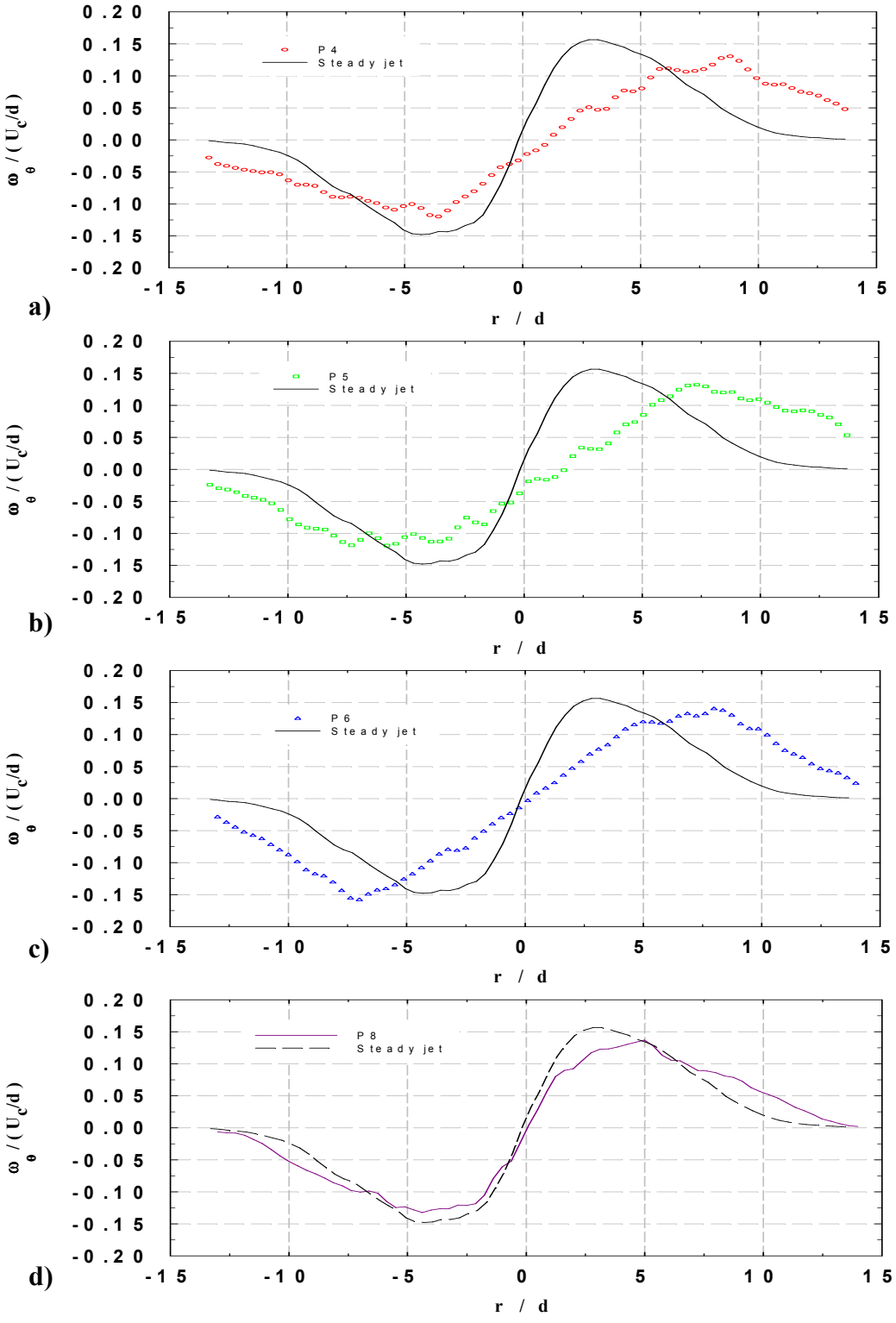

Figure 5.25: Normalized vorticity profiles at puff center for the puff and the steady jet a) *P*=4; b) *P*=5; c)*P*=6, and d) *P*=8. Dashed lines denote for the steady jet at the same axial location as the puff center.

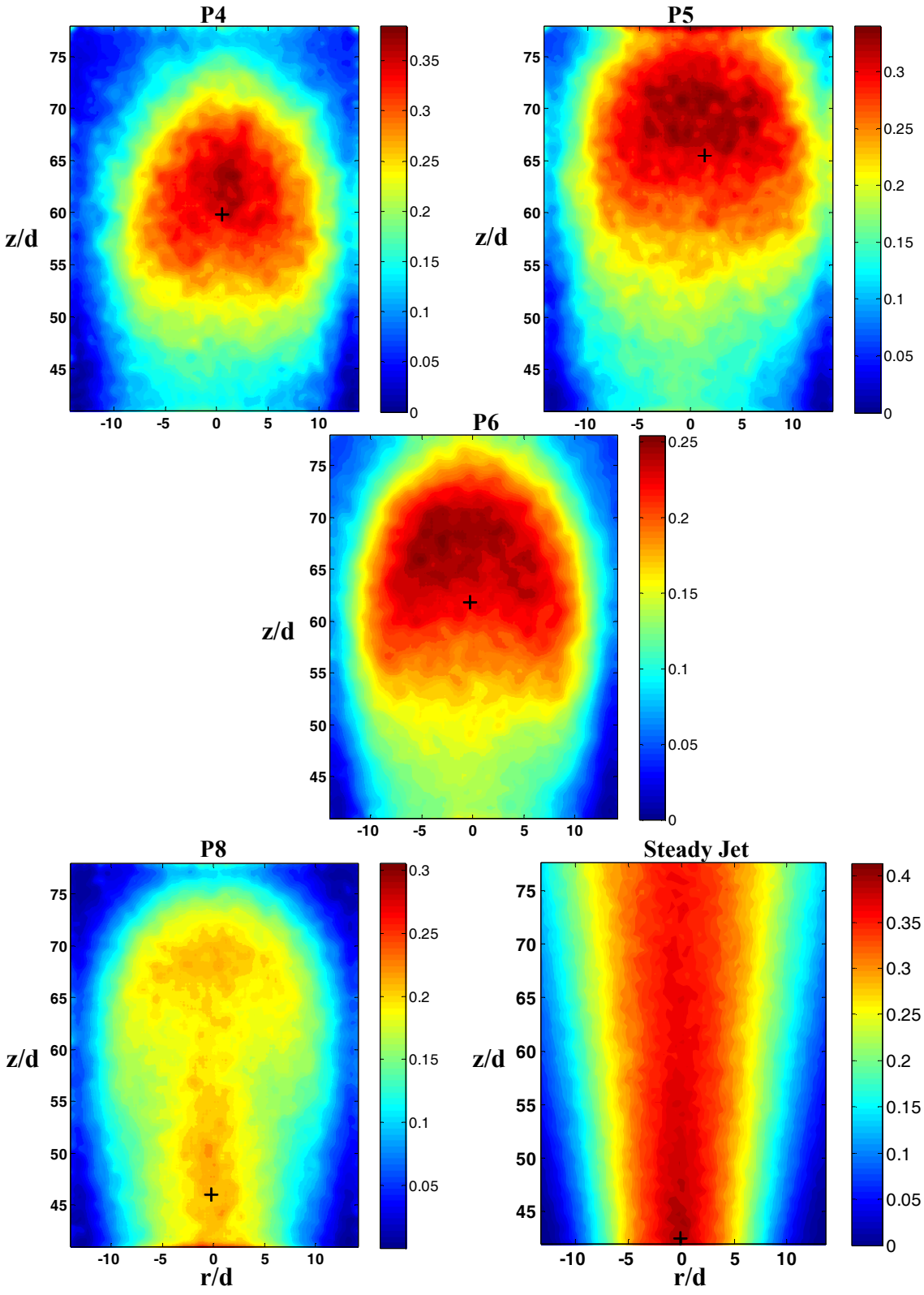

Figure 5.26: Normalized vorticity rms (ω'_{rms} d/U_c) contour for the puff, and the steady jet. The flow direction is from the bottom to the top. The bold plus denote the location of puff center.

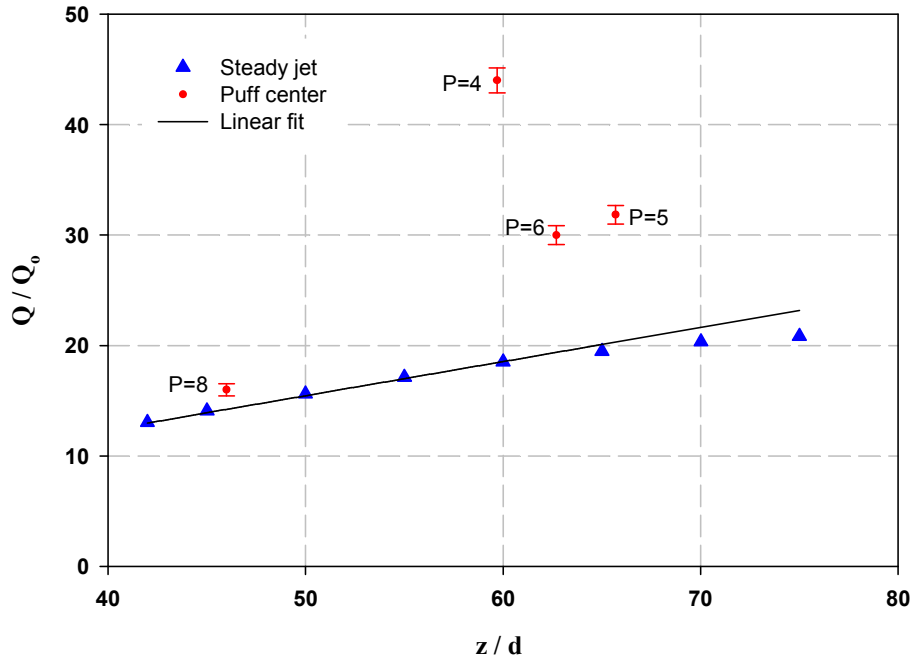

Figure 5.27: Normalized volume flow rate profiles for puff with P = 4,5,6, 8 and the steady jet. Puff values are located at puff center.

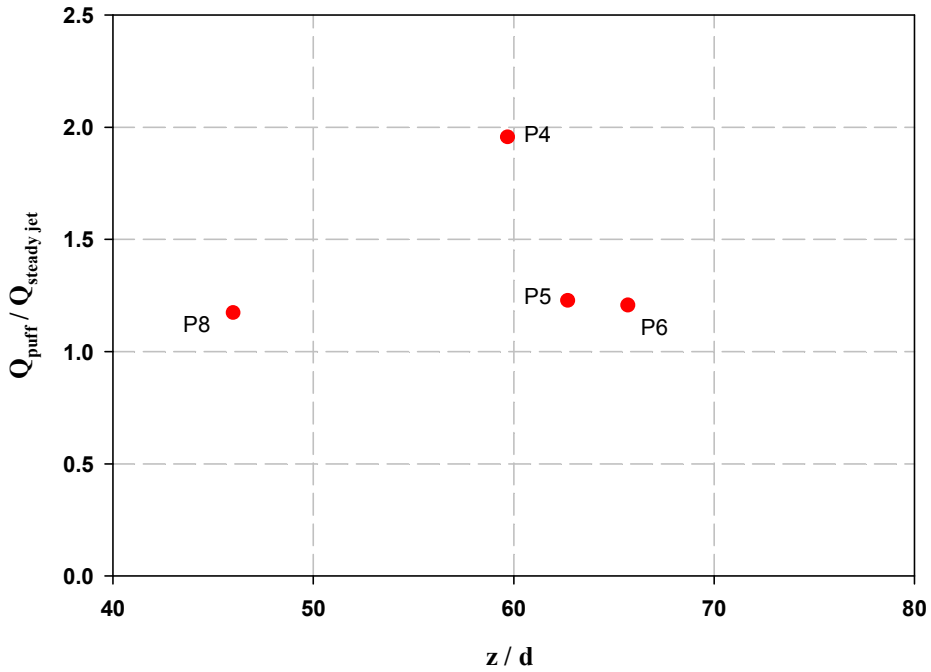

Figure 5.28: Ratio of the puff center volume flow rate to the steady jet volume flow rate. The steady jet volume flow is at the same axial location as the puff center for each puff.

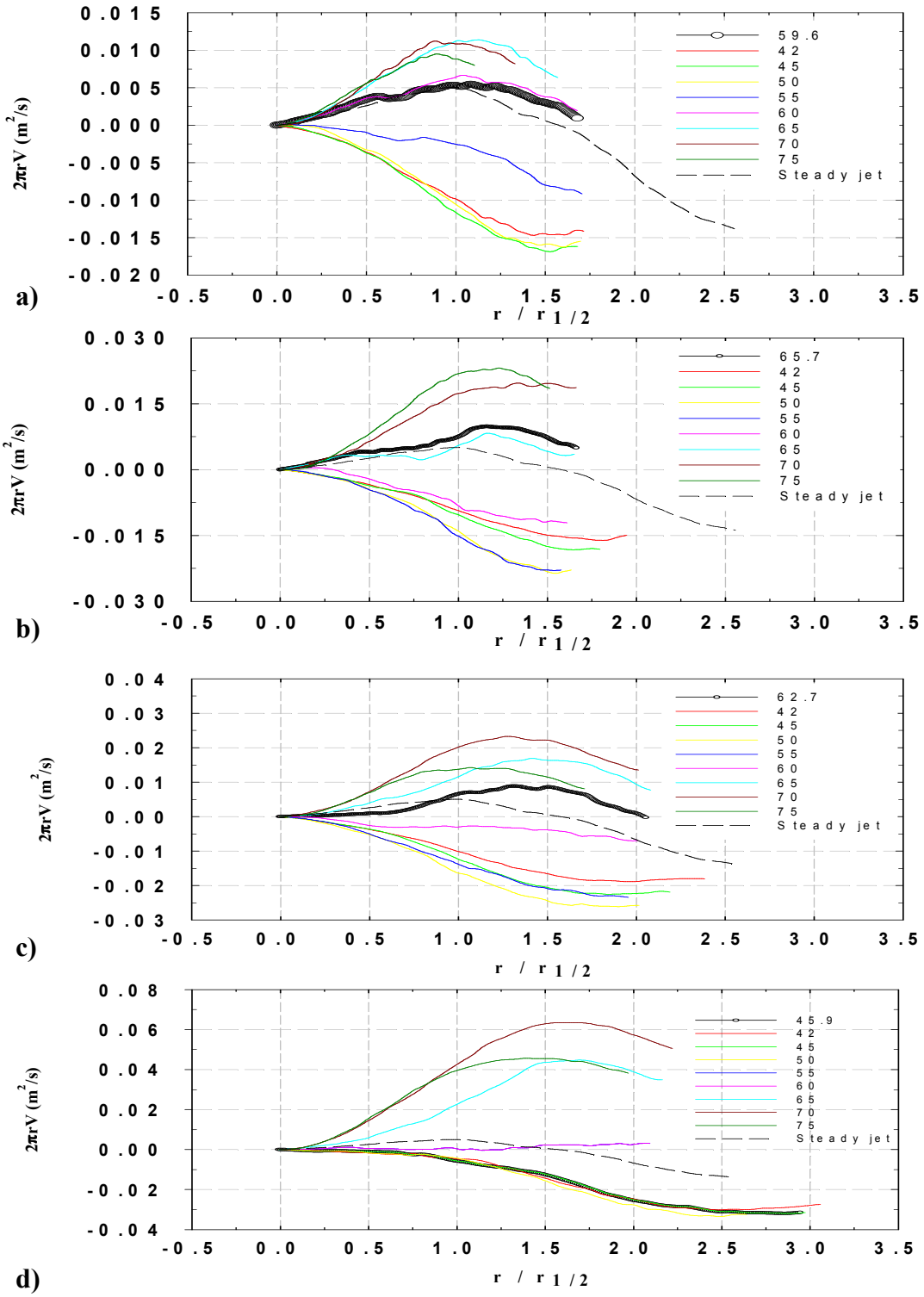

Figure 5.29: Profiles of $2\pi rV$ for the puff with a) P=4; b) P=5; c) P=6, and d) P=8. Circled lines denote data at the puff center, and dashed line denotes steady jet data at the same axial location of the puff center. The data are for the right half of the puff.

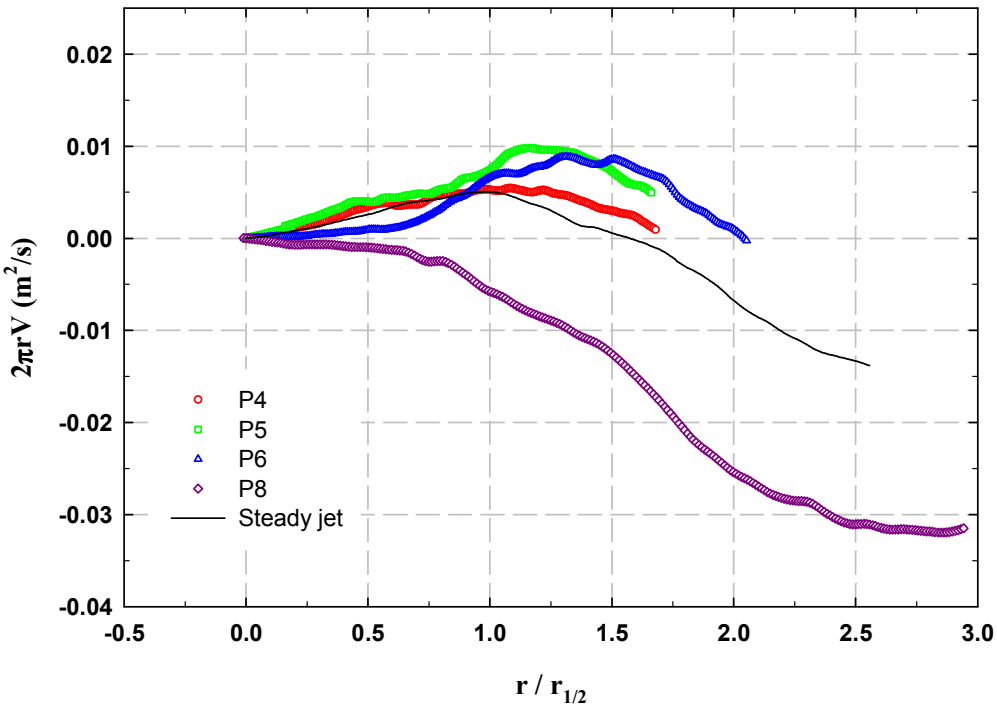

Figure 5.30: Profiles of $2\pi rV$ at puff center for the puffs and the steady jet. The unit is m^2/s. The data are for the right half of the flow field.

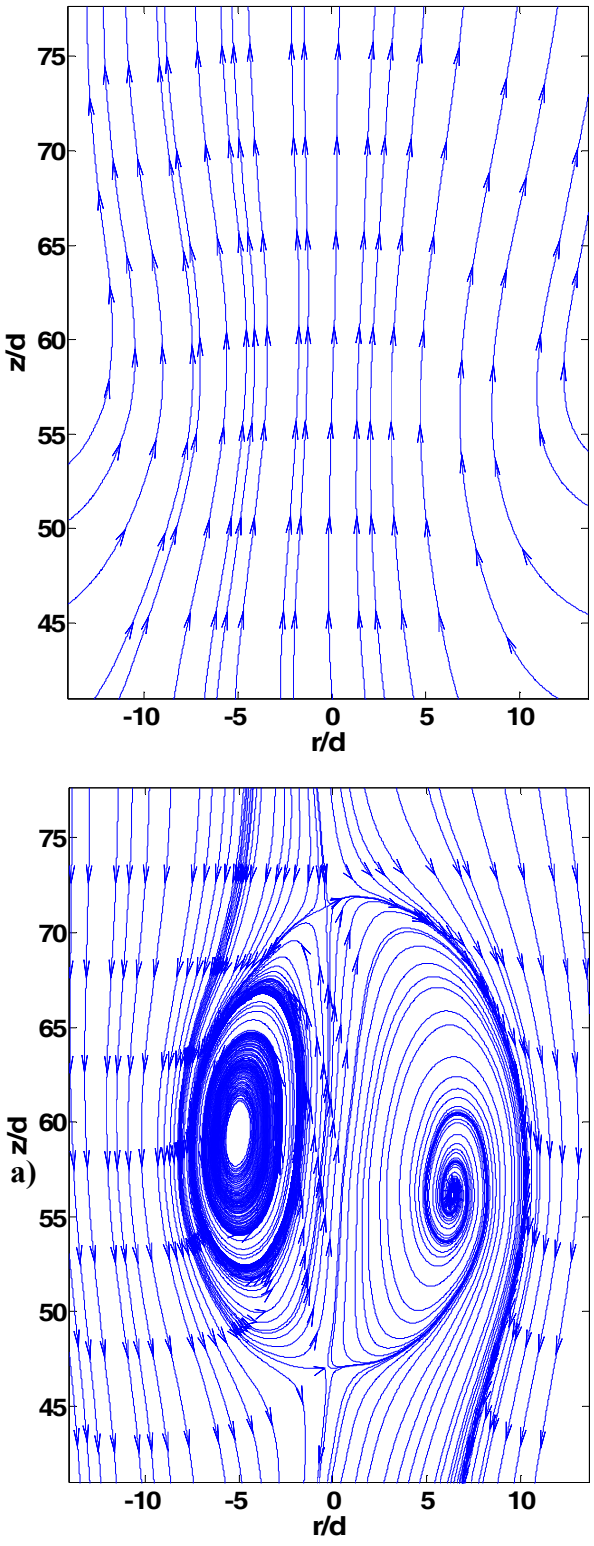

Figure 5.31: Instantaneous streamlines for puff with P=4: a) puff in a laboratory reference frame; b) puff in its moving frame.

6. Discussion and Conclusion

6.1 Discussion

In this section, the velocity field of puff with $P = 4$ is compared with the past work on the vortex ring and turbulent puff. A vortex ring is defined as an axially symmetric spheroidal volume of fluid whose internal mean vorticity lies entirely in the azimuthal direction (Glezer & Coles, 1990). The work of Richards (1965), Kovasznay *et al*., (1974), Sangras *et al.* (2002), Johnson (1971), Maxworthy (1972), Glezer & Coles (1990), Gahrib *et al.* (1998), and Dabiri & Gharib (2004) provide the most comprehensive analysis of the structure and entrainment of a vortex ring, and turbulent puffs. Kovasznay *et al*. (1974) suggested that a turbulent puff is a vortex ring growing by diffusion. In fact, the scaling laws listed below (and discussed earlier in the introduction) for the width, penetration and celerity of puffs are identical to those for turbulent vortex rings in the self-similar regime, except for the proportionality constants:

$$\delta \sim (z - z_o)$$

$$(z - z_o) \sim (\frac{I}{\rho})^{1/4}(t - t_o)$$

$$\frac{dz}{dt} \sim (\frac{I}{\rho})^{1/4}(t - t_o)^{-3/4} \sim \frac{I}{\rho}(z - z_o)^{-3}$$

The experiment conducted for the $P = 4$ puff in the present work is compared with the finding of Glezer & Coles (1990) in this section. In their study, a cylindrical volume of fluid moved at a constant velocity U_o for a time T_o through a circular orifice of diameter d. Their experiment was conducted in water with injection velocity of U_o =1.24 m/s, nozzle diameter of d = 1.9 cm, stroke ratio of H/d = 3.42, and Reynolds number of

Re_{jet} =24,000. Their velocity measurements were made for an ensemble average of 100 vortices at each LDV (Laser Doppler Velocimetry) probe position. Their similarity coordinates were defined as follow:

$$\xi = (z - z_o)(\frac{\rho}{I(t - t_o)})^{\frac{1}{4}}, \qquad \eta = r(\frac{\rho}{I(t - t_o)})^{1/4} \tag{6.1}$$

where I is the initial impulse ($\frac{I}{\rho} = \frac{1}{4}\pi d^2 H U_o = 2374 \pm 15 \text{ cm}^4/\text{s}$).

Figure 6.1 shows the experimental results of Glezer & Coles (1990) for the velocity and the vorticity contour of the vortex ring in their similarity coordinates. Their data is mirror-imaged about the symmetry axis. Their axial velocity, U, contour shown in Fig. 6.1a indicates the peak velocity region occurs at the vortex cores, while for the puff in the current study it is located near the puff center (Fig. 5.8). The axial velocity geometry for both vortex ring and puff are elongated. In the Glezer & Coles (1990) study, there are negative axial velocities at one side of each vortex core, which indicates a reverse flow around them. No negative axial velocity has been seen in the current study.

The radial velocity of the vortex ring, V, from Glezer & Coles (1990) is shown in Fig. 6.1b. The radial velocity of the vortex ring at centerline is zero. The peak values of vortex ring radial velocity are located at the vortex cores. The vortex ring radial velocity trend seems symmetric. There is a change of sign at the centerline; above the vortex cores the radial velocities are positive and below the vortex cores they are negative. There is a change of sign for radial velocity of the puff with $P = 4$ as well (Fig. 5.9).

The experimental results of Glezer & Coles, (1990) for azimuthal vorticity of the vortex ring, ω_θ, are shown in Fig. 6.1c. The vorticity is strongly concentrated in the

cores, and centerline has zero vorticity. The $P = 4$ puff vorticity structure shown in Fig. 5.24 also consists of a ring vortex, in which the maximum and minimum values are located around the cores. The puff centerline vorticity is also zero. The vorticity geometry of puff is more elongated than that of the vortex ring.

Figure 6.2 shows the experimental results of Glezer & Coles, (1990) for the normal Reynolds stresses and the turbulent shear stress contours of the vortex ring in similarity coordinates. The axial normal Reynolds stress, $<u'u'>$, and radial normal stress, $<v'v'>$, shown in Fig. 6.2a, and Fig. 6.2b, respectively, are strongly concentrated around the cores. The centerline of the vortex ring region has the least normal stress. In contrast to the vortex ring, the axial fluctuation velocity (Fig. 5.14) and radial fluctuation velocity (Fig. 5.17) for the $P = 4$ puff have the peak value around the puff center.

The vortex ring turbulent shear stress, $< u'v' >$, shown in Fig 6.2c indicates zero value at the centerline, and a change in its sign. The turbulent shear stress for the puff with $P = 4$ is shown in Fig. 5.20. The puff center also has zero turbulent shear stress. For the vortex ring, there is a change of sign in each side of the centerline, while the puff on each side of the puff center has the same sign. The contour geometry of the vortex ring is different from the puff as well.

It can be concluded from the puff results, especially the puff with $P = 4$, that it doesn't reveal a structure similar to that seen in turbulent vortex ring.

Kovasznay *et al.* (1974) studied the turbulent puff both in theory and experiment. They defined the puff as a moving mass of turbulent fluid with a finite linear momentum and kinetic energy. Their experiment was conducted in air with injection velocity of U_o

=30 m/s, nozzle diameter of d =1 inch, stroke ratio of H/d = 11.8, and Reynolds number of Re_{jet} = 50,000. The P parameter for their experiment was 2.3.

For theory, Kovasznay *et al.* (1974) used the linearized Navier-Stokes equations with velocity component u_i as follow:

$$\frac{\partial u_i}{\partial t} - \upsilon_t(t)\frac{\partial^2 u_i}{\partial x_k \partial x_k} = 0 \tag{6.2}$$

and the continuity equation :

$$\frac{\partial u_i}{\partial x_i} = 0 \tag{6.3}$$

They assumed the turbulent viscosity, υ_t , was constant at each axial station. By introducing a new variable

$$T(t) = \int \frac{\upsilon_T(t)}{\upsilon} dt \tag{6.4}$$

They rearranged the Navier-Stokes equation (6.2) as below:

$$\frac{\partial u_i}{\partial T} - \upsilon\frac{\partial^2 u_i}{\partial x_k \partial x_k} = 0 \tag{6.5}$$

Kovasznay *et al.* (1974) suggested the following expression for turbulent kinematic viscosity :

$$\upsilon_T(t) = \kappa U_c(t)\sigma(t) \tag{6.6}$$

where κ is a non-dimensional universal constant of the order of 10^{-2}, and σ is a characteristic radius value. The above assumption lead to these results for centerline velocity:

$$U_c(t) = (P_1/\sigma)(\frac{32}{3} P_1 \kappa t)^{-3/4} \tag{6.7}$$

$$\sigma(t) = (\frac{32}{3} P_1 \kappa t)^{1/4} \tag{6.8}$$

where P_1 is the axial pressure. The distance z traveled by the puff is then obtained as:

$$z \approx t^{1/4} \tag{6.9}$$

Table 6.1 summarizes similar scaling parameters from previous work for the round non-buoyant puff and vortex ring for $z = 4cn^3 \frac{I}{\rho_a} t^{C_z}$, and $\delta = 2(1/n)z$.

Table 6.1: Scaling parameters of non-buoyant turbulent puff and vortex ring.

Source	Medium	Re_{jet}	1/n	C_z
Present (measured at puff center)	Gas	5,000	0.22	
Sangras *et al.* (2002)	Liquid	3,000-12,000	0.18	1/4
Richards (1965)	Liquid	---	0.25	1/4
Kovasznay *et al.* (1974)	Gas	50,000	0.29	1/4
Vortex Ring:				
Glezer & Coles (1990)	Liquid	24,000	0.25	

The Kovasznay *et al.* (1974) experimental results for velocity and puff dimension are shown in Fig. 6.3, and Fig. 6.4, respectively. The velocity contours shown in Fig. 6.3 revealed a noticeable tail for their puff structure in the near field in comparison to the current study for puff with $P = 4$.

Figure 6.4 shows the half-width, $\delta_{0.5}$, and half-length, $L_{0.5}$, corresponding to the Kovasznay *et al.* (1974) experiment. Their results showed a linear growth for the puff. The puff aspect ratio, $\delta_{0.5}/L_{0.5}$, is less than 1, which shows an elongated structure for their puff. The axial location of the puff center for the P = 4 puff from the passive scalar

experiment is shown in Fig. 4.2; it is at z/d = 38 from nozzle. Table 6. 2 shows the result of the puff geometry for both current study and Kovasznay *et al.* (1974) at z/d = 7.9. Their puff is more elongated than the puff with P = 4 in our experiment. It is to be noted that their Reynolds number is larger than that of the present study by a factor of 10, and they looked at the near field flow.

Table 6.2: Puff Geometry result.

Source	P	Re_{jet}	$\delta_{0.5}/d$	$\delta_{0.5}/L_{0.5}$
Present	4	5,000	12.16	1.12
Kovasznay *et al.* (1974)	2.3	50,000	1.3	0.5

Based on the previous work done by Hermanson *et al.* (2004), which was discussed earlier in the Introduction section, the puff flame length increases as P increase. The results are shown in Fig. 1.4. The current study showed that the volume flow rate of the puff at its center is larger than that of the steady jet at the same axial distance (Fig. 5.28). The flame length of isolated burning puffs from Hermanson *et al.*, (2004) study and the volume flow rate of the current study are summarized in Table 6.3.

Table 6.3: Non-reacting puff volume flow rate and burning puff length.

P	Q_{Puff}/Q_{Steady}	L/d
4	2.39	59
5	1.58	85
6	1.55	110
8	1.13	160

The flame length of the puff with P = 8 is 2.7 times the P = 4 puff. On the other hand; the volume flow rate of the puff with P = 4 is 2.1 times the P = 8 puff. This indicates that the reduction in flame length for smaller P is directly related to the increase of the

volume flow rate. It is noteworthy that the entrainment and mixing rate of the flow will be altered by changing the structure of the flow.

6.2 Conclusion

A pulsed flow injector system was used to examine the structure of passive scalar concentration and the velocity fields of a non-interacting turbulent puffs. We were particularly interested in the effects of injection time and injection volume on the puff structure, volume and mixing efficiency. The planar laser Mie scattering technique was utilized to perform an investigation of the concentration field structure. The velocity field of isolated turbulent puffs and the steady jet were examined using Particle Image Velocimetry technique. In order to verify the puff measurements, the steady jet velocity field was measured and compared with the past measurement results.

Examination of the passive scalar concentration field in non-reacting isolated, turbulent puffs revealed that for injection conditions corresponding to $P \leq 8$, puffs evolved from a spherical geometry at $P = 4$ to that with a tail as the injection parameter P increases. A considerable tail was present for the puff with $P = 8$. It is noteworthy that none of the puff images reveals a structure similar to that seen in turbulent vortex rings. Although the presence of a tail region is common among puffs and turbulent vortex rings, the vortex ring cores contain high concentrations when compared to the fluid moving with the core. For the puffs, no evidence of large concentrated regions within the seeded flow was observed.

The measured half- and full-width, at the location of maximum concentration within the puff, decreased as the injection parameter P increased. The half-width for a puff with

$P = 8$ was comparable to that of the steady jet at the same location. The mean radial profiles became more Gaussian-like as P increased. The puff axial length enlarged with increasing P for the range of parameters examined.

The puff volume within the imaged area increased with P; however, the ratio of entrained volume to injected volume decreased as P increased. The decreasing normalized entrained volume indicated that puffs with larger P were less efficient in entraining and mixing with the ambient fluid. This confirmed the increasing length of flame puffs at larger values of P.

The velocity field of non-reacting isolated, turbulent puffs was measured by the PIV methods in a two-dimensional plane. Based on the analysis of the data, the profile for both axial and radial velocities and turbulent statistics got closer to the steady jet as P increased. The axial velocities were Gaussian with the same width at puff center.

The averaged velocity contours showed puffs evolved from an oblong geometry to one with a "tail" as the injection time increased. This confirms the observations from the passive scalar concentration field. The largest velocities occurred within the central portion of the puff. The measured axial velocity corresponding to the location of puffs followed the Gaussian distribution. The puff center half-width decreased with increasing P, and got closer to the steady jet value.

The axial and radial velocity fluctuations corresponding to the location of puff center were almost symmetric about the centerline. The highest peak value of axial and radial velocity fluctuations among the puffs was observed for puff with the puff with $P = 4$. The increase in maximum magnitude of axial and radial velocity fluctuations for the $P = 4$ puff were about 1.87 and 2 times the steady jet value, respectively.

The measured Reynolds shear stress for puffs at puff center was observed to follow a trend similar to the steady jet's but was of much larger magnitude, especially for the lowest P puff. The absolute maximum magnitude of the normalized turbulent shear stress for the $P = 4$ puff was about 2.5 times the steady jet value. This implied a larger entrainment rate for the $P = 4$ puff than that of the steady jet.

The turbulent kinetic energy contour plots clearly indicated that the peak kinetic energy for the puffs were around the centerline. The puff with the $P = 4$ generated larger turbulent kinetic energy than that of the puffs with higher P values and the steady jet.

The azimuthal vorticity field was calculated from the velocity field. The existence of two vortices was observed. The normalized vorticity magnitude did not significantly change by varying the P parameter when compared to the turbulent fluctuation velocities. The peak root-mean-square value of vorticity occurred around the puff center, the exception being for the puff with $P = 8$, which occurred at the trailing edge.

The inward radial flow of entrained gas into the puff at its center showed a larger value than that for the steady jet, except for the $P = 8$ puff. The ratio of the puff volume flow rate to that of the steady jet at the puff center location resulted in the largest value for the $P = 4$ puff.

The majority of entrainment into the puff occurred from below the puff center while the puff cap pushed out into the surrounding fluid. No entrainment took place at the puff center.

Puff structure is not similar to the steady jet in the range of $4 \leq P \leq 8$. In general, the puff characteristics do not reveal an internal structure similar to that seen in turbulent vortex rings.

6.3 Recommendations for Future Research

Based on the results of the current research, the following recommendations can be made for future work:

First, future studies of velocity fields in reacting puffs (flame) would be helpful to assess the effects of heat release and associated dilation on the puff characteristics.

Velocity measurements of both non-reacting and reacting puffs with different range of co-flow would be insightful in understanding how the puff behavior changes with varying co-flow velocities. It also helps to disarm how the entrainment characteristics of the puff change with different amount of co-flow.

In addition, velocity measurement experiments with the same level of detail should be performed at higher Reynolds numbers. This way it can be seen whether the conclusions drawn in this research could be applicable to higher Reynolds numbers.

The range of duty cycle for the measurement of the puff velocity field should be increased in order to investigate the effects of the interaction among the neighboring puffs.

The experiment could be conducted in a larger flow chamber, which would allow for a extended flow field. This way the flow field would be examined over a larger radial distance, and the puff entrainment could be analyzed with the closed streamline method.

Velocity and passive scalar measurements of puffs with smaller P $(P<4)$ would be useful in improving the mixing efficiency.

Furthermore, velocity and passive scalar measurements of puffs in cross flow would be helpful to explore more thoughts in entrainment and mixing efficiency.

Finally, computational fluid dynamic (CFD) models should be used to verify results of the present experiments. This research provides a database of detailed flow field measurements which can be used to verify the result of the CFD models.

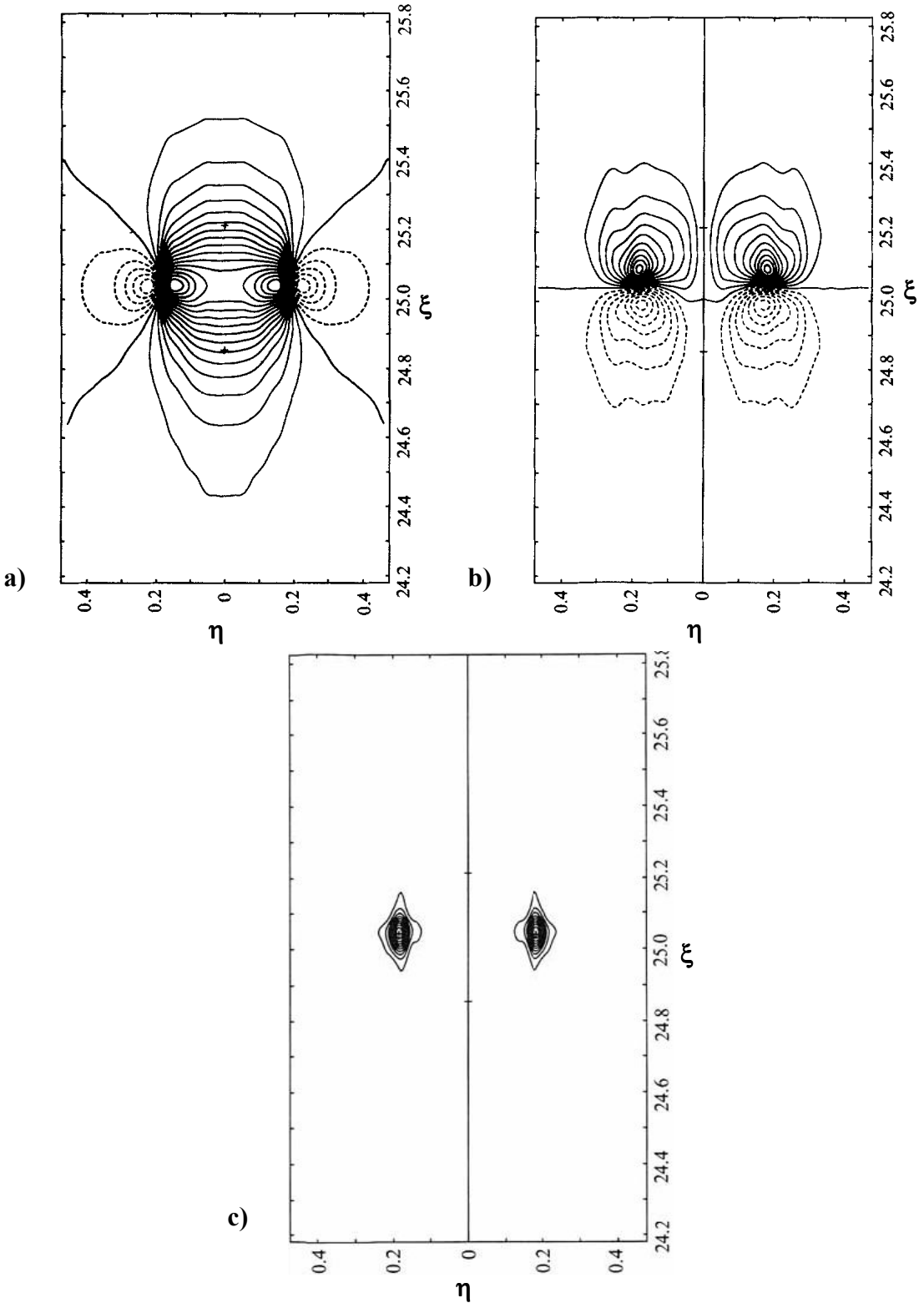

Figure 6.1: From Glezer & Cole (1990). Experimental measurement of a vortex ring in similarity coordinates for: a) axial velocity, contour labels are -5 (1) 16; b) radial velocity contour labels are -7 (1) 10; c) vorticity, contour labels are 100 (100) 1200.

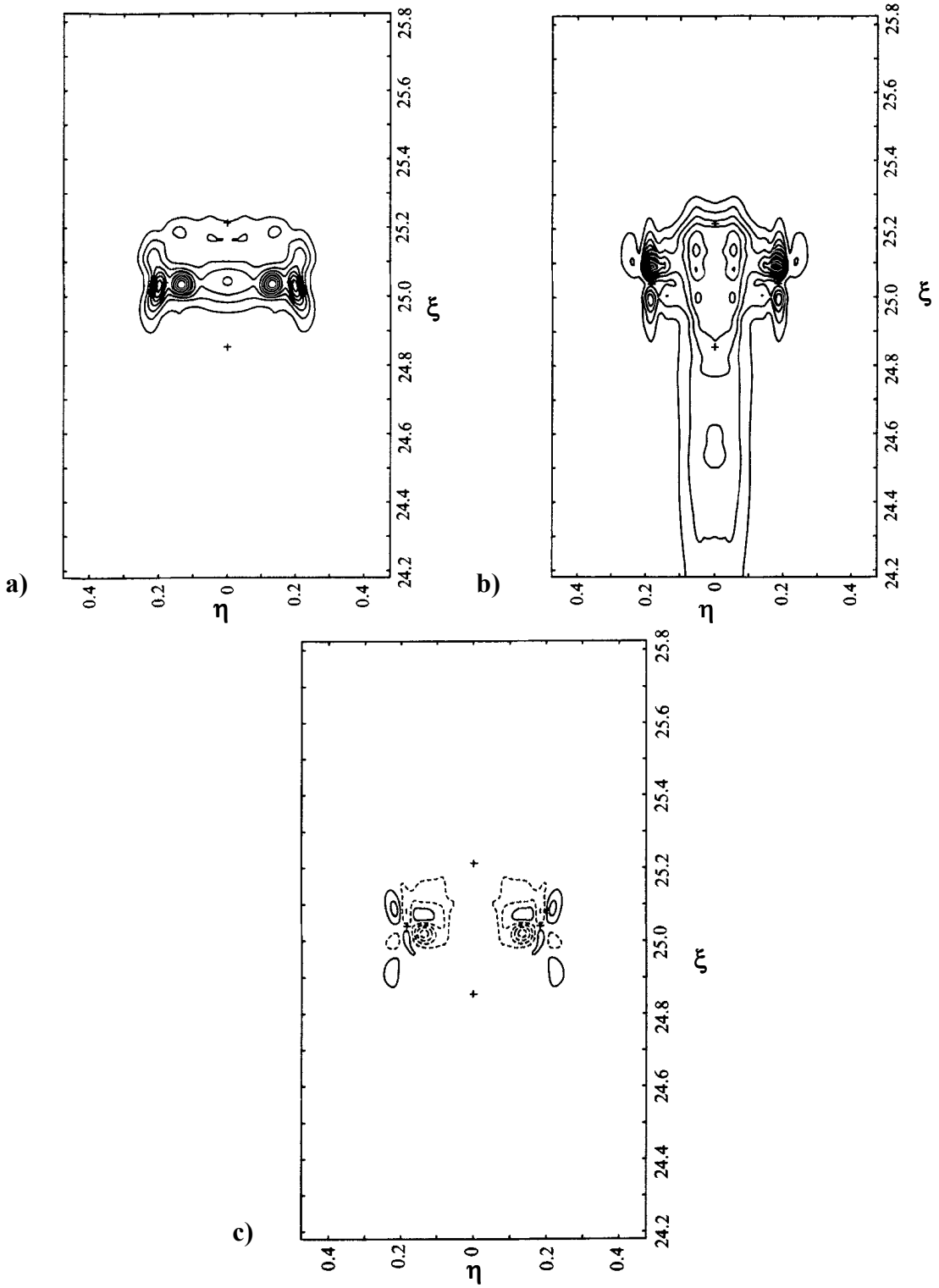

Figure 6.2: From Glezer & Cole (1990). Experimental measurement of a vortex ring in similarity coordinates for: a) axial normal Reynolds stress, contour labels are 0.25 (0.25) 2; b) radial normal Reynolds stress, contour labels are 0.5 (0.5) 4.5; c) Reynolds shear stress, contour labels are -0.7 (0.2) 0.3.

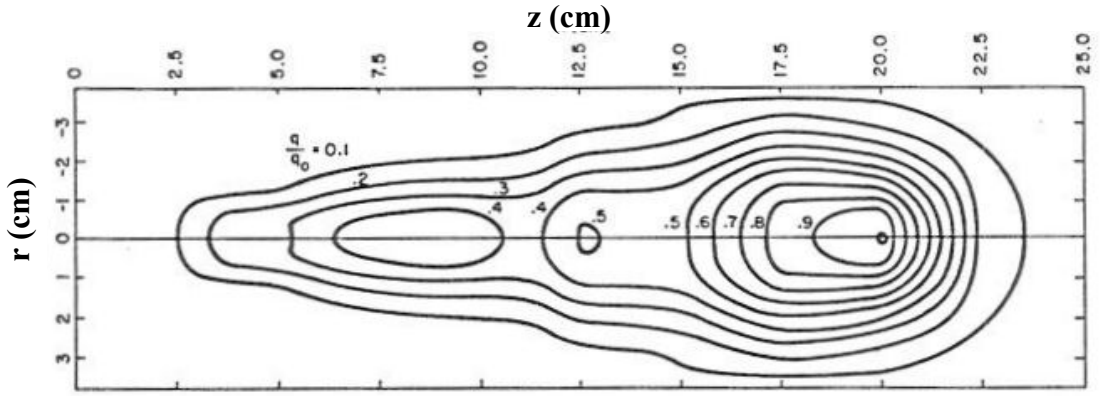

Figure 6.3: From Kovasznay *et al.,* (1974). Experimental measurement of absolute velocity for Puff with $P = 2.3$ and $Re_{jet} = 50{,}000$.

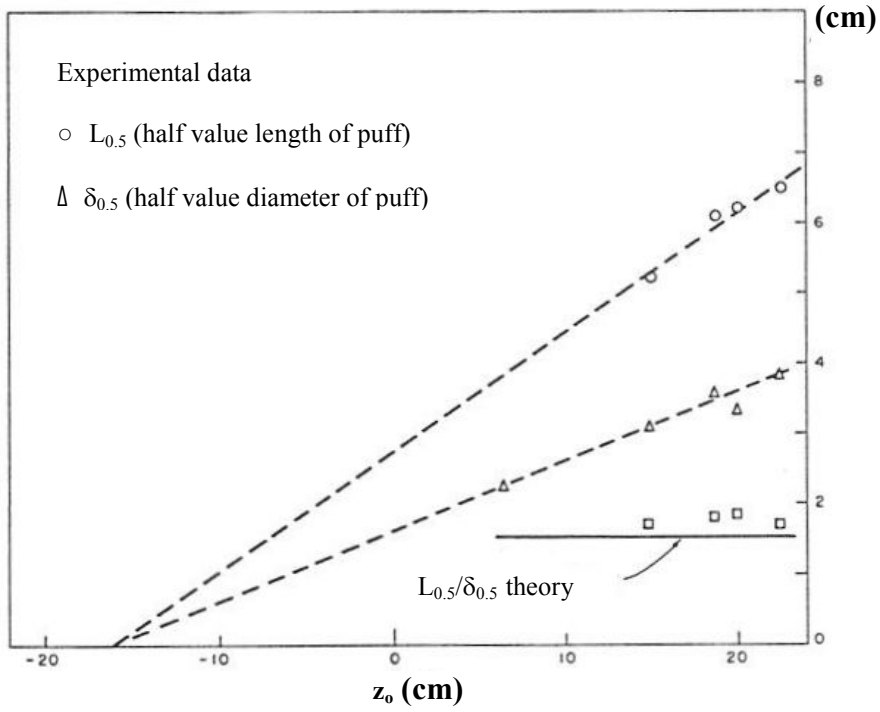

Figure 6.4: From Kovasznay *et al.,* (1974). Experimental measurement of puff dimension variation for Puff with $P = 2.3$ and $Re_{jet} = 50{,}000$.

7. References

Agrawal, A. and Parsad, A.K., "Integral Solution for the Mean Flow Profiles of Turbulent Jets, Plumes, and Wakes," *Journal of Fluid Engineering*, Vol. 125, No. 5, 2003, pp. 813-822.

Boersma, B.J., Brethouwer, G., and Nieuwstadt, F.T.M., "A Numerical Investigation on the Effect of the Inflow Conditions on the Self-Similar Region of a Round Jet," *Physics of Fluids*, Vol. 10-4, 1998, pp. 899-909.

Bremhorst, K. and Hollis, P.G, "Velocity Field of an Axisymmetric Pulsed, Subsonic Air Jet," *AIAA Journal*, Vol. 28, No. 12, 1990, pp. 2043-2049.

Broadwell, J.E., Dahm, W.J.A., and Mungal, M.G., "Blowout of Turbulent Diffusion Flames," *Twentieth Symposium (International) on Combustion*, the Combustion Institute, Pittsburgh, PA, 1984, pp. 303-310.

Brooks Instruments Produtcs Information Catalog, 2004.

Chen, C.J. and Rodi, W., Vertical Turbulent Buoyant Jets - A Review of Experimental Data, Pergamon Press Ltd., 1980.

Chen, T.Y., Hegde, U.G., Daniel, B.R., and Zinn, B.T., "Flame Radiation and Acoustic Intensity Measurements in Acoustically Excited Diffusion Flames," *Journal of Propulsion and Power*, Vol. 9, 1993, pp. 210-216.

Crow, S.C. and Champagne, F.H., "Orderly Structure in Jet Turbulence," *Journal of Fluid Mechanics*, Vol. 48, 1971, pp. 547-591.

Dabiri, J. O. and Gharib, M., "Fluid Entrainment by Isolated Vortex Ring," *Journal of Fluid Mechanics*, Vol. 511, 2004, pp. 311.

Dahm, W.J.A. and Dibble, R.W., "Coflowing Turbulent Jet Diffusion Flame Blowout," *22nd International Symposium on Combustion*, 1988, pp. 801-808.

Dahm, W.J.A. and Dimotakis, P.E., "Measurement of Entrainment and Mixing in Turbulent jets," *AIAA Journal*, Vol. 25, No. 9, 1987, pp. 1216-1223.

Dahm, W.J.A. and Dimotakis, P.E., "Mixing at Large Schmidt Number in the Self-Similar Far Field of Turbulent Jets," *Journal of Fluid Mechanics*, Vol. 217, 1990, pp. 299-330.

Diez, F.J., Sangras, R., Kwon, O.C., and Faeth, G.M., "Erratum: Self-Preserving Properties of Unsteady Round Nonbuoyant Turbulent Starting Jets and Puffs in Still Fluids," *ASME Journal of Heat Transfer*, Vol. 125, 2003, pp. 204-205.

Dimotakis, P.E., Miake-Lye, R.C., and Papantonious, D.A., "Structure and Dynamics of Round Turbulent Jets," *Physics of Fluids*, Vol. 26, No. 11, Nov. 1983a, pp. 3185-3192.

Dowling, D.R., Lang, D.B., and Dimotakis, P.E.," An Improved Laser-Rayleigh Scattering Photodetection System., "*Experiments in Fluids*, Vol. 7, 1989, pp. 435-440.

Driscoll, J.F., Chen, R-H., and Yoon, Y., "Nitric Oxide Levels of Turbulent Jet Diffusion Flames: Effects of Residence Time and Damkohler Number," *Combustion and Flame*, Vol. 88, 1992, pp. 37-48.

Falcone, A.M. and Cataldo, J.C., "Entrainment Velocity in an Axisymmetric Turbulent Jet, "*Journal of Fluids Engineering*, Vol. 125, No. 4, 2003, pp. 620.

Fischer, H.B., List, J.E., Koh, C.R., Imberger, J., and Brooks, N.H., "Mixing in Inland and Coastal Waters," Academic Press (New York), 1979, pp. 302.

Gharib, M., Rambod, E., and Shariff, K., "A Universal Time for Vortex Ring Formation," *Journal of Fluid Mechanics*, Vol. 360, 1998, pp. 121.

Glezer, A. and Coles, D., "An Experiment Study of a Turbulent Vortex Ring," *Journal of Fluid Mechanics*, Vol. 211, 1990, pp. 243-283.

Han, D. and Mungal, M.G.," Direct Measurement of Entrainment in Reacting/Nonreacting Turbulent Jets," *Combustion and Flame*, Vol.124, No.3, 2001, pp. 370.

Haynes, B.S. and Wagner, H.G., "Soot Formation," *Progress in Energy and Combustion Science*, Vol. 7, 1981, pp. 229-273.

Hermanson, J.C., Dugnani, R., and Johari, H., "Structure and Flame Length of Fully-Modulated, Pulsed Diffusion Flames," *Combustion Science and Technology*, Vol. 155, 2000, pp. 203-225.

Hermanson, J.C., Ghaem-Maghami, E., and Johari, H., "CO/UHC Emissions of Fully-Modulated Diffusion Flames," *Combustion Science and Technology*, Vol. 176, 2004, pp. 1855-1866.

Hermanson, J.C., Usowicz, J.E., Johari, H., and Sangras, R., "The Effects of Co-Flow on Isolated Turbulent Flame Puffs," *AIAA Journal*, Vol. 40, No. 7, 2002, pp. 1355-1362.

Hill, B., "Measurement of Local Entrainment Rate in the Initial Region of Axisymmetric Turbulent Air Jets,"*Journal of Fluid Mechanics*, Vol. 51, 1972, pp. 773-779.

Hulst, H.C. Van de, Light Scattering by Small Particles, New York wiley, Dover, 1957.

Hussein H.J., Capp, S.P., and George, W.k., "Velocity-Measurements in a High-Reynolds-Number, Momentum-Conserving, Axisymmetrical, Turbulent Jet," *Journal of Fluid Mechanics*, Vol. 258, 1994, pp. 31-75.

Johari, H. and Motevalli, V., "Flame Length Measurements of Burning Fuel Puffs," *Combustion Science and Technology*, Vol. 94 (1-6), 1993, pp. 229-245.

Johnson, G. M., "An empirical model of the motion of turbulent vortex rings," *AIAA Journal*, Vol. 9, No. 4, 1971, pp. 763-764.

Jones, H.R.N. and Leng, J., "The Effect of Hydrogen and Propane Addition on the Operation of a Natural Gas-Fired Pulsed Combustor," *Combustion and Flame*, Vol. 99, 1994, pp. 404-412.

Karasso, P.S., Expeiments on Mixing and Reaction in Plane and Curved Shear Layers, *HTGL report No. T-300*, Stanford University, July 1994.

Keller, J.O. and Hongo, I., "Pulse Combustion: The Mechanisms of NO_x Production," *Combustion and Flame*, Vol. 80, 1990, pp. 219-237.

Kovasznay, L.S.G., Fujita, H., and Lee, R.L., "Unsteady Turbulent Puffs," *Advanced in Geophysics*, 1974, pp. 253-263.

Lefebvre, A., "Pollution Control in Continuous Combustion Engines," *15th Symposium (International) on Combustion*, 1975, pp. 1169-1180.

Liepmann, D. and Gharib, M., "The role of streamwise vorticity in the near-field entrainment of round jets," *Journal of Fluid Mechanics*, Vol. 245, 1992, pp. 643-668.

Lovett, J.A. and Turns, S.R., "Experiments on Axisymmetrically Pulsed Turbulent Jet," *AIAA Journal*, Vol. 28, 1990, pp. 38-46.

Maxworthy, T., "The Structure and Stability of Vortex Rings," *Journal of Fluid Mechanics*, Vol. 51, 1972, pp. 15.

McCabe, W.L., Unit Operations of Chemical Engineering, McGraw-Hill, New York, 1976.

Mungal, M.G., Karasso, P.S., and Lozano, A., "The Visible Structure of Turbulent Jet Diffusion Flames: Large-Scale Organization and Flame Tip Oscillation," *Combustion Science and Technology* , Vol. 76, 1991, pp. 165-185.

Mungal, M.G. and O'Neil, J.M., "Visual Observations of a Turbulent Diffusion Flame," *Combustion and Flame*, Vol. 78, 1989, pp. 377-389.

Oshima, K., Kovasznay, L.S.G., and Oshima, Y., "Sound Emission from Burning Puff," *Lecture Notes in Physics*, Vol. 76, 1977, pp. 219-230.

Panchapakesan, N.R. and Lumley, J. L., "Turbulence Measurements in Axisymmetric Jets of Air and Helium. Part 1. Air Jet," *Journal of Fluid Mechanics*, Vol. 246, 1993, pp. 225-247.

Parr, T.P., Gutmark, E., Wilson, K., Hanson-Parr, D.M., Yu, K., Smith, R.A., and Schadow, K.C., "Compact Incinerator Afterburner Concept Based on Vortex Combustion," *Twenty-sixth Symposium (International) on Combustion*, The Combustion Institute, 1996, pp. 2471-2477.

Peters, N. and Donnerhack, S., "Structure and Similarity of Nitric Oxide Production in Turbulent Diffusion Flames," *15th Symposium (International) on Combustion*, 1981, pp. 33-42.

Platzer, M.F., Simmons, J.M., and Bremhorst, K.," Entrainment Characteristics of Unsteady Subsonic Jets," *AIAA Journal*, Vol. 16, 1978, pp. 282-284.

Raffel, M., Willert, C.E., and Kompenhans, J., Particle Image Velcoimetry- A Practical Guide, Springer, 1998.

Reuter, D.M., Daniel, B.R., Jagoda, J.I., and Zinn., B.T., "Periodic Mixing and Combustion Processes in Gas Fired Pulsating Combustors," *Combustion and Flame*, Vol. 65, 1986, pp. 281-290.

Reuter, D.M., Hedge, U.G., and Zinn, B.T., "Flow Field Measurements in an Unstable Ramjet Burner," *Journal of Propulsion and Power,* Vol. 6, 1990, pp. 680-865.

Richards, J.M., "Puff Motions in Unstratified Surroundings," *Journal of Fluid Mechanics*, Vol. 21, 1965, pp. 97-106.

Ricou, F.P. and Spalding, D.B., "Measurement of Entrainmet by Axisymmetrical Turbulent Jets,"*Journal of Fluid Mechanics*, Vol. 11, 1961, pp. 21-32.

Sangras, R. and Faeth, G.M., "Round Turbulent Nonbuoyant Starting Jets and Puffs and Buoyant Starting Plumes and Thermals," *Proceedings of the 34th National Heat Transfer Conference*, 2000, pp. NHTC 2000-12174.

Sangras, R., Kwon, O.C., and Faeth, G.M., "Self-Preserving Properties of Unsteady Round Nonbuoyant Turbulent Starting Jets and Puffs in Still Fluids," *ASME Journal of. Heat Transfer*, Vol. 124, 2002, pp. 460-469.

Sarohia, V. and Bernal, L.P., "Entrainment and Mixing in Pulsatile Jets," *Third Symposium on Turbulent Shear Flows*, 1981, pp. 11.30-11.35.

Scarano, F. and Riethmuller, M.L., "Iterative Multigrid Approach in PIV Image Processing with Discrete Window Offset," *Experiments in Fluid*, Vol. 26, 1999, pp. 513-523.

Scorer, R.S., "Experiments on Convection of Isolated Masses of Buoyant Fluid," *Journal of Fluid Mechanics*, Vol. 2, 1957, pp. 583-594.

Stanislas, M., Okamoto, K., Kahler, C.J., "Main Results of the Second International PIV Chalenge," *Experiments in Fluid*, Vol. 39, 2005, pp. 170-191.

Tang, Y.M., Ku, S.H., Daniel, B.R., Jagoda, J.I., and Zinn, B.T., "Controlling the Rich Limit of Operation of Pulse Combustors," *23rd Symposium (International) on Combustion*, 1995, pp. 1005-1010.

Tang, Y.M., Waldherr, G., Jagoda, J.I., and Zinn, B.T., "Heat Release Timing in a Nonpremixed Helmholtz Pulse Combustor," *Combustion and Flame*, Vol. 100, 1995, pp. 251-261.

Taylor, J. R., An Introduction to Error Analysis, 2nd Ed., University Science books, 1997.

Tennekes, H. and Lumley, J.E., A First Course in Turbulence, 1972, MIT press.

Tso, J., Kovasznay, L.S.G., and Hussain, A.K.M.F.," Search for Large Scale Coherent Structure in the Nearly Self Preserving Region of a Turbulent Axisymmetric Jet," *Journal of Fluid Mechanics*, Vol. 103, 1981, pp. 503-508.

Turner, J.S., "Turbulent Entrainment: The Development of the Entrainmet Assumption, and Its Application to Geophysical Flows," *Journal of Fluid Engineering,* Vol. 173, 1986, pp. 431-471.

Turns, S.R. and Bandaru, R.V., "Carbon Monoxide Emissions from Turbulent Nonpremixed Jet Flames," *Combustion and Flame,* Vol. 94, 1993, pp. 462-468.

Turns, S.R., "Understanding Nox Formation in Nonpremixed Flames: Experiments and Modeling," *Progress in Energy and Combustion Science*, Vol. 21, 1995, pp. 361-385.

Usowicz, J.C., "An Experimental Study of Flame Lengths and Emissions of Fully-Modulated Diffusion Flame," MS. Thesis, 2001, WPI.

Vermeulen, P.J., Ramesh, V., and Yu, W.K., "Measurement of Entrainment by Acoustically Pulsed Axisymmetric Air Jets," *Journal of Engineering Gas Turbines and Power,* Vol. 108, 1986, pp. 479-484.

Webster, D.R., Roberts, P.J.W., and Ra'ad, L., "Simultaneous DPTV/PLIF Measurements of a Turbulent Jet," *Experiments in Fluids*, Vol. 30, No. 1, Jan. 2001, pp. 65-72.

Willert, C.E. and Gharib, M., "Digital Particle Image Velocimetry," *Experiment in Fluids,* Vol. 10, 1991, pp. 181-193.

Wygnanski, I.J. and Fiedler, H.E., "Some Measurements in the Self-Preserving Jet," *Journal of Fluid Mechanics*, Vol. 38, 1969, pp. 577-612.

Zenz, F.A., Fluidization and Fluid-Particle System, Reinhold publishing corporation, New York, 1960.

Appendix A: Co-flow rates

Table A.1: Actual flow rate for Re = 5,000.

Rotameter Reading (SCFM)	Pressure Reading (psi)	SF	Corrected Rotameter Reading (SCFM)	Co-Flow Velocity (m/s)	Ucof / U_o %
0	0.00	1.00	0.00	0.00	0.00
2	0.12	1.00	2.01	0.01	0.07
4	0.28	1.01	4.04	0.02	0.13
6	0.47	1.02	6.10	0.03	0.20
8	0.70	1.02	8.19	0.04	0.27
10	0.96	1.03	10.32	0.05	0.34
12	1.25	1.04	12.50	0.07	0.41
14	1.58	1.05	14.73	0.08	0.49
16	1.94	1.06	17.02	0.09	0.56
18	2.34	1.08	19.38	0.10	0.64
20	2.77	1.09	21.80	0.11	0.72
22	3.24	1.10	24.30	0.13	0.80
24	3.74	1.12	26.88	0.14	0.89
26	4.27	1.14	29.54	0.15	0.98
28	4.84	1.15	32.29	0.17	1.07
30	5.45	1.17	35.12	0.18	1.16
32	6.09	1.19	38.05	0.20	1.26
34	6.76	1.21	41.08	0.22	1.36
36	7.47	1.23	44.21	0.23	1.46
38	8.21	1.25	47.44	0.25	1.57
40	8.98	1.27	50.77	0.27	1.68

Appendix B: Image Processing Routines

The volume of puff was extracted in an automated fashion from the image of the puff recorded in the experiments. The image processing routine is shown graphically in Figure A.1. The image process was done using the graphical programming language WiT. The routine is shown in Fig. B.1 is the actual program used to process the data in this research for calculating puff volume.

The processing procedure consisted of thresholding the image into a binary format, then performing blob detection on the binary image to select the largest blob which represented the image of the puff. The extents of the blob were then extracted as measures of the puff diameter and height. The volume was estimated assuming each column of pixels from the centerline outward in the puff blob was revolved around the centerline to form a ring. Then the volume of all these rings was summed to estimate the total volume of the puff. Since this calculation used only half of the puff in the volume estimate (columns from the centerline of the puff out), the volume was estimated twice from each side of the puff centerline. Then the average of these two volume estimates was calculated to give a final best estimate for the volume enclosed by the puff.

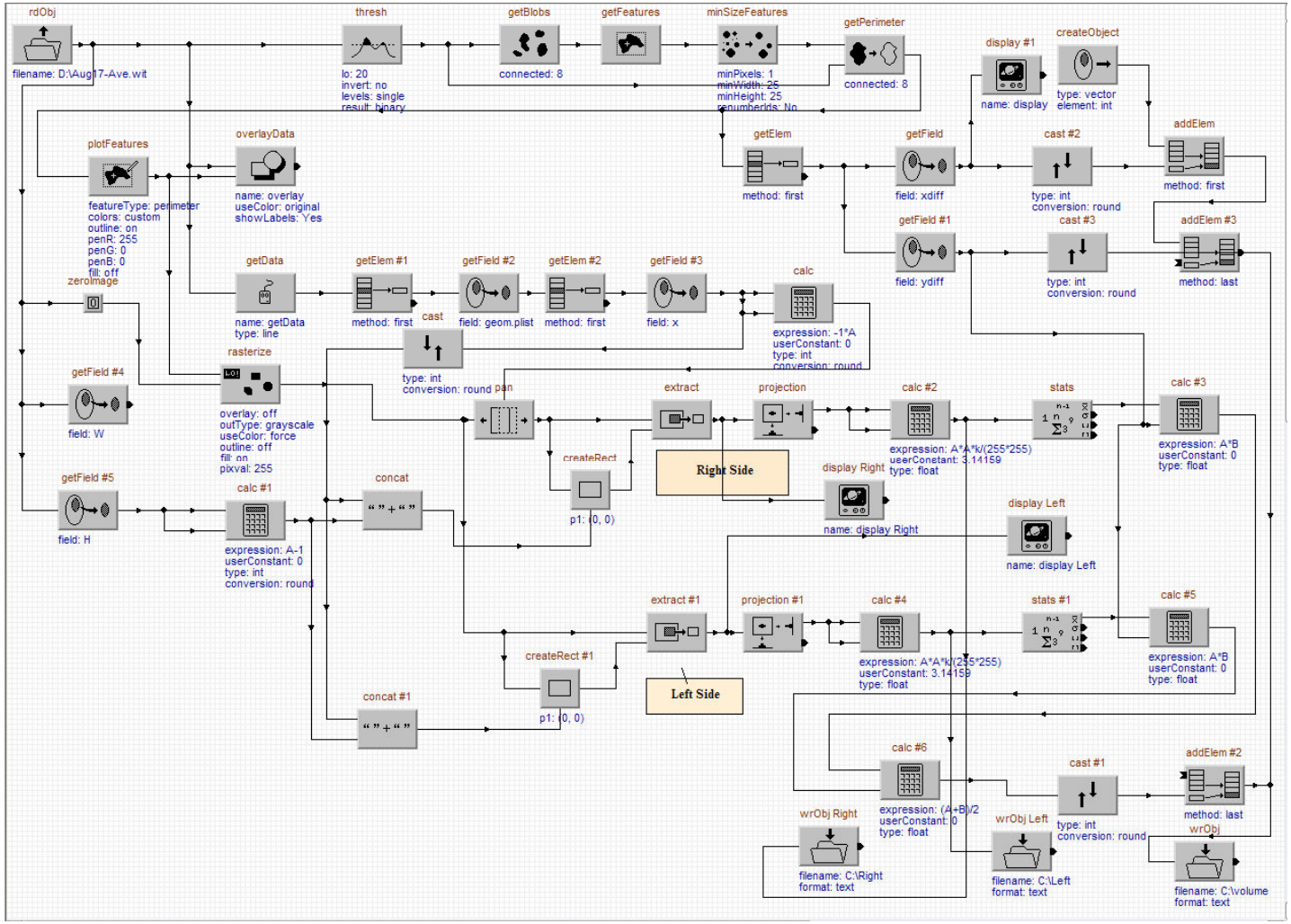

Figure B.1: The image processing routine used to calculate the puff volume.